Modélisation de la compaction d'assemblages granulaires mous : effet du mélange de grains mous/rigides et de la forme des particules

Manuel Cardenas-Barrantes

THÈSE POUR OBTENIR LE GRADE DE DOCTEUR DE L'UNIVERSITÉ DE MONTPELLIER

En Physique

École doctorale : Information, Structures, Systèmes
Unité de recherche LMGC

Modélisation de la compaction d'assemblages granulaires mous : effet du mélange de grains mous/rigides et de la forme des particules.

Modeling the compaction of soft granular packings: effect of mixed soft/rigid grains and particle shape.

Présentée par Manuel CÁRDENAS - BARRANTES

Sous la direction de Emilien AZÉMA et Mathieu RENOUF

Devant le jury composé de

M. Luca CIPELLETTI, Professeur, Université de Montpellier - IUF	Président du jury
Mme. Karen DANIELS, Full Professor, North Carolina State University	Rapporteure
M. Patrick RICHARD, Directeur de recherche, Université de Gustave Eiffel	Rapporteur
Mme. Vanessa MAGNANIMO, Associate Professor, Twente University	Examinatrice
M. Emilien AZÉMA, Maître de conférences, Université de Montpellier - IUF	Directeur de thèse
M. Mathieu RENOUF, Chargé de recherche, CNRS - Université de Montpellier	Co - directeur
M. Jonathan BARÉS, Ingénieur de recherche, CNRS - Université de Montpellier	Invité

UNIVERSITÉ DE MONTPELLIER

Title in English

Modeling the compaction of soft granular packings: effect of mixed soft/rigid grains and particle shape.

Titre en France

Modélisation de la compaction d'assemblages granulaires mous : effet du mélange de grains mous/rigides et de la forme des particules.

Abstract: The compaction behavior of deformable grain assemblies beyond jamming remains misunderstood, and existing models that seek to find the relationship between the confining pressure P and solid fraction ϕ end up settling for empirical strategies or fitting parameters. Numerically and experimentally, we analyze the compaction of highly deformable frictional grains of different shapes and soft/rigid particle mixtures in two and three dimensions: numerically, using a coupled discrete - finite element method, the Non-Smooth Contact Dynamics Method (NSCD), and experimentally using high-resolution imaging coupled with a dedicated DIC algorithm. We characterize the evolution of the packing fraction, the elastic modulus, and the microstructure (particle rearrangement, connectivity, contact force, and particle stress distributions) as a function of the applied stresses. We show that the solid fraction evolves non-linearly from the jamming point and asymptotically tends to a maximal packing fraction, depending on the soft/rigid mixture ratio, the friction coefficient, and the particle shape. At the microscopic scale, different power-law relations are evidenced between the local grain structure and contacts, and the packing fraction and pressure, regardless of the shape, the mixture ratio, or the dimensionality (2D/3D). A significant outcome of this work is the development of a theoretical and micromechanical-based approach for the compaction of soft granular assemblies far beyond the jamming point. This latter is derived from the granular stress tensor, its limit to small deformations, and the evolution of the connectivity. Furthermore, from the expression of these well-defined quantities, we establish different compaction equations, free of *ad hoc* parameters, well-fitting our numerical and experimental data. These equations mainly depend on the dimensionality, where the characteristics of shape, elastic bi-dispersity, and compression geometry (uniaxial *vs* isotropic) are considered as input parameters. Our theoretical framework allows us to unify the compaction behavior of assemblies of soft, soft/rigid, and noncircular soft particles coherently, both in 2D and 3D, for isotropic and uniaxial compression.

Resumé: La compaction d'assemblages de grains mous au-delà de leur point de blocage (i.e., le "jamming point"), bien que très étudiée reste encore mal comprise. Par exemple, un très grand nombre d'équations reliant l'évolution de la pression de confinement P à la compacité ϕ ont été proposés mais la plupart des équations existantes s'appuient sur des stratégies empiriques impliquant souvent plusieurs paramètres d'ajustement dont le sens physique n'est pas toujours clair. Dans ce travail de thèse, au moyen de simulations numériques et d'expériences modèles, nous analysons la compaction de grains frottant hautement déformables, de différentes formes, ou encore des mélanges de grains déformable/rigide en deux et trois dimensions. Numériquement, nous utilisons la méthode de dynamique des contacts non régulière ("Non-Smooth Contact Dynamics NSCD") couplant la méthode de Dynamique des Contacts (pour gérer le contact entre grains) à la méthode des Eléments Finis (pour la déformation des grains), et expérimentalement nous

utilisons des techniques d'imagerie à haute résolution couplées à des algorithmes de DIC sur un système quasi-2D de compression unixial. Dans tous nos essais, nous caractérisons l'évolution de la compacité, du module élastique et de la microstructure (réarrangement des particules, connectivité, forces de contact et distributions des contraintes dans les particules) en fonction des contraintes appliquées. Nous montrons que la compacité évolue de manière non linéaire à partir du point de blocage et tend asymptotiquement vers une compacité maximale qui dépend du rapport de mélange de grains déformable/rigide, du coefficient de frottement ou encore de la forme des particules. À l'échelle microscopique, différentes relations en lois de puissances sont mises en évidence entre, d'un coté, les structures locales à l'échelle des grains et des contacts et, de l'autre coté, la compacité et la pression, indépendamment de la forme, du rapport de mélange ou de la dimension du problème (2D/3D). Finalement, un résultat majeur de ce travail est la mise en place d'un cadre théorique et micromécanique pour l'étude de la compaction d'assemblages granulaires mous au-delà du point de blocage. Ce cadre micromecanique s'appuie sur le tenseur des contraintes granulaires, sa limite aux petites déformations, et de l'évolution de la connectivité des particules. À partir de l'expression de ces quantités, nous établissons différentes équations de compaction, libres de tout paramètres *ad hoc*, et reproduisant parfaitement nos données numériques et expérimentales. Ces équations dépendent principalement de la dimension considérée (2D/3D), et prennent en compte les caractéristiques de forme, de bi-dispersité élastique, ou de géométrie de compression (uniaxiale *vs* isotrope). Le cadre micromécanique proposé permet d'unifier le comportement de compactage des assemblages de particules molles, molles/rigides et non circulaires de manière cohérente, à la fois en 2D et en 3D, pour une compression isotrope et uniaxiale.

A mi familia.

Acknowledgements

I would like to thank my supervisors, Emilen Azéma, Mathieu Renouf and Jonathan Barés, for the for their valuable guidance and exciting discussions during the thesis. I want to thank all the members of LMGC for the cordial conversations and the delightful moments lived throughout this time, especially to Luisa Orozco and Oscar Polania, wonderful people and brilliant scientists.

Finally, and most importantly, I want to thank my family for their unconditional support and patience. Especially to my father, Manuel Cárdenas-Farfán, my mother Maria Barrantes, and my sister, Marcela Cárdenas; this achievement belongs to you.

Contents

List of Tables

List of Figures

General introduction

Granular materials and especially deformable granular media are a valuable and indispensable part of countless natural phenomena and human activities. These materials are present from constitutive biological cells, foams, and suspensions to powder compaction, pharmaceutical industries, and food activities. On the other hand, mixtures of particles with different elastic properties have also received significant attention in recent years because of their innovative properties. In an engineering context, recycled materials such as rubber chip mixtures from wasted tires are usually employed to improve stress relaxation and foundation damping in building structures. The range of applications for soft/rigid mixtures is potentially broad and opens the door to an extensive field of fundamental topics that are still poorly studied.

Among the applications, the compaction of soft granular matter, especially beyond the jamming point, is a broad issue increasingly studied in the literature. Innovative experiments and advanced numerical methods have made it possible to take a step forward in the understanding of the microstructural evolution beyond the jamming point. However, despite their presence in so many scientific and industrial fields, the behavior of deformable particle packets is far from being fully understood. Understanding the physics behind these phenomena, especially the compaction, as a function of their different elastic properties, shape, size, and response to possible external loads would optimize many of the processes in which highly deformable particles are involved. Although in this direction, many equations that try to link the confining pressure to the packing fraction (i.e., the ratio between the volume of the particles over the box's volume) have been proposed, most of them are based on empirical strategies with no apparent physical bases.

We focus this work on the compaction behavior of deformable grain assemblies beyond jamming. Precisely, we study the physical effect of the proportion of soft/rigid particles in the packing, the effect of different particle shapes, the friction coefficient, and the dimensionality (2D/3D). Starting from the micro-mechanical definition of the granular stress tensor, we introduce an analytical model for the compaction behavior accounting for the evolution of particle connectivity, the applied pressure, and the packing fraction. Our model accurately predicts the sample density ranging from the granular jamming point to high packing fractions, considering the properties mentioned above. As a natural consequence, the bulk modulus evolution is also deduced.

The thesis is structured as follows. **Chapter 1** presents a brief overview of rigid and solid granular media behavior under compression, especially at the jammed state and above. The main advances in the field and the main numerical and experimental methods to study them are also presented. **Chapter 2** analyzes the isotropic compaction of soft/rigid mixtures and characterizes the evolution of the packing fraction, the elastic modulus, the strain energy, and some microstructural parameters such as the connectivity. A micromechanical model to describe the compaction, based on the characterization of one single particle under the same compaction conditions, is also proposed. The isotropic compaction of assemblies composed of soft pentagons interacting through classical Coulomb friction and its comparison with circular assemblies are presented in **Chapter 3**. The compaction model presented in **Chapter 2** is also revised and extends to noncircular regular particles. In **Chapter 4**, by mean of a recently designed experimental set-up, we analyzes the oedometric compaction of soft/rigid mixtures and extends and validates the findings in **Chapter 2**. In **Chapter 5**, we perform three-dimensional simulations for the isotropic compaction of an assembly of elastic spheres and test our theoretical framework. Finally, the main results of this thesis and comments on the perspectives of this work are presented.

CHAPTER 1

Introduction

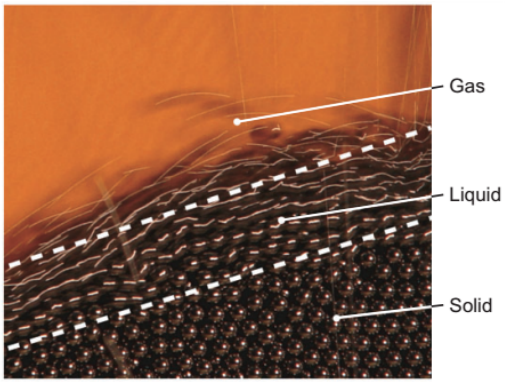

FIGURE 1.1. Solid, liquid, and gas regimes of beads flowing out from a pile [1].

This chapter presents a brief review of the behavior of granular media, with a particular focus on the solid behavior of granular assemblies. First, we evoke some general features of the dense state of hard granular assemblies, i.e., particles that do not deform (or deform only at the contact). Second, we focus the discussion on the soft granular assemblies, which is the main subject of this thesis. The principal advances in this field will be presented, in particular on their compaction. Subsequently, the current numerical frameworks and the most used experimental methods in this specific field are shown. We conclude with some open questions that emerge for the compaction of the soft granular assemblies.

1.1 Granular media

Granular media is present in everyday life. Such systems composed of an extensive collection of grains can be found in different scales, sizes, shapes, and elastic properties, making this type of material being studied in many scientific fields. For instance, they can be found at the microscale, like powders or biological cells [25, 26], at the mesoscale, in sands, cereal, soils, and roks [4], and finally at astronomical scales [27], like asteroids and rocky aggregates in, for example, the rings of some planets. Transversely, we also find them in numerous applications such as metal sintering [3], pharmaceutical processes [28], civil structures, and natural phenomena such as landslides or erosion [29] to name a few. The challenges in these applications are mainly in achieving the optimization of many of their manufacturing, handling, and maintenance processes to reduce energetic, economic, and temporal costs. For these reasons, an interdisciplinary study of granular media is needed, involving several branches of physics and mathematics.

Although these materials have been studied for many years, their theoretical modeling has not been a straightforward task, to the point that we still have not a unified description of their general behavior. Their complexity and difficulty to be modeled are due to the large set of particles that composed them, with a high local disorder, a large number of degrees of freedom, and their complex local interactions, both cohesive and non-cohesive, that often depends on the system scale. Also, the granular materials are not usually composed of particles of the same characteristics but rather of mixtures of grains with various sizes and shapes or elastic properties. Moreover, some of these particles can deform or, in extreme cases, break. In addition, granular matter presents high and complex energy dissipation processes far from the classical systems, preventing the use of the traditional tools of statistical mechanics to model their behavior. These characteristics result in different macroscopic behaviors, where granular matter exhibits properties typical of solid, liquid, or gaseous systems, or even all three states in a single phenomenon [1]. Such complexity is illustrated in Fig. 1.1 where it is shown the three different regimes present in the fall of beads from a pile. Here, assuming that the state is governed by (i) the inertial forces induced by the shear, and (ii) the static forces due to the confining pressure, it is possible to define a dimensionless number, the inertial number [30], from the ratio of these two forces. Small values correspond to the quasi-static state while high values correspond to the dynamic state.

In this direction, the jamming transition [31] that separates the fluid-like state from the solid-like state, when the inertia number goes to zero, has been one of the main topics studied in hard granular matter. In contrast, the study of systems made of particles with different elastic properties, that can exceed this jamming limit, as is the case for assemblies of particles that deform rather than break, has not made sufficient progress, whereas it is of greater importance in many real-life scenarios.

Indeed, the presence of assemblies of deformable particles in many natural and industrial processes makes the understanding of the physics of these materials and especially their response to different loading conditions, a topic of vital importance. We find them in emulsions [32–34], foams [17, 35], biological cells [2, 36, 37], clayey materials [38, 39], and metal powders [3, 40]. In particular, in the civil engineering context, is the case of composites of particles with different elastic properties, especially soft-hard mixtures, that exhibit new and fascinating mechanical properties such as better stress relaxation [41–43],

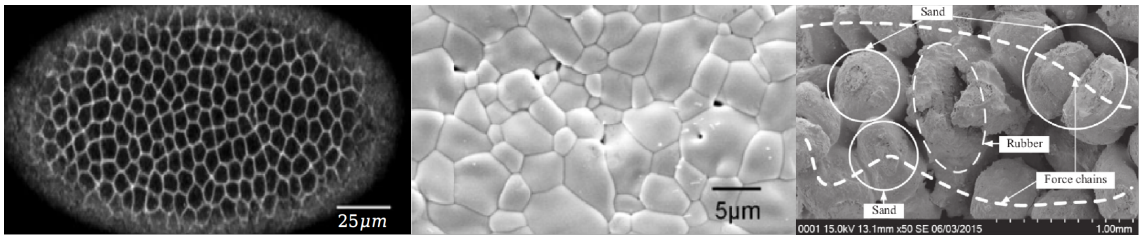

FIGURE 1.2. Example of soft matter assemblies. From left to right, epithelial cell growth [2], ceramic sintering [3] and rubber-sand mixtures [4].

seismic isolation [44–46], and foundation damping [42, 43, 47] while reducing the weight of the structures or increasing the packing fraction. Figure 1.2 shows some micrographs of different soft granular assemblies under different loading conditions.

In the following, we briefly review the significant results in hard granular packings, especially at the jammed state. This is followed by the most relevant result on the compaction of soft granular assemblies beyond the jamming point, including the most used and recent compaction equations found in the literature and the principal experimental and numerical methods used to study these materials.

1.2 Solid behavior of hard granular packings

1.2.1 The jammed state

The jammed state is defined as the mechanical state where all particles in the assembly are in equilibrium, such that the resultant force and torque on each of them are precisely equal to zero. These conditions are often presented in terms of the coordination number, Z, defined as the average number of contacts per particle, and in terms of the packing fraction ϕ, defined as the ratio between solid matter and the total volume of the packings (also named relative density or solid fraction). The mechanical equilibrium in the jammed state involves a balance between the number of degrees of freedom of the system and the number of constraints. For example, a granular packing of N d-dimensional frictionless particles has $NZ/2$ independent contact forces and dN force constraints. In the isostatic limit, where the condition of mechanical equilibrium is minimally satisfied, the coordination number Z is equal to $Z_{iso} = 2d$ for frictionless disks or spheres and $Z_{iso} = d(d+1)$ for frictionless non-circular or non-spherical particles, and coincides with the known Random Close Packing (RCP) [48,49]. For frictional particles $Z_{iso} = d+1$, but in reality, the critical

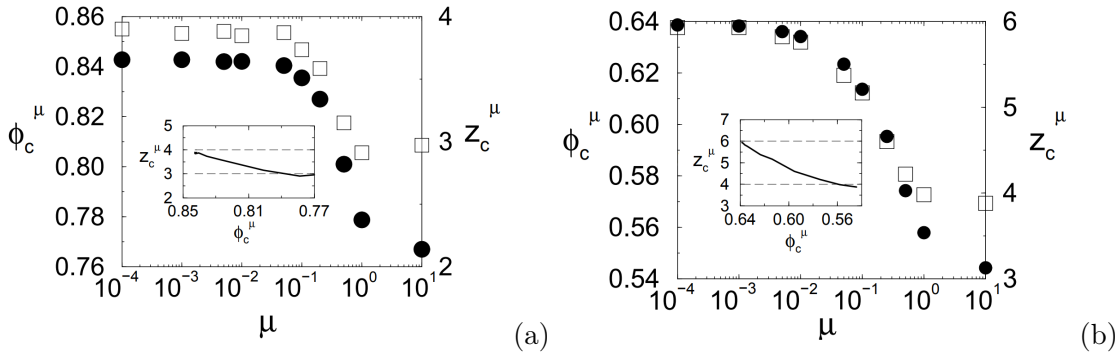

FIGURE 1.3. Coordination number Z_c^μ (open squares) and packing fraction ϕ_c^μ (filled circles) found at the jammed state as a function of the friction coefficient in (a) monodisperse packings of disks and (b) monodisperse packings of spheres [5].

coordination number varies in a range such that $d+1 < Z_{iso} < 2d$ for a random frictional packing of disks or spheres, and $d+1 < Z_{iso} < d(d+1)$ for a random frictional packing of non-circular or non-spherical packings, that depends on the friction coefficient. This is shown in Fig. 1.3 for packings of disks and spheres [5, 18, 50].

While the jammed state is well defined in terms of the coordination number through the number of degrees of freedom of the system, the same is not valid for the packing fraction. The disordered character of the packings makes the mechanical equilibrium condition to be fulfilled in a wide range of packing fraction values, which depends on the size and shape of the grains [51,52], the friction coefficient (see Fig. 1.3) [5,53], and even the initial conditions [54]. For example, the increase of the particle polydispersity is directly correlated to the increment of the packing fraction at the jammed stated, which also depends on the used grain size distribution as shown by Oquendo et al. in [55]. About the shape, some works have been done with elongated particles [6], non-convex particles [56], angular particles [57], and with hyper-spheres [58], showing the nonlinear relation between the parameters that define the shape of the particle and the jammed values of the packing fraction. For instance, Donev et al. in [6] showed the non-monotonic character of the jammed packing fraction of ellipsoidal particles in 3D as a function of their aspect ratio (the ratio of the major axis to the minor axis) (see Fig 1.4). Furthermore, they showed that it is possible to reach high jamming states of disordered packings and achieve values close to the ordered hexagonal configuration. This latter is the configuration with maximal packing fraction for a monodisperse packing of spheres.

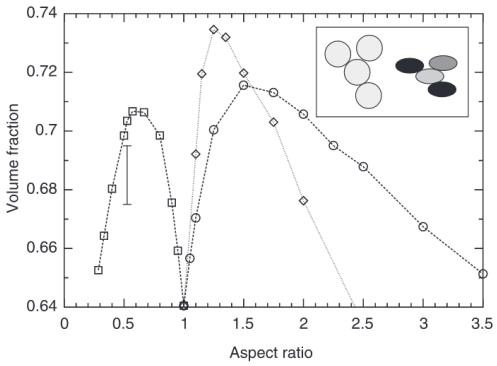

FIGURE 1.4. Packing fraction (Volume fraction in the figure) at the jammed state as a function of the aspect ratio of spherical particles with elongated shapes (circles) and flattened shapes (diamonds) [6].

1.2.2 Contact forces

Another aspect widely studied in the general context of granular media is the transmission of forces. In rigid or quasi-rigid granular packings (where deformations are far below the radius of the particles in contact), it is classically found that the contact force between particles is well described by the Hertz's elastic contact law [59]. In this law, the contact force between particles is repulsive and depends on the virtual deformation or interpenetration between the particles and their elastic properties. For instance, the contact force between two spherical particles and two cylindrical particles is given by:

$$f_n = \frac{2}{3}\frac{E}{(1-\nu_p^2)}R^{1/2}\delta^{3/2}, \tag{1.1}$$

and

$$f_n = \frac{\pi}{8}\frac{E}{(1-\nu_p^2)}L\delta, \tag{1.2}$$

respectively, with E the material Young modulus, ν_p its Poisson ratio, $R^{-1} = R_1^{-1} + R_2^{-1}$ the effective radius of the two particles of radius R_1 and R_2, and δ the particles' displacement and L the cylinder height.

Experimentally, although it is not possible to directly measure the contact forces on each grain, it is possible to indirectly get it by mean of inverse analysis. For example, in two dimensions, the most common method consists of loading birefringent particles. Observation between crossed polarisers shows fringes whose density is related to the local stress induced by the contact forces [7, 60, 60]. In three dimensions, historically, forces on

the edges have been guessed by measuring the diameters of discs on carbon paper marked at the contacts [61]. Figure 1.5(a) shows the stress chains in experimental assemblies of birefringent particles that have reached the jammed state. These chains and their heterogeneous distribution in the assembly result from the distribution of contact forces between particles. Figure 1.5(b) shows the interacting force chains in a simulation of spheres in the jammed state [8].

About the Probability Distribution Function (PDF) of those contact forces in the inside of the assembly, a well-known form is observed (see Fig. 1.5(c)). In these distributions, often called bimodal distributions [62, 63], at the jamming transition, the probability of having contacts with forces below the mean value, weak forces, increases following a power law. The weak forces are the ones that keep the internal equilibrium of the system. On the contrary, having contacts with forces above the mean value, strong forces, decreases with an exponential law [62]. The strong forces are the forces that mainly keep balancing the external deviatoric stresses of the system. About the shapes of the distribution, Radjai in [9] proposed a theoretical model that predicts the bimodal character of the distributions by analyzing the effects of steric constraints concerning the force balance condition (cf. red line in Fig. 1.5(c)):

$$PDF(f) = \beta(1+\gamma)\frac{\gamma e^{\beta f}}{(1+\gamma e^{\beta f})^2}, \tag{1.3}$$

with β and γ constants.

Generally speaking, the bimodal shape of the distributions is not significantly altered by the size polydispersity, the particle shapes, nor by changing friction in the system. For the case of polydispersity in size, the same potential-law behaviors are observed for weak forces but with longer exponential tails, making the distributions broader in close proportionality to the polydispersity [52]. Moreover, more tortuous force chains are observed for different particle shapes, with exponential decays very similar to spheres and disks, but with a lower density for weak forces and a more prominent peak above the mean value [8]. On the other hand, friction in the system increases the building of arches that supports a large part of the force chains and increases the presence of weak forces in the system [64, 65].

Moreover, based on the contact forces and the geometrical disposition of the contact network, it is possible to build the stress tensor of the packing [66]. To do so, we first

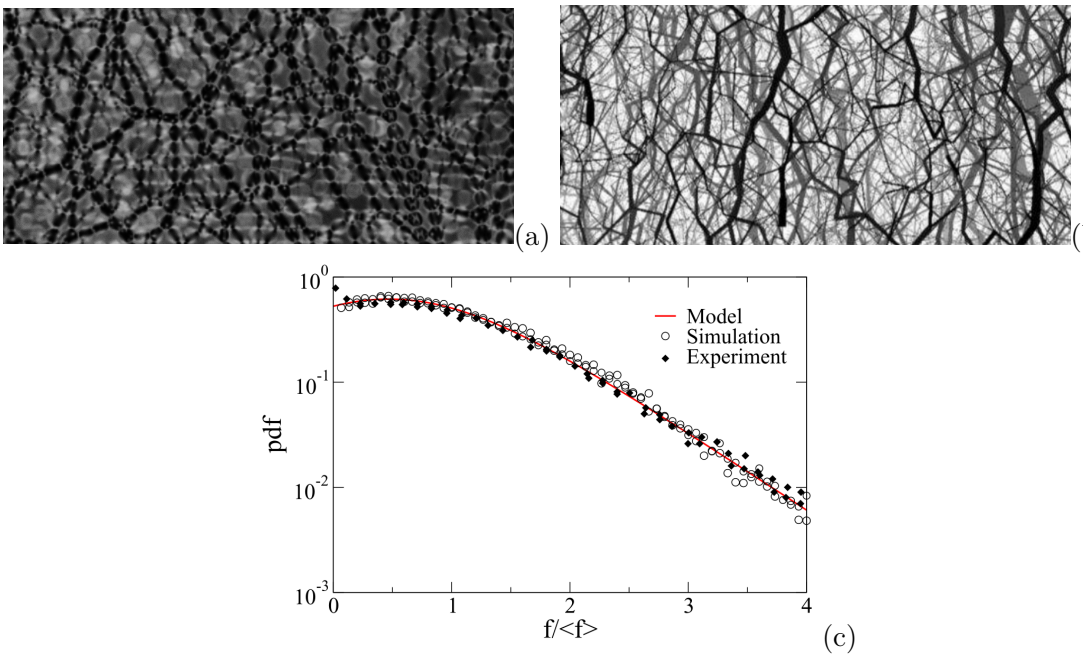

FIGURE 1.5. (a) Stress chains of an experimental oedometric compression of photoelastic particles in the small deformation regime. The color intensity (from white to black) is related to the stress in the particles [7]. (b) Snapshot of the normal contact forces in a packing of simulated spheres at the jamming point[8]. (c) The probability density function of the normal contact forces normalized by the mean value for granular experiments and simulations [9].

defined the internal moment, $\mathbf{M}^i$, on each particle i, as:

$$M^i_{\alpha\beta} = \sum_{c\in i} f^c_\alpha r^c_\beta, \tag{1.4}$$

where f^c_α is the α^{th} component of the contact force acting on the particle i at the contact c, r^c_β is the β^{th} component of the position vector of the same contact c, and the sum runs over all the contacts of the particle i ($c \in i$). The stress tensor $\boldsymbol{\sigma}$ in the volume V of the packing is given by the density of the internal momentum over this volume:

$$\boldsymbol{\sigma} = \frac{1}{V}\sum_{i\in V} \mathbf{M}^i. \tag{1.5}$$

With Eq. (5.2), one defines the mean stress, P, in a granular packing from the principal values $\sigma_{\alpha\alpha}$ of $\boldsymbol{\sigma}$, as (in 3D):

$$P = \frac{1}{3}(\sigma_{xx} + \sigma_{yy} + \sigma_{zz}). \tag{1.6}$$

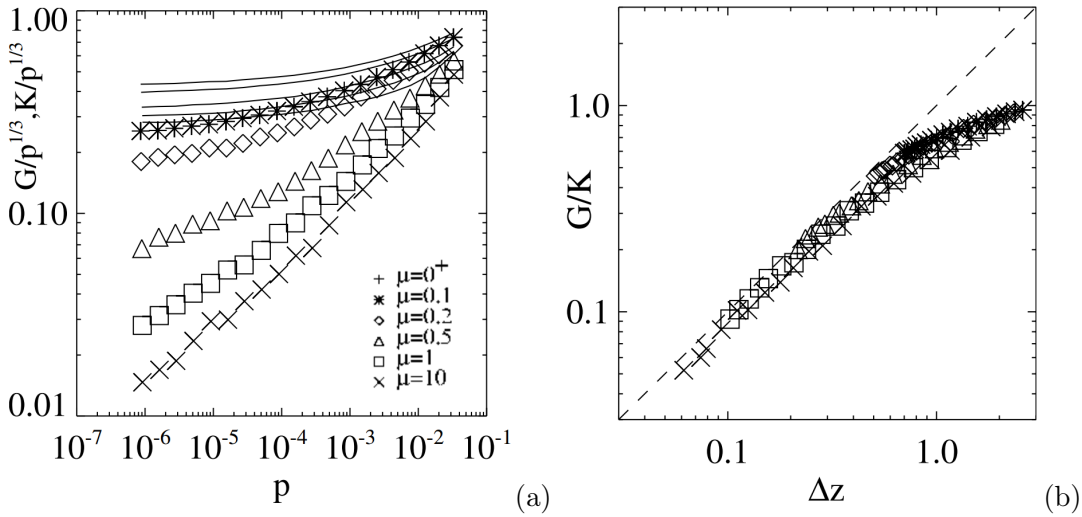

FIGURE 1.6. Molecular dynamic simulation on frictional disks [10]. (a) Shear modulus G and bulk modulus K (continuous lines) as a function of the applied pressure. (b) G and K as a function of the excess coordination number.

1.2.3 Elastic properties

One of the principal characteristics of soft particles is their elasticity. This is the material's ability to resist a deformation induced by an external loading and return to its original shape. The bulk modulus K and the shear modulus G are the two quantities that give some insight into that material's elasticity [59, 67]. The first one is defined as:

$$K = -\frac{dP}{d\varepsilon}, \tag{1.7}$$

with P the mean pressure in the packing (Eq. (1.6)), and ε the volumetric deformation of the material. K tells us about the material's resistance to the compression. The second one, is defined as:

$$G = -\frac{d(\sigma_{xx} - \sigma_{yy})}{d(\varepsilon_{xx} - \varepsilon_{yy})}, \tag{1.8}$$

with ε_{xx} and ε_{yy}, the principal deformations in the x and y direction, respectively. G tells us about the resistance to shear stress. For example, by knowing the evolution of these two quantities as a function of the applied stress or the compaction density, is it possible to study the wave propagation in a granular media and to compute its velocity [68, 69].

Under the framework of the Effective Medium Theory (EMT) [70, 71], where the particles are replaced by a network of bonds in contact, it has been shown that both the bulk modulus K and the shear modulus G vary as a power-law of the applied pressure ($\sim P^{1/3}$)

[10, 72]. However, experimentally, this law Has not been validated, mainly because of the increase of the number of particles in contact and the contact area that is not taken into account in EMT [71, 73, 74]. It is found that G and K evolve faster than the mentioned power-law, with a high discrepancy in the predicted values for K/G [10, 74, 75]. Nevertheless, it is possible to tell that EMT has a good qualitative description of K, and a much better description than G. Figure 1.6 shows the behavior of K and G as a function of pressure and the excess coordination number for frictional disks obtained by Somfai et al. [10].

1.3 Soft granular assemblies

In the previous section, we presented the description of granular assemblies in or near the jammed state. Their main characteristic is that the particles do not deform, or their deformation is minimal compared to the size of the particles. Although, as discussed at the beginning of this Chapter, the real world is also made of different types of particles that can achieve large deformations under different types of compaction. This characteristic of large deformability gives rise to new physics, and different mechanical properties often dismissed or simplified.

In those assemblies, in addition to the interaction properties (friction, cohesion, or repulsion) and rearrangements (sliding or rolling), the individual body deformation (related to the Young's modulus and the Poisson's ratio of the particle) is crucial to understand their bulk and mechanical behavior, especially in the compaction process. For instance, the high deformability of soft particles under confining pressure allows the packing fraction of the assemblies to easily pass the critical jamming point.

1.3.1 Compaction

The compaction of soft particle assemblies beyond the jamming point is in the center of several natural and industrial processes, such as cellular tissue growth [36, 37], ceramic sintering [76, 77], metal power compaction [3, 15], and pharmaceutical tableting [26, 28, 78] to name a few. Fig. 1.7(a) shows experimental results of Secondi on the oedometric compaction of different types of iron powders, where high values of packing fraction are achieved [11].

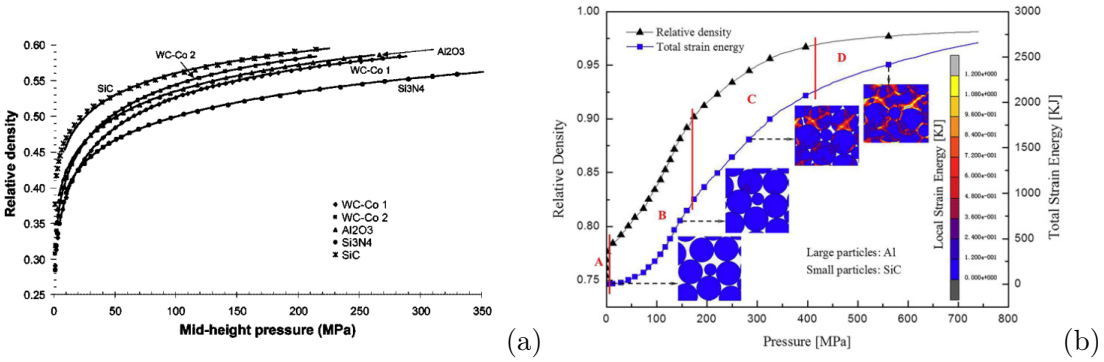

FIGURE 1.7. (a) Experimental results of compaction of different metal powders [11]. (b) Numerical results of the granular density and strain energy density of a metal mixture Al and SiC as a function of the loading pressure [12].

The compaction curves are often presented as the evolution of the packing fraction as a function of the loading conditions, showing, most of the time, a very similar qualitative and general evolution with the confining pressure. The quantitative differences are mainly given by the initial conditions of the compaction and the intrinsic properties of the materials. It follows a rapid increase of the packing fraction for low pressure, followed by an asymptotic increment towards a maximum value of the packing fraction. This behavior is described in four main stages by Huang et al. in [12] looking at the strain energy (Fig. 1.7(b)). In the initial state, region **A**, there is a sharp rise in the packing fraction, which is explained by the rearrangement of particles, with almost zero increment in the strain energy and not high deformations in the particles. In **B**, as the pressure continues rising, the packing fraction or relative density increases almost linearly with the pressure, and the strain energy starts to increase, where the elastic deformation is dominant. In **C**, at high pressures, large deformations are observed, evidenced by a rapid increase of the total strain energy. Finally, in **D**, the plastic deformation of the particles is dominant, where the deformation and the strain energy reach maximum values. This makes the packing fraction stabilizes to an asymptotic value.

Recently, Vu et al. [20, 79, 80] presented experimental and numerical studies on two-dimensional rubber-like particles. They find that first, the hyperelastic behavior driven by the neo-Hookean model [81], adopted in the simulations, reproduces the experimental tendency of the compaction performed on silicon disks. Second, they found that the different compaction evolutions, varying the Young modulus E and Poisson ratio ν of the particles, follow the same general behavior proposed by Huang et al., and qualitatively present very close concordance when scaled with the effective young modulus $E^* = E/(1-$

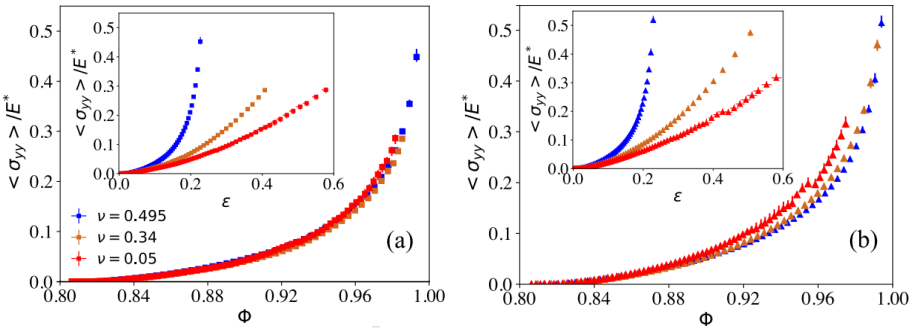

FIGURE 1.8. Stress in the y-direction scaled by the effective Young modulus of an oedometric compaction as a function of the packing fraction of particles with different Poisson ratios and friction coefficients equal to (a) $\mu = 0.2$ and (b) $\mu = 0.8$ [13].

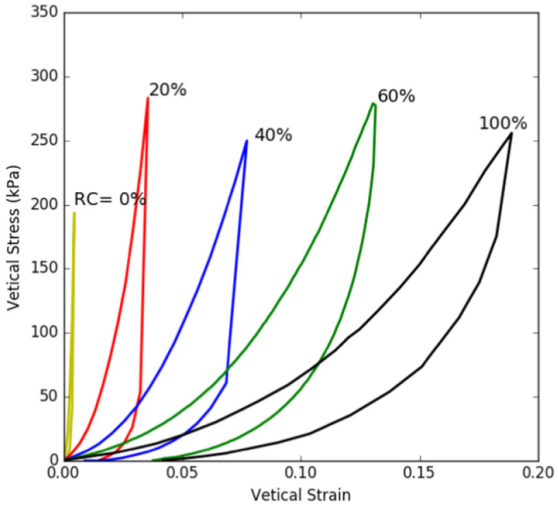

FIGURE 1.9. Stress in the y-direction as a function of the deformation in the same direction for experimental oedometric compaction of mixtures of sand and rubber particles. The percentage of rubber particles is denoted by RC. [14].

ν^2). Figure 1.8 presents the stress in the y-direction of oedometric compaction of particles with different Poisson ratios and friction coefficients, obtained by Vu et al. [13].

In addition, the compaction evolution of composites made of particles with different elastic properties, such as mixtures of soil particles with soft particles, show similar compaction evolution. They show a maximal packing fraction and maximal strain depending on the proportion of rigid particles concerning soft ones (besides the friction, shape, or size of particles) [4, 82] (see Fig. 1.9). This behavior implies that this kind of mixtures exhibit new properties such as better stress relaxation [42, 43, 83], seismic isolation [45, 46, 84] and foundation damping [42, 43, 47] while reducing the weight and keeping the strength of the structures.

1.3.2 Compaction models

The understanding and theoretical description of the compaction of soft granular matter as a function of different load conditions is still an open topic in many areas of science. One of the first constitutive equations to explain and predict the compaction curve in soft granular matter was proposed by Walker in 1923 [85]. This equation states that the packing fraction, ϕ, is proportional to the logarithm of the pressure ($\ln P$). The model involves two fitting constants, which have been later correlated to an equivalent Young's modulus or yield strength by Balshin et al. [86]. Shapiro and Kolthoff [87], followed by Konopicky [88] and Heckel [89], had a different approach and assumed the proportionality between the porosity or void ratio and the packing fraction ϕ increment over the stress increment:

$$(1-\phi) = k\frac{d\phi}{dP}, \tag{1.9}$$

with k, a constant of proportionality. They proposed that $P \propto \ln(1-\phi)$ with two fitting constants related to the powder properties. Later, Carroll and Kim [90] justified this equation by correlating the loss of void space in the packing and the collapse of a spherical cavity within an elastic medium and extended it by adding a parameter that states the maximal packing fraction ϕ_{max} reachable:

$$P = b\ln(\phi_{max}-\phi) + P_0, \tag{1.10}$$

where b is a fitting constant called the yield stress, which depends on the material, and P_0 a fitting parameter defined by the initial conditions of the compaction. Equation (1.10) is the currently most used model to predict the evolution of the compaction of any soft material.

Over the years, many other compaction equations have been proposed in the literature [91–95]. However, like the previous ones, they linearly relate the logarithm of the packing fraction and a polynomial function of P, with two or three fitting constants. Some models also introduce a maximum packing fraction ϕ_{max}, which depends on the grains' properties (shape, size, friction coefficient...) in the form of $P \propto \ln(\phi_{max}-\phi)$ [11]. Recently, double logarithmic functions have also been proposed by Ge et al. [96], Zhang et al. [24] and Wünsch et al. [78]. They linearly relate $\ln P$ to $\log\ln\phi$. Less usual, some authors have shown non-linear equations [76, 97–99], linking a functional form of P to a functional

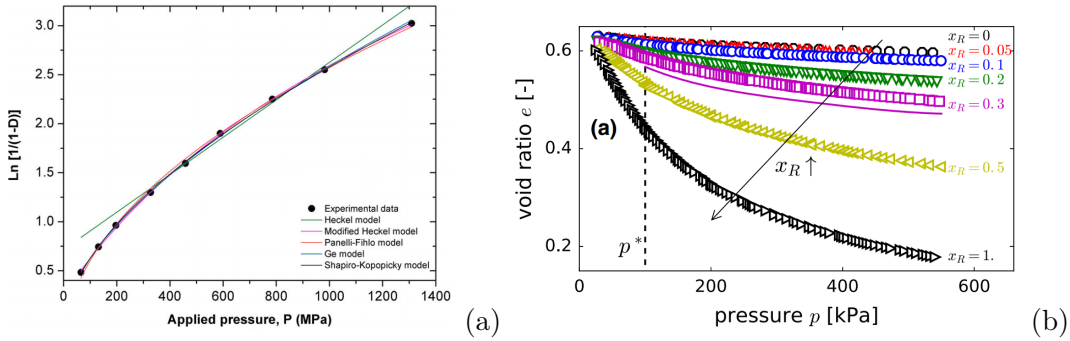

FIGURE 1.10. (a) Experimental compaction of a metallic powder together with the prediction given by some well-known compaction equations [15] (Tab. 1.1). (b) Pressure as a function of the void ratio (1 minus the packing fraction) of an isotropic compaction of experimental tests of sand-rubber mixtures done by Platzer et al. [16]. The solid line is the prediction given by the Platzer et al.'s model.

form of ϕ. An extensive list of equations, mainly for metal and pharmaceutical powders compaction, is reviewed in [15, 40, 100] and Tab. 1.1 displays the most relevant models among them. Figure 1.10(a) shows the compaction of a metallic powder, together with some of the compaction equations in Tab. 1.1.

For assemblies of distinct solid granular phases, the adopted strategies consist in using existing compaction equations for a single granular phase, and to fit free-parameter [77,101]. The first attempt to predict the compaction behavior of mixtures of rigid-soft particles can be attributed to Platzer et al. [16], who studied mixtures of sand with rubber particles (see Fig. 1.10(b)). They introduced an equation involving parameters related to the initial geometrical and mechanical conditions of the compaction, not considered in other models, and the intrinsic elastic properties of the particles. From the assumption that the void space is filled, they deduced a first-order differential equation of the applied pressure. The Platzer et al. equation is as follows:

$$e(\kappa, P) = e(0, P) - \kappa f^* - \kappa(F - f^*)\left[1 - \exp\left(\frac{P^* - P}{P_0(\kappa)}\right)\right], \tag{1.19}$$

with κ the mixture ratio, e the void space $(1-\phi)$, $e(0, P)$ the experimental void fraction at pressure P for the rigid particles, $P_0(\kappa)$ and P^* two characteristic pressures. $f^* = f(\kappa, P^*)$ and $F = f(\kappa, P \to \infty)$ are the critical deformed fraction and the maximum deformed fraction of rubber, respectively. Equation (1.19) rewritten in terms of the packing fraction

Author	Equation	Year
Walker [100]	$m_1 \ln P = a_1 \phi$ (1.11)	1923
Heckel [89]	$P = b \ln(1-\phi)$ (1.12)	1961
Huang [40]	$\log P = a_3 + m_3 \log \ln \left(\frac{\phi_{max} - \phi_0}{\phi_{max} - \phi} \frac{\phi}{\phi_0} \right)$ (1.13)	1982
Shapiro et al. [92]	$b_4 P^{1/2} + k_4 P = a_4 + \log \ln \left(\frac{1}{1-\phi} \right)$ (1.14)	1993
Ge [96]	$b_5 \log P = a_5 + \log \ln \left(\frac{1}{1-\phi} \right)$ (1.15)	1995
Panelli et al. [93]	$b_6 P^{1/2} = a_6 + \ln \left(\frac{1}{1-\phi} \right)$ (1.16)	2001
Secondi [11]	$b_7 P^{m_7} = \ln \left(\frac{\phi_{max} - \phi}{\phi_{max} - \phi_0} \right)$ (1.17)	2002
Zhang et al. [24]	$logP = a_8 + m_8 \log \ln \left(\frac{\phi_{max} - \phi_0}{\phi_{max} - \phi} \frac{\phi}{\phi_0} \right)$ (1.18)	2014

TABLE 1.1. Most used and relevant compaction equations for deformable materials. According to the authors, a_i, b_i, and m_i are constants that depend on different properties of the materials.

ϕ takes the form of:

$$P(\kappa,\phi) = -P_0(\kappa)\ln\left(\frac{[\phi_{max}-\phi]+[\phi(0)-\phi_{max}(0)]}{[\phi_{max}-\phi^*(\kappa)]+[\phi_0^*(0)-\phi_{max}(0)]}\right)+P^*, \tag{1.20}$$

with $\phi_{max} = \phi_{max}(\kappa)$, $\phi(0) = \phi(\kappa = 0, P)$ the packing fraction evolution for a pure sand sample, $\phi_{max}(0) = \phi_{max}(\kappa = 0)$ the maximum packing fraction obtained for a pure sand sample, and $\phi_0^*(0) = \phi_0^*(\kappa = 0)$ and $\phi^*(\kappa)$ the packing fraction for a pure sand and a mixture rubber-sand, respectively, at the characteristic pressure P^*. Nevertheless, the authors mentioned that their model provides fair predictions for low pressures and a ratio of rigid to soft particles below 50%, but it loses its accuracy for high pressure. It is worth noting that the model of Platzer et al. is a more general form of the previously mentioned models. Figure 1.10(b) shows the typical curves for compaction for granular mixtures.

Although most of the models above provide acceptable predictions on specific cases, their limitations are due to (*i*) the use of parameters without clear physical meaning, (*ii*) the lack of physical derivation, and, for many of them, (*iii*) the limitation to a single solid granular phase.

1.3.3 Microstructural features

The extensive range of results of compaction of soft granular packings of a broad kind of materials using different techniques have in common some fundamental findings. Up to the maximal packing fraction, it has been observed that the excess coordination number, $Z - Z_J$, as a function of the excess packing fraction, $\phi - \phi_J$, follows a power law with an exponent $\alpha \approx 0.5$ in both 2D and 3D cases, and for different materials [51, 80, 102], with the subindex J indicating the value at the jamming point. Figure 1.11(a) shows the coordination number as a function of the packing fraction in experiments of foams [17]. In addition, although the critical values, defined by the jamming, for the coordination number and the packing fraction change as a function of the friction (the higher is the friction between the particles, the lower is the coordination number and packing fraction of the jamming point), the above power laws do not vary significantly [51, 103].

On the contrary, looking at the structure of contacts and local pressure properties, a continuous and smooth transition is observed in the probability distribution function of normal contact forces, and local stresses inside the packing [101,104,105]. The distributions

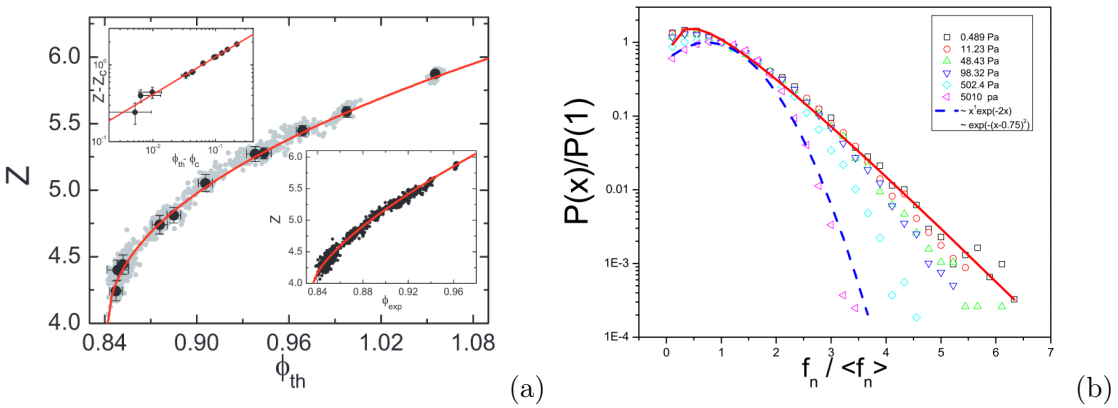

(a) (b)

FIGURE 1.11. (a) Coordination number as a function of the packing fraction in experiments of foams. The solid red line is a power-law fit with an exponent equal to (0.50 ∓ 0.02) [17]. (b) The probability density function of the normal contact forces in compressed emulsion under different load pressure [18].

start from the typical bimodal distributions observed in hard particle packings at the jammed state to completely homogeneous distributions with well-defined Gaussian shapes and a decreasing relative standard deviation as the highest density level is reached. Figure 1.11(b) shows part of the continuous transition to homogeneous states of the probability distribution function of normal contact forces. Other quantities such as the deviation from the affine motion, particle rearrangements, and particle rotations are significant and depend on interparticle friction, and macroscopic stress, displaying different plasticity effects in the granular material [18, 51, 104]. Moreover, the elastic and shear moduli depend mainly on the contact area between particles that increases during compaction, which is also related to the change in the coordination number [72, 106].

Furthermore, experimental and numerical studies in emulsions and foams have shown that the shear modulus obeys a power-law scaling with the excess packing fraction $(\phi - \phi_J)$, with an exponent close to 0.8 [107, 108]. Likewise, the specific contact length, defined as the average of the ratio between the contact length and the particle perimeter, follows a linear tendency with the same excess packing fraction [23].

1.4 Numerical methods and experimental techniques

This section introduces the numerical and experimental methods currently used to model quasi- and highly deformable granular media under different loading conditions. We also briefly explained the numerical framework and experimental method used in this work.

1.4.1 Numerical methods

Discrete Element Methods

To model the behavior of granular media, there are classical approaches known as Discrete Element Methods (DEM) [109]. The term *classical* underlines the fact that the bulk behavior of each particle is considered rigid. By combining the equation of motion written for each particle and a set of contact laws (Coulomb friction, cohesion, long-range interactions...), it is possible to simulate the evolution of such systems in numerous configurations, from quasi-static to dynamic.

Although many specificities differentiate the many existing methods, DEM can be classified into two main categories [110]: smooth (i.e., allowing grains interpenetration) and nonsmooth approaches (i.e., based on non-regular mechanics that take into account interactions without grain interpenetration).

For smooth approaches, the contact forces are explicitly expressed as a function of the overlapping between particles [111–113]. For elastic interactions in the normal direction, the most common law used is the Hertz law from Eq. (1.1) as follows,

$$\vec{f_n} = \frac{4}{3}\left(\frac{R_i R_j}{R_i + R_j}\right)^{1/2} \frac{E_i E_j}{E_i + E_j} \delta^{3/2} \hat{n}_{ij}, \tag{1.21}$$

where R_i is the radius of the particle i, E_i is proportional to the Young modulus of the same particle, and δ_{ij} is the overlapping between the two interacting particles.

In the case of frictional contact, a tangential interaction is added [114]. Generally, these tangential interactions assume that when two particles touch each other, a spring-like force acting in the tangential direction appears and couples the two bodies. This force acts against the tangential relative displacement and satisfies the Coulomb criterion for static-sliding friction. As soon as the bodies stop touching each other, the spring disappears.

The particle motions are thus twice differentiable, and the equations of dynamics can be integrated by conventional methods. For instance, in this category, we have the well-known DEM methods developed by Cundall, whereby considering Hertz contact together with regularized Coulomb friction laws [109], and Molecular Dynamics (MD) extended

to granular media by Allen and Tildesley [115]. Regularised laws introduce an artificial elasticity related to the normal contact stiffness, denoted by k_n. In simple geometries such as disks, the elasticity can be related to the deformation of the grains by correctly choosing the value of k_n, which is no longer possible when the geometry becomes more complex (polygons, for example). The presence of a contact stiffness induces the choice of small-time steps (mass-spring system) and most of the time requires the introduction of a damping parameter for numerical stability reasons [82, 116, 117].

For nonsmooth approaches, the philosophy is different; overlapping between particles is not allowed. Consequently, contact forces are described using inequalities. For example, to express the unilaterality of the contact, one use the well known Signorini condition given by

$$\begin{cases} \delta = 0, & \begin{cases} v_n = 0, & f_n \geq 0 \\ v_n > 0, & f_n = 0 \end{cases} \\ \delta > 0, & f_n = 0, \end{cases} \tag{1.22}$$

where f_n represents the contact force, δ the distance between particles and v_n denotes the normal relative velocity. The existence of such a relation is related to Jean Moreau [66]. As for smooth approaches, it is possible to account for friction. In the case of inequalities, the Coulomb friction can be expressed as:

$$\begin{cases} \delta = 0, & \begin{cases} v_t < 0, & f_t = \mu f_n \\ v_t = 0, & -\mu f_n \leq f_t \leq \mu f_n \\ v_n > 0, & f_t = -\mu f_n \end{cases} \\ \delta > 0, & f_t = 0, \end{cases} \tag{1.23}$$

where v_t represents the tangential component of the contact relative.

The solution of the contact problem results from the intersection of such inequalities and the equation of motion. The absence of overlapping between particles allows the use of large time step but need iterative algorithms to solve the contact problem. In the context of granular media simulation, the best-known method is the Contact Dynamics method (CD) developed by Moreau [66], but we can also mention the method developed by Baraff in the context of Computer Graphics [118] or the approaches used in the simulation of multibody systems [119].

In summary, the DEM can be seen in three basic steps: (*i*) a network of potential contacts is defined, (*ii*) the velocities and contact forces are computed from the equations of motion together with frictional contact relations, and (*iii*) the particle positions and rotations are updated.

DEM for soft particles

The extension of smooth and nonsmooth DEM methods to include the deformable character of the particles can be treated in different ways.

One way is to increase the allowed overlapping and to associate it with the grain deformation like in MD approaches. Although this approach is debatable in terms of the actual representation of the particle shapes, it is possible to obtain interesting results, in the small deformation domain, in the compaction of packings of hard [106] and deformable particles [82, 112], and the mixture of both [82]. For example, Harthong et al. [120] proposed a contact model, High Density model (HD model), where the contact force depends on both the overlapping between the particles in contact and the available space in the Voronoi element defined by the contacts of each particle, such that this repulsion force tends to the infinity when the void space tends to zero.

Another solution is to change the intrinsic behavior of the particles from rigid to purely deformable behavior through meshless and mesh approaches like Finite Element Methods (FEM). For instance, Fig. 1.12 shows the comparison of DEM-FEM and MD made by Harthong et al. [19] in the boundary stress of oedometric compaction of 32 spheres as a function of the packing fraction (or relative density). In the MD simulation, two different contact models were used, the model of Storåckers et al. [121], and the HD model. [120]. It is seen that, in this particular example, the three methods show a good agreement for medium relative density, but with some discrepancies for high densities, especially using MD with the Storåckers contact model.

BPM

One other alternative is the Bounded Particle Method (BPM). In BPM, the particles are considered as a connected system of sub-particles through bilateral or cohesive laws depending on the type of particles and the type of deformation to model [122–124], which

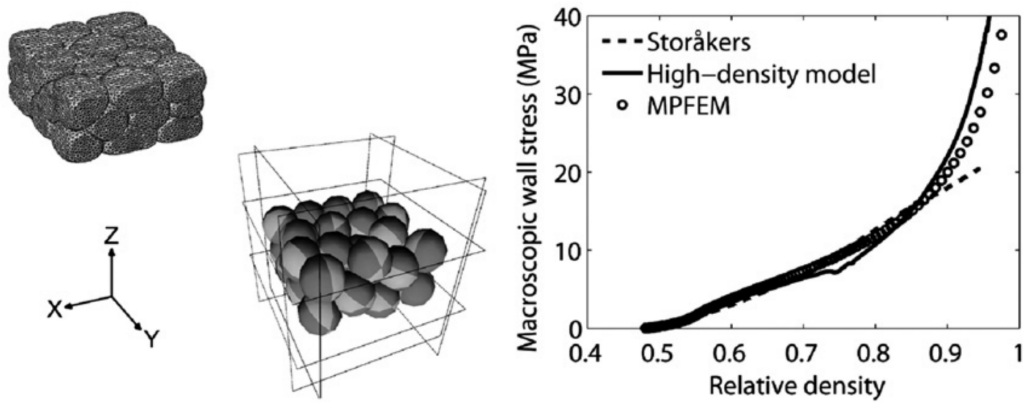

FIGURE 1.12. Boundary stress of oedometric compaction of 32 spheres as a function of the packing fraction (or relative density) using DEM-FEM (Multi Particle - FEM) and MD with two different contact models, the model of Storåckers et al., and the High-Density model of Harthong et al. [19].

can resist normal force, shear force and bending moment. One of the main advantages of this approach is its low computational cost. For example, in this group of BPM, we have the recent works of Asadi et al. [14]. They simulate the compaction of sand mixtures with deformable particles. The sand particles are simulated as a rigid cluster of spheres that do not move relative to each other, and the deformable particles by agglomerates of bonded spheres, following a linear elastic and cohesive law.

Meshless approches

In mesh-free models, generally, a continuous law of the material's behavior to be studied is used. It is discretized in different ways without using Finite Elemets methods (FEM), such as mass points, for example, in the case of Material Point Methods (MPM) [99], or in the use of nodes subjected to deformation fields [125]. In the last case, the work of Mollon [125] avoids using FEM by employing material points or nodes subject to a deformation field that carries the system's degrees of freedom. The continuous deformation field is interpolated between the nodes by means of a moving Least Square algorithm. In these types of approaches, it is also necessary to calibrate some fundamental computational parameters from a priori experimental measurements, such as the stiffnesses and viscosities [99, 125].

DEM-FEM approaches

In meshed approaches, a volumetric model associated with a state equation law of each grain is considered. In this case, FEM-like methods are used to describe the particle deformations, keeping (or not) the integrity of the particles (DEM-FEM) [12,101,104,120]. In contrast to other methods, although computationally expensive, DEM-FEM strategies have the advantage of closely representing the geometry and bulk properties of the particles. These methods are based on finite element methods to solve the continuous mechanics at the particle scale and solve their constitutive equations by considering the external contacts and the friction interactions between particles. It is possible to distinguish mainly two classes of DEM-FEM methods, (*i*) the Multi-particle Finite Element Method (MPFEM) [104, 126–128] (see Fig. 1.12 and Fig. 1.13(b)), in which regularized contact interactions are used, and (*ii*) the Non-Smooth Contact Dynamic Method (NSCD) [66, 129] (see Fig. 1.8 and Fig. 1.13(a)), in which non-regularized contacts laws are used. The first MPFEM simulations were performed by Mesarovic et al. to study the deformation mechanisms in a periodic configuration of dissimilar elastoplastic spheres [130]. For granular random packings, the first MPFEM studies were conducted by Gethin et al. in 2002 [126] and Chen et al. in 2006 [131] in two and three dimensions, respectively, and mainly in the context of metal compactions.

NSCD was developed by Jean [129] and is an extension of the Contact Dynamics method (CD) initially presented by Moreau [66]. The first work done on elastic media using NSCD dates back to the 2000s by Acary et al. [132] with their work in masonry, followed by Cao et al. in 2011 [133], who tested the method on the compaction and shearing of deformable granular packings. The latest works on deformable packings using NSCD correspond to Vu et al. [13,23], who studied the oedometric compaction of highly deformable particle assemblies in two dimensions. To our best knowledge, three-dimensional studies using NSCD on the compaction of spheres using different load conditions have not been implemented so far.

The NSCD method is the numerical method used to study the compaction of granular soft and soft-rigid assemblies in this work mainly because of its accurate description of the particle deformations and contacts, treating the contacts between rigid and soft particles without distinction of behavior, with good accurate results up to high densities.

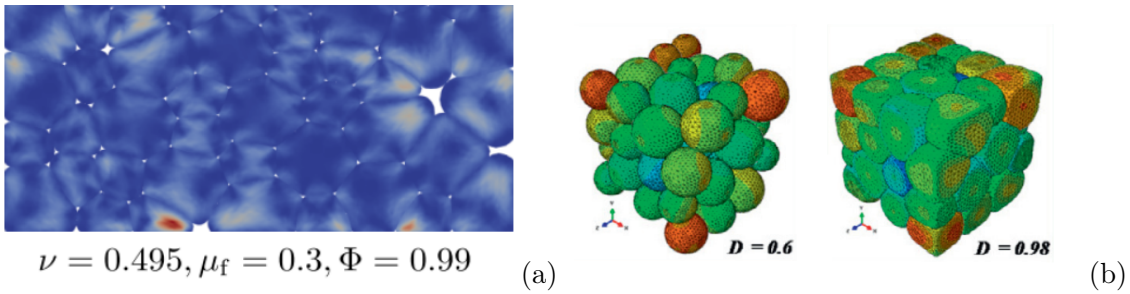

(a) (b)

FIGURE 1.13. (a) Two-dimensional simulations of a frictional soft particle assemply under oedometric compression using NSCD. The color-intensity is related to the strain energy within the particles [20]. (b) Three-dimensional simulations of a soft particle assemply under oedometric compression using MPFEM [21]. In both cases, the color-intensity is related to the mean stress within the particles.

1.4.2 Experimental methods

Experiments are needed

In essence, natural phenomena are infinitely complex, especially the ones involving granular matter. Indeed, in something as simple as a flowing dune, for instance, grain shapes, sizes, constituents, and initial positions are of infinite diversity and interaction between each grain, and the rest of the system is ruled by many physical processes as complex and diverse as capillarity attraction, contact repulsion, friction, thermal dilatancy, and fluid-structure interaction to name a few. When trying to model such a physical phenomenon, it is not possible to consider the whole complexity of the problem. On the contrary, one tries to keep as minimal as possible the number of variables (circular shape, bidisperse, rigid) and interaction processes (repulsive interaction, friction) that permit to reproduce the key observables of the natural phenomenon. This is the concept of *model experiment* that we have followed during the experimental study presented in this manuscript. Of course, numerical simulations also follow the same precepts adding an extra layer of simplification on the geometry and the interaction laws. Still, they permit to easily vary the input parameters of the phenomena. This allowed to make significant progress in many areas of physics, especially in granular media over the last decades.

Although the numerical methods closely reproduce the natural laws of granular media by using different hypotheses, such as those explained briefly in previous sections, they often do not fully represent the actual behavior of systems with all their complexity. In some cases, these simplifications still permit to match numerical results with experimental

ones, but in some others, a certain level of complexity needs to be added to be more realistic. This is why we have chosen to couple the numerical study with an experimental approach in this work.

Also, even if the numerical approach reduces the complexity, which allows a clear focus on specific parameters, sometimes challenging to obtain experimentally, the experimental approach (*i*) permits to validate the hypotheses used and the results found with the numerical methods, and (*ii*) permits to observe the actual and complete behavior of the system, allowing to see variables or phenomena that in some way could be overlooked by the physical hypotheses used in the numerical simulations.

One of the interesting and, at the same time, challenging aspects of the study of granular media is their intrinsic multi-scale character. From a global point of view, many macroscopic parameters allow a general bulk description of these media, such as the global deformation or reaction to the loading conditions. In a certain way, this does not require very elaborated experimental arrangements to be measured and many standard procedures have already been established [134–136]. From a more local perspective, at the grain scale, many phenomena responsible for the global behavior occur. So, a more structural and mechanical description of the system at this scale is necessary to understand the full behavior of the granular matter. This scale has descriptors such as the connectivity of the contact network and its structure porosity for example. Here, more advanced experimental techniques combined with a good resolution imaging, efficient image analysis and particle tracking algorithms, developed in the last decades, must be used [136–138]. If the stresses involved in the process are small enough, this level of observation is enough. However when stresses get higher and forces between particles are enough to significantly deform particles, it is necessary, not only to get particle displacements but also to measures these forces. In these cases the most common methods used an *inverse analysis* approach: A local measurement is done, most of the time optically, and forces are guessed such that the Hertz contact model, the superposition principle and the force balance fit the measurements. This for example how photoelastic method works [60, 139]. If the stress level is even higher, the Hertz contact model is not valid anymore and this method cannot be used. In this case it is need to examine the system directly below this micro-scale, inside the grains. Making experimental measurements at this sub-micro scale, is even more challenging. This is due to the difficulty of accessing this scale of the material and being able to measure at the

same time the behavior of each particle as a consequence of the different strains and stresses applied at the global system. Moreover, the difficulty is even greater due to the highly deformable character of the particles. Nevertheless, some experimental advances have been presented these recent years to address some of these challenges [23]. In the following, we present a brief review of these last and most common experimental methods.

Main experimental techniques

Historically, the first experimental work performing local measurements in granular media, combining grain detection and tracking algorithms with advanced image analysis methods, was performed on dry granular fluids [136, 136, 140–143]. They measured, for example, parameters such as kinematic profiles, effective friction, and global deformations, among others. Subsequently, these methods were adapted to study rigid granular systems, especially near the jammed state. To do so, since displacements are not relevant anymore, one needs to be able to measure the network of forces at the local scale when the system transitions from dynamic to jammed state. The first works in this direction focused mainly on the particle on the boundaries, directly evaluating the contact forces using the Hertz approximation and the surface in contact [144]. For rigid systems, this is a reasonable estimation, considering that the deformations are very small. However, it is not valid for deformable systems, and is only applicable to study particles on the boundaries.

To have an adequate analysis of granular systems near the jamming point, the interactions at the contact and only at the boundaries is not enough. It is also necessary to know what is happening inside of the system. Over the last decades, several experimental techniques have been presented to analyze the structure and micromechanics of confined granular systems, both in rigid and deformable assemblies. Most of the time, they rely on an inverse analysis approach. Among them, the most relevant experimental setups used photoelastic particles [50, 60, 139, 145–147], where their materials present different characteristics of birefringence as a function of the internal stresses on the material. When such materials are subjected to external stress and illuminated with a polarized light source, depending on the local stress, it refracts the light with different polarization angles. The refracted and polarized light can then be measured with high-precision imaging methods and the angle of polarization computed. Then, having the polarization changes and intensity of the refracted light, it is possible to obtain the values of the forces acting locally

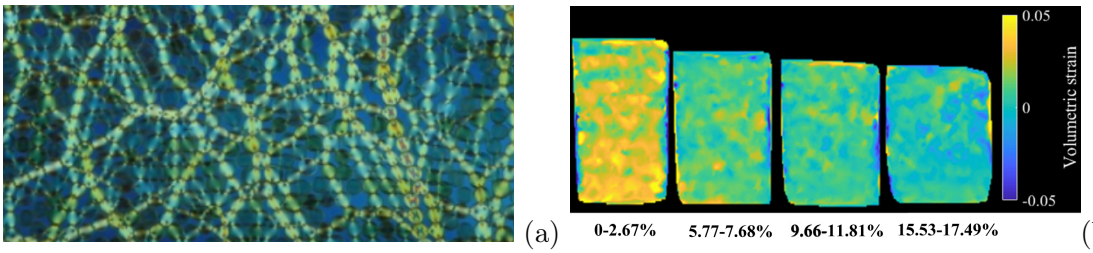

(a) (b)

FIGURE 1.14. (a) Stress chain of a oedometric compression of photoelastic particles in the small deformation regime. The color-intensity is related to the stress on the particles [7]. (b) Strain field distribution on a 2D slice of a sand-rubber sample at different shear stages [22].

in the particles via an inverse analysis method or a direct heuristic method. In recent reviews [60, 139] a description of the algorithms and the steps for building an experimental apparatus and samples using the photoelastic method is presented. This method has been used to study the statistical properties of granular materials under shear and near jamming [7, 145], the sound propagation [148], and the compaction of semi-rigid materials [146], among others. Figure 1.14(a) shows the refraction of light of compressed birefringent materials, from which the stress chains can be extracted. Inverse analysis can not only be coupled with photoelastic measurement but also with DIC algorithms [149–153]. In this latter case, instead of fitting a photoelastic pattern to guess applied forces, the displacement field is fitted.

These inverse methods have also been extended to three-dimensional analysis and applied to digital tomography of different granular materials. The tomography techniques use the refraction of X-Rays on materials that change their density or refractive index as a function of the local pressure exerted on them. Small changes in these intrinsic properties of the granular material allow the recovery of their geometry and mechanical structure. The versatility of this technique permits its use in assemblies of particles with different shapes [154], assemblies of deformable particles [152], and also mixtures of rigid-soft particle assemblies [22]. Figure 1.14(b) shows the resultant strain field distribution of a sand-rubber sample under simple shear. However, these approaches mainly rely on Hertz contact law, so they are limited to small deformations.

Digital Image Correlation (DIC) for highly deformable packings

For deformable grain assemblies, especially grains that allow large deformations, the photoelastic method is not very useful anymore because the birefringent signal saturates, and

it is not possible to assume small deformations to perform the inverse analysis. The previously presented DIC method cannot be used either precisely for the same latter reasons. It is thus necessary to set up a new method. Usually, in mechanics, when one needs to measure large deformations, the most common method consists in performing an accurate DIC algorithm without any assumption on the material behavior. The challenge in the case of granular matter is to be able to perform precise imaging on the whole system, which is, a priori, very large. This challenge has been tackled using a new kind of imaging device. This was first used by Lo et al. [23, 79] in the case of oedometric compaction of hyperelastic and plastic particles. In these works, they built samples of deformable particles close to the jammed state, and using a high-resolution imaging flatbed scanner and a large deformation DIC algorithm, they measured the evolution of the displacement field inside each particle during compaction. As a result, they deduced local and macroscopic quantities such as the deformation tensor, the particle shapes and solid rigid motion, as well as the contact network, and packing fraction, among others [23, 79].

The DIC algorithm initially builds a grid of material points attached to a random black and white pattern painted on the particle bottom. These points will be tracked all along the loading process. The size of the grid is chosen according to the required precision of the displacement field, up to a minimum size given by the image resolution and random pattern correlation length. With the evolution of the position of the particles and of the points in the grid, it is possible to compute the displacement fields inside each grain of the assembly $\mathbf{u}(\mathbf{X}, \mathbf{t})$ at each time or compaction step [23, 79]. Finally, the deformation gradient tensor $\mathbf{F}$, is defined from the displacement field [155]:

$$\mathbf{F} = \nabla_{\mathbf{X}} \mathbf{u}(\mathbf{X}, \mathbf{t}) + \mathbf{I}, \tag{1.24}$$

with $\mathbf{I}$ the identity tensor. Then, the Cauchy-Green strain tensor $\mathbf{C} = \mathbf{F}^T\mathbf{F}$ is computed. Figure 1.15 shows the force evolution as a function of the packing fraction (experimentally using the extended DIC method, numerically using NSCD (Infinitesimal FEM in the figure)) in an oedometric compaction of an assembly of highly deformable cylinders (a), together with the energy field in the assembly (b) numerically and (c) experimentally, performed by Vu et al. [23]. It is observed that both the experimental and numerical methods have an excellent agreement until the end of compaction, showing the effectiveness of the

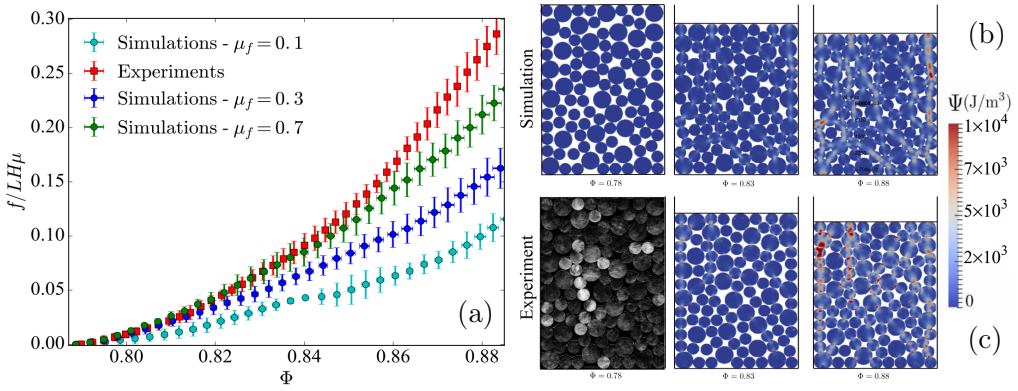

FIGURE 1.15. (a) Evolution (Experimentally using the extended DIC method and numerically using NSCD) the force evolution as a function of the packing fraction in an oedometric compaction of an assembly of highly deformable cylinders [23]. (b,c) Snapshots of the oedometric compaction, (b) simulations, and (c) experiments, where the color scale represents the strain energy of the particles [23].

NSCD approach and the great capabilities of the extended DIC method applied to the experiments.

Considering that in the compaction of granular mixtures with different elastic properties (as in mixtures of soft particles with rigid particles) large deformations occur at the particle scale, we used the latter experimental method to achieve an adequate measurement of the structural properties of such mixtures.

1.5 Conclusions

The behavior of soft granular packings beyond jamming under different loading conditions is widely investigated in the context of industrial and engineering purposes, yet it remains misunderstood. On the one hand, in the jammed state, systems composed of particles with different shapes, sizes, and elastic characteristics, among others, show clear transitions in their mechanical and geometrical properties. On the other hand, the evolution of these quantities, deep in the jammed state, is not yet entirely clear for highly deformable systems. Some numerical and experimental studies show the evolution of some of their mechanical and geometrical properties after the jamming point. However, numerically, most of them are studies on systems composed of discs (in 2D) and spheres (in 3D) with no real deformation (mainly with virtual deformations that allow overlappings) or do not take into account aspects of shape and elastic properties of the particles. Experimentally,

a clean study presents major challenges, especially in measuring local quantities on the scale of particles and contacts.

To achieve high packing fractions, it is generally necessary to apply different external loads that compress the granular packings, such as oedometric, isotropic compactions, or sheared compactions. Much of the research has been aimed at describing the behavior of their compaction curve (pressure vs. solid density) and trying to reduce its description into fundamental physical parameters. However, in most of the results, there are only empirical models with few fitted parameters, without a clear physical meaning.

This thesis aims to show the evolution of the microstructure and micromechanics of two and three-dimensional particle systems, not necessarily circular, highly deformable, and with different elastic properties, subjected to isotropic loading conditions. Also, to develop a theoretical approach that describes and predicts the evolution of the compaction in terms of well-defined and easily measurable physical quantities. To do so, we will use, for the numerical part, the NSCD approach, mainly because of its versatility in handling deformable and rigid particles, and its accurate calculation of the real particle deformations since overlapping between particles is not allowed. In the experimental study, high-resolution image analysis with DIC is employed, taking into account its high accuracy in computing local deformations and the computational efficiency of the method.

CHAPTER 2

Compaction of mixtures of rigid and soft particles

This chapter is based on the following published papers:

M. Cárdenas-Barrantes, D. Cantor, J. Barés, M. Renouf, and E. Azéma, Physical Review E 102, 032904 (2020). [156]

D. Cantor, M. Cárdenas-Barrantes, I. Preechawuttipong, M. Renouf, and E. Azéma, Physical Review Letters 124, 208003 (2020). [157]

This chapter analyzes the isotropic compaction of mixtures composed of rigid and deformable particles by the non-smooth contact dynamics approach (NSCD). The deformable bodies are simulated using a hyper-elastic neo-Hookean constitutive law using classical finite elements. We characterize the evolution of the packing fraction, the elastic modulus, the strain energy density, and some microstructural parameters, such as the connectivity, the local packing fraction, and the contact forces, as a function of the applied stresses when varying the coefficient of friction. We develop a micromechanical-based model to describe the compaction behavior as a function of the applied pressure, the Young modulus of the deformable particles, and the mixture ratio. This model lays on the characterization of a single deformable particle under compression together with a power-law relation between the connectivity and packing fraction.

2.1 Numerical framework

The simulations are carried out by means of the Non-Smooth Contact Dynamics (NSCD) method initially developed by Moreau, and Jean [66, 129]. The NSCD is the extension of the Contact Dynamic (CD) method [129, 158] to deformable bodies through a Finite

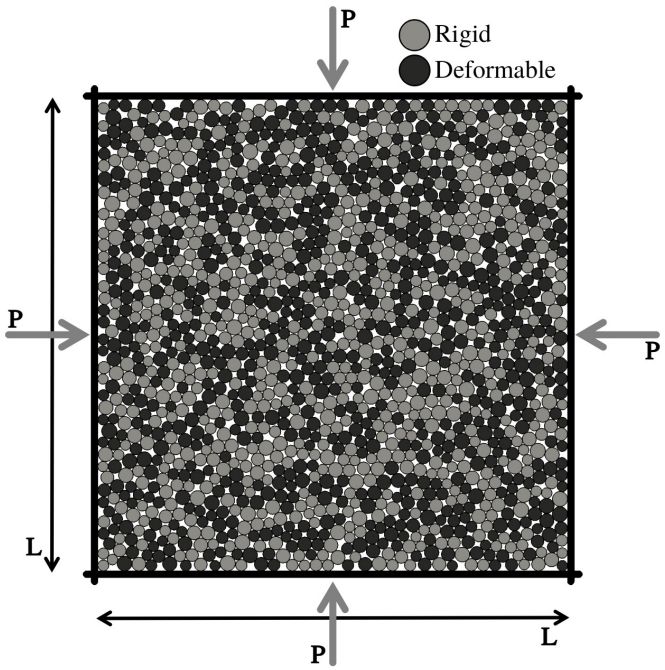

FIGURE 2.1. Scheme of the compression test for $\kappa = 0.50$. A collection of deformable and rigid particles are prescribed inside an initially squared 2D frame and compressed in a quasistatic manner with an imposed pressure, P. L is the size of the square box.

Elements approach (FEM). We used an implementation of the NSCD on the free, open-source simulation platform LMGC90 [159].

All samples are prepared according to the same protocol. First, $N_p = 1500$ rigid disks are randomly placed into a square box of initial length L_0 by simple geometrical rules in order to build a dense system [160]. A weak size polydispersity is considered by varying the diameter d of the disks in the range of $[0.8\langle d\rangle, 1.2\langle d\rangle]$ with a uniform distribution of the particle volume (area in 2D) fractions and $\langle d\rangle$ the mean diameter.

Second, a volume κV_p of rigid disks is homogeneously replaced by deformable disks meshed with 92 triangular similar-size elements, with κ the mixture ratio varying from 0.2 (packing composed of 20% of deformable particles) to 1 (packing of only deformable particles). All deformable particles are assumed to have the same isotropic neo-Hookean incompressible constitutive law [161]. We use a constant Poisson's ratio equals 0.495 and a Young modulus, E, varying as a function of the particle rigidity($E \to \infty$ for the rigid particles). Plane-strain conditions are also assumed.

Finally, the packings are isotropically compressed by gradually and quasistatically, applying the stress P on the boundaries, as shown in Fig. 2.1. A set of loading steps are

undertaken to target stable values of applied pressure and packing fraction. For a given pressure P, a stable state is reached once the variations of the packing fraction remained below 0.01%. The friction with the walls and the gravity are set to 0 to avoid force gradients in the sample.

The relevant dimensionless control parameters for disks under pressure P are the reduced pressure P/E [162,163] and the inertia parameter I [59] to assess how dynamic the tests are. I is defined as $\dot{\gamma}\langle d\rangle\sqrt{\rho/P}$, where $\dot{\gamma} = v/L_0$ with v the velocity of the walls, and ρ the particle density. In all our simulations, I remained below 10^{-4}, so the particle-to-particle interaction and the particles' bulk rapidly damped the kinetic energy, and elastic waves had little influence on the particle reorganization. Note that as $P/E \to 0$, we have $\phi \to \phi_0$ with ϕ_0 the packing fraction at the corresponding jammed state for the rigid assembly of particles.

We performed a large number of isotropic compression tests for a broad set of combinations of mixture ratios, coefficients of friction, and reduced pressures P/E. The mixture ratio κ was varied in the set $[0.2, 0.5, 0.8, 1.0]$ for two distinct values of coefficient of friction $\mu = 0.0$ and $\mu = 0.2$. For $\kappa = 1$, we also included simulations for an increasing coefficient of friction ($\mu = 0$ to 0.8). The reduced pressure P/E was varied from $\sim 10^{-5}$ to $P/E \sim 5 \cdot 10^{-1}$. The packings are shown in Fig. 2.2 for different values of κ and increasing stable values of P/E at $\mu = 0.2$.

2.2 Packing fraction and bulk properties

Figure 2.3 shows the evolution of ϕ as a function of P/E for rigid-deformable particle assemblies with $\kappa \in [0.2, 0.5, 0.8, 1]$ and $\mu \in \{0, 0.2\}$ (a), together with simulations fixing $\kappa = 1$ and varying $\mu \in [0, 0.2, 0.4, 0.6, 0.8]$ (b).

For all cases, curves evolve with the same general trend regardless of κ and μ. Particularly, the packing fraction first increases with P/E from ϕ_0 and then tends asymptotically to a maximum packing fraction ϕ_{max}. Note that both ϕ_0 and ϕ_{max} slightly decline as the friction increases. It is explained by the reduction of the particle rearrangements due to friction, as discussed in previous studies [51, 80, 164].

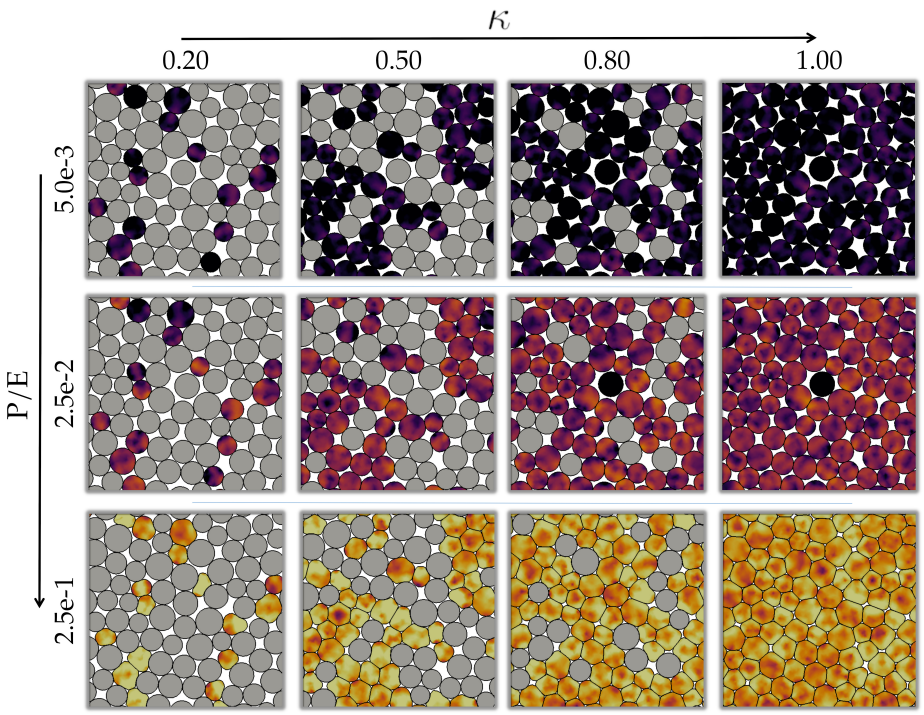

FIGURE 2.2. Close-up views for different mixture ratios κ and the reduced pressure P/E. Here, friction is fixed to 0.2. The rigid particles are shown in grey and the color intensity for the deformable particles is proportional to the volumetric deformation of the particles.

In assemblies of rigid-soft particles, ϕ_{max} decreases as κ goes towards 0, and tends to the random close packing when κ approaches 0. In the same figure, we plot some of the compaction models found in the literature fitting our numerical results for $\mu \in \{0, 0.2\}$ for all mixtures and $\mu \in \{0, 0.8\}$ at $\kappa = 1$. Further discussion upon these models was presented in **Section 1.3.2**.

It is also interesting to analyze the elastic properties of the assemblies depending on the values of the mixture ratio and friction coefficient. We define the bulk modulus as:

$$K(\phi) = \frac{dP}{d\phi} \cdot \frac{d\phi}{d\varepsilon_v}, \tag{2.1}$$

with $\varepsilon_v = -\ln(\phi_0/\phi)$ the macroscopic cumulative volumetric strain. Figure 2.4 shows the evolution of $K(\phi)$ as a function of ϕ for all values of κ and μ, measured in our simulations and computed using the derivative of the compaction equations used to fit the compaction evolution. We observe that K diverges as the packing fraction tends to ϕ_{max}. This comes from the fact that the assembly of grains starts to behave as a non-deformable solid. Note that, regardless of κ, the coefficient of friction has little influence on the macroscopic bulk

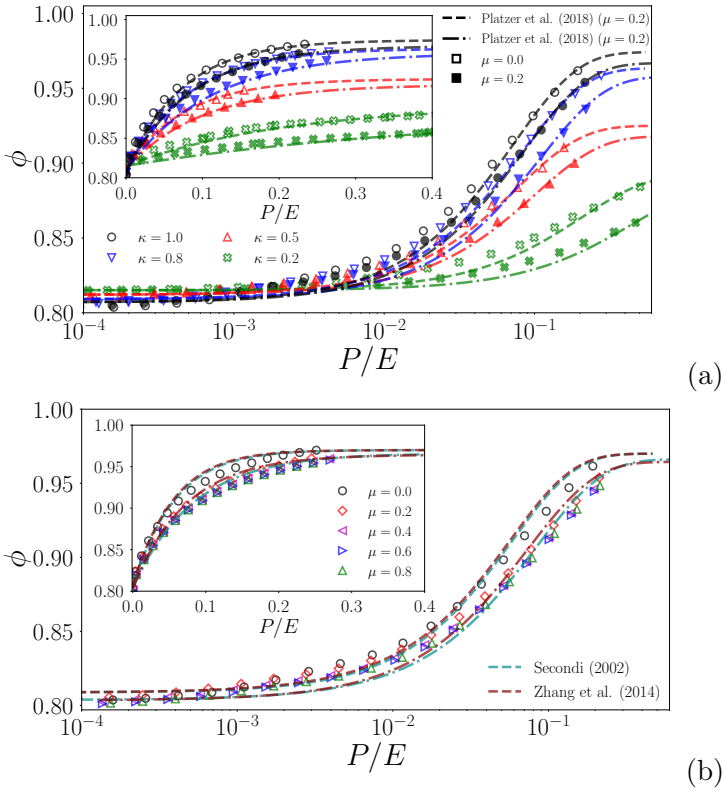

FIGURE 2.3. Evolution of the packing fraction ϕ as a function of P/E for (a) rigid-deformable particles assemblies with $\kappa \in [0.2, ..., 1]$ and $\mu \in \{0, 0.2\}$, and for (b) completely deformable particle assemblies (i.e., $\kappa = 1$) with $\mu \in \{0, 0.8\}$. Main panels are in lin-log scale while insets show curves in lin-lin scale. Numerical data (symbols) are shown with fits of Platzer et al.'s model [16] for rigid-deformable particles and Secondi's model [11], and Zhang's model [24] for the fully deformable systems (dashed lines).

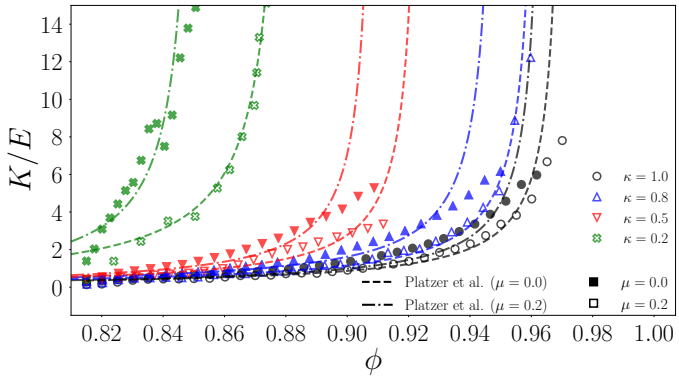

FIGURE 2.4. Evolution of the bulk modulus K normalized by the Young modulus E as a function of the packing fraction ϕ for simulations with all values of κ and $\mu = 0$ and 0.2. The dashed lines show the bulk modulus computed from the Platzer et al. compaction equation [16].

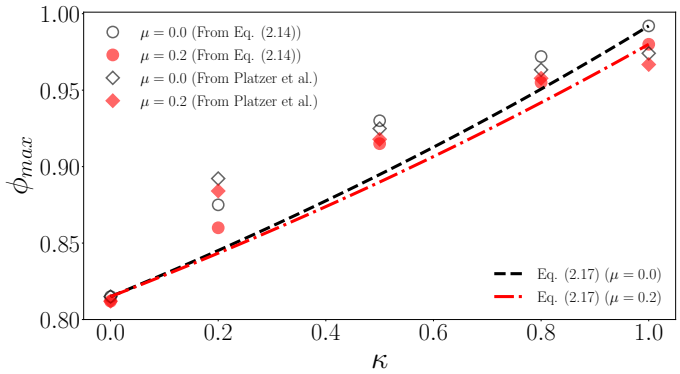

FIGURE 2.5. Values of ϕ_{max} fitted with Platzer et al.'s model (diamond symbols) and with Eq. (2.14) (circular symbol, see **Section 2.4**) on the compaction curves of rigid-deformable particle assemblies shown in Fig. 2.3(a), for different κ and $\mu \in \{0, 0.2\}$. The dashed lines show the prediction given by Eq. (2.17).

modulus for the small deformation domain. However, its effect slightly increases for large strain values.

2.3 Microstructural aspects

2.3.1 Particle connectivity

The coordination number Z, which allows quantifying the average number of neighbors per particle, is the first and the simplest statistical descriptor of the granular texture, i.e., the organization of the particles and their contacts in space. At the jammed state (i.e. for the packing fraction ϕ_0), the grain organization is characterized by a minimal value Z_0. Below

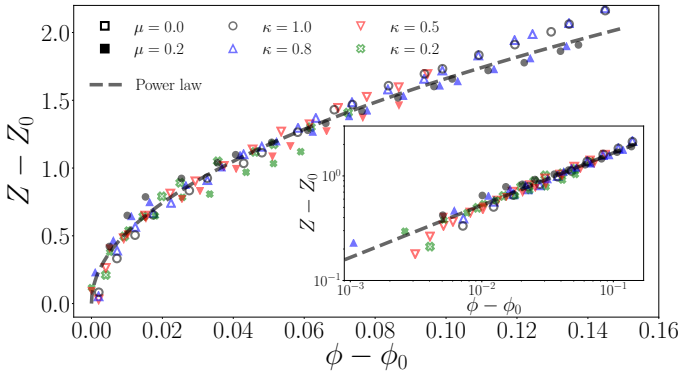

FIGURE 2.6. The reduced coordination number $Z - Z_0$ as a function of the reduced solid fraction $\phi - \phi_0$ for all values of κ and μ (a log-log representation is shown in the inset). The dashed black line is the power-law relation $Z - Z_0 = \xi(\phi - \phi_0)^\alpha$ with $\alpha = 0.5$ and $\xi = 5.1$.

such value, the collective motion of the particles is possible without necessarily implying particle deformation. As discussed in the **Chapter 1**, Z_0 depends on many parameters like shape, friction, and packing preparation [51, 165–167] to name a few. Basically, for circular particle assemblies, Z_0 declines as μ is increased, and tends to 4 as $\mu \to 0$, and to 3 for large friction values [168]. Furthermore, since Z_0 also depends on the packing preparation for frictional particles, distinct values of Z_0 are admissible.

Above the jammed state, it has been systematically reported in the literature that Z continues to increase following a power-law as:

$$Z - Z_0 = \xi(\phi - \phi_0)^\alpha, \tag{2.2}$$

with $\alpha \sim 0.5$ and $\xi = (Z_{max} - Z_0)/(\phi_{max} - \phi_0)^\alpha$ a structural parameter fully defined as $P/E \to \infty$, with both ϕ and Z reaching a maximum value ϕ_{max} and Z_{max}, respectively. This relation was observed both numerically and experimentally for many deformable particulate assemblies like foams, emulsions, and rubber-like particles [35, 79, 111, 164].

As shown in Fig. 2.6, we found the same proportionality in our simulations, with $\xi \sim 5.1$, independently of the mixture ratio and friction. Thus, our results extend the validity of such relation to binary mixtures.

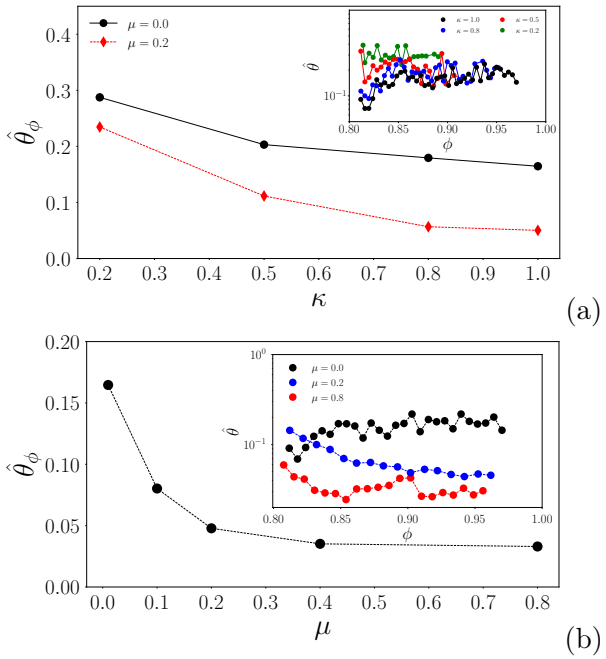

FIGURE 2.7. Non-affine rearrangement parameter $\hat{\theta}_\phi$ as a function of (a) the mixture ratio for two different values of friction ($\mu = 0.0$, 0.2), and (b) the friction coefficient for a packing of only soft particles ($\kappa = 1.0$). The inset in (a) shows the evolution of $\hat{\theta}$ as a function of the packing fraction ϕ for the different mixture ratios κ and coefficient of friction equal to 0. The inset in (b) shows the evolution of $\hat{\theta}$ as a function of ϕ for $\kappa = 1$ and different friction coefficients.

2.3.2 Particle rearrangements

A way to quantify the rearrangement of an assembly of particles is to measure the deviation of the movement of the particles from a reference direction, where the reference direction can be defined from the ideal case of a continuous, homogeneous, and deformable medium. The difference between the actual displacement and this referential displacement is the so-called non-affine motion. During an isotropic compression, each material point would move, on average, towards the geometric center of the system. We define the non-affine rearrangement parameter for each particle i, denoted by $\hat{\theta}_i$, as the absolute value of the angle, θ_i, between its velocity $\boldsymbol{v}_i$ and the vector defined from its center of mass to the geometric center of the packing, normalized by π ($\hat{\theta}_i = |\theta_i|/\pi$).

In the insets of Fig. 2.7 we present the evolution of the rearrangement parameter mean value $\langle\hat{\theta}_i\rangle_i$, as a function of packing fraction for the different mixture ratios and two coefficients of friction (a) and $\kappa = 1$ with different friction coefficients. First, For a low friction coefficient, $\langle\hat{\theta}_i\rangle_i$ slowly increases with ϕ, while it decreases for larger friction

coefficients. Second, $\langle\hat{\theta}_i\rangle_i$ increases faster as κ tends to 0. In other words, the particle rearrangements, although small, occur even after the jamming point and at each stage of the deformation.

To have a better idea of the reorganization of the particles along the compaction process, we compute $\hat{\theta}_\phi$, the asymptotic value of $\langle\hat{\theta}_i\rangle_i$ as the packing fraction goes to ϕ_{max}. Figure 2.7 shows $\hat{\theta}_\phi$ as a function of the (a) the mixture ratio κ for $\mu = 0.0$, 0.2, and (b) the friction coefficient for $\kappa = 1.0$. The rearrangement parameter is inversely proportional to both, the mixture coefficient and the friction. With a large proportion of rigid particles in the mixture, the few soft particles will store higher elastic potential energy as the system is compressed. In this case, the only way to release this extra energy is by moving the neighboring particles and find a more homogeneously stable state of minimum energy. This rearrangement occurs less frequently as the proportion of deformable particles increases since there is a progressively more homogeneous distribution of this elastic energy (see **Section 2.3.5)**. Particles rearrangement decreases as the friction coefficient increases since this frictional force is the one that opposes the sliding between particles. What is noteworthy is that low friction allows larger particle rearrangements while high friction tends to prevent it.

2.3.3 Shape parameter

During the compaction, the shape of the soft particles evolves from an initial circular form to a polygonal form, which depends on the mixture ratio and the friction coefficient. To characterize the change in shape of the particles, we use the circularity parameter $\hat{R}$ defined as usual by:

$$\hat{R} = \left\langle 4\pi \frac{V_i}{a_i^2} \right\rangle_i , \tag{2.3}$$

with a_i the particle perimeter and $\langle ...\rangle_i$ the average over the particles in the volume V.

In Figure 2.8 we show the evolution of $(\hat{R}-\hat{R}_0)$, with $\hat{R}_0$ the shape parameter computed at ϕ_0, as a function of the excess packing $(\phi-\phi_0)$ fraction for (a) different mixture ratios and two friction coefficients, and for (b) different values of friction coefficient for completely deformable packings. Interestingly, regardless of the friction and the proportion κ, $\hat{R}$

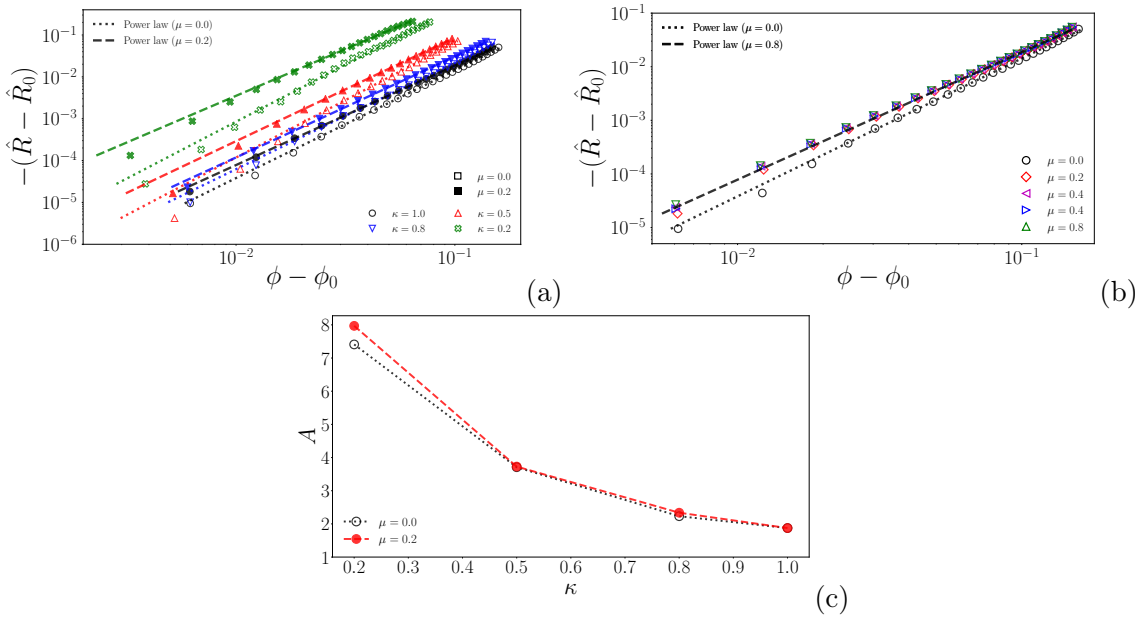

FIGURE 2.8. Evolution of $(\hat{R} - \hat{R}_0)$ as a function of $(\phi - \phi_0)$ for different values of (a) mixture ratio κ and (b) friction coefficient μ for $\kappa = 1.0$. The doted and dashed line are the power-law fittings for $\mu = 0.0$ and $\mu = 0.2$, respectively. (c) Power law's prefactor, A, as a function of the mixture ratio κ for coefficients of friction equal to 0.0 and 0.2.

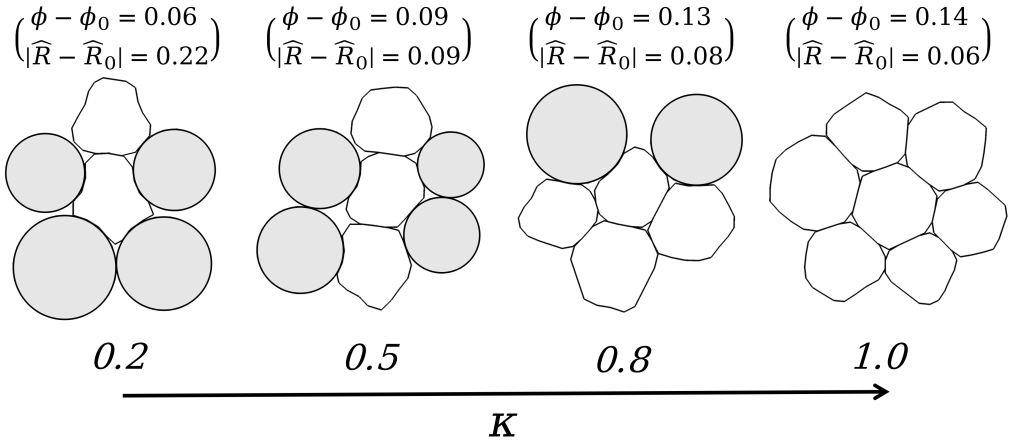

FIGURE 2.9. Group of particles extracted from the different mixture packings, showing the mean circularity value very close to the maximal packing fraction. The rigid particles are colored in gray.

increase following a power law as:

$$(\hat{R} - \hat{R}_0) = A(\phi - \phi_0)^{\beta}, \tag{2.4}$$

with β and A two fitting constants. We find that β is independent of κ but depends slightly on friction from $\beta \sim 2.6$ for $\mu = 0.0$ to $\beta \sim 2.4$ for $\mu > 0.2$. On the contrary, the scale parameter A does not change with the friction coefficient but is inversely proportional with the mixture ratio as it is shown in 2.8(c). This is explained by the fact that, at low κ-values the rigid particles strongly press the deformable ones, which quickly lose their circular shape and adopt non-regular shapes with low circularity values. As the ratio of deformable particles becomes high, the distribution of pressure in the system becomes more homogeneous (as it will be discussed below), as a result the particle shapes change more regularly and much more slowly. In Fig.2.9 we show the final shape of a random group of particles for different mixture ratios. Ideally, the final shape of the particles in a fully deformable system tends to be a hexagonal polygon since this form is the most efficient way to fill the (two-dimensional) space while minimizing the contact length between particles [17, 25, 79].

2.3.4 Specific contact length

The specific contact length per particle $ł_i$, defined as the ratio between the contact length and the perimeter of the particle, together with its average over the particles $Ł = \langle ł_i \rangle$, tell us the ratio of the particle boundaries in contact with another particle or with the boundaries. In Fig. 2.10 we show the evolution of the excess average specific contact length per particle $(Ł - Ł_0)$ as a function of the excess packing fraction $(\phi - \phi_0)$ for different mixture ratios (a) and friction coefficients (b). Remarkably, we see a linear tendency $(Ł - Ł_0) \approx m(\phi - \phi_0)$ with slope m varying from 1.6 to 2.5 as κ increases. In contrast, m seems to be independent of the friction coefficient (Fig.2.10(b)). This linear variation (with a similar slope) was observed before by Vu et al. [23] in an experimental study of hyperelastic cylinders under two-dimensional uniaxial compaction.

The linear tendency can be justified following some simple arguments. The average specific contact length Ł is proportional to the average length of each contact l times the average number of contacts Z: $Ł \sim lZ$. Assuming that contacts in our 2D circular particle

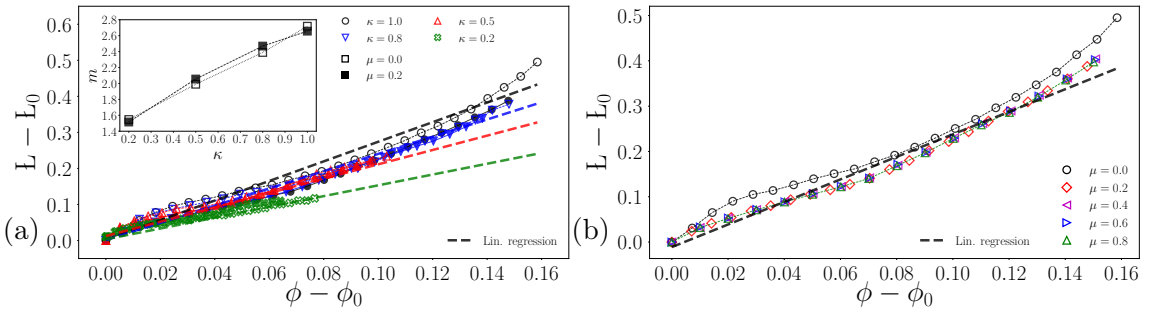

FIGURE 2.10. Evolution of the excess of the average contact length $Ł - Ł_0$ as a function of the excess packing fraction $\phi - \phi_0$ for different values of (a) mixture ratio κ and (b) friction coefficient μ for $\kappa = 1.0$. The dashed lines in both figures are linear fits of the evolution. The inset in (b) shows the slope m of the linear fits for the different mixture ratio κ. In (b) the linear fit has and slope ~ 2.6.

assemblies follow a similar Hertz law of 3D cylindrical particles assemblies, we get that the length at each contact is proportional to δ the deformation of that particle: $l \sim (d\delta)^{0.5}$, [59]. At the small deformation limit, for a typical square particle configuration, we know that the particle deformation is also proportional to the global strain, and thus to the excess of packing fraction, $\delta \sim \varepsilon_v \sim \phi - \phi_0$. Then $l \sim \varepsilon_v^{1/2} \sim (\phi - \phi_0)^{1/2}$. Moreover, as seen in **Section 2.3.1**, Z is proportional to $(\phi - \phi_0)^{1/2}$. With these last two results, we can then conclude that $Ł \sim (\phi - \phi_0)$. Such simple arguments are done on the small deformation domain, but we can see that the linear prediction is also conserved for larger strains.

2.3.5 Strain energy density

As it was mentioned in **Section 2.1**, the soft particles follow the isotropic neo-Hookean constitutive law. In this case, the bulk behavior of the particles can be described in terms of a strain energy density function, which can be written in general terms as [59]:

$$\Psi = \frac{\eta}{2}(I_1 - 3) - \eta \ln J + \frac{\lambda}{2} \ln^2 J, \tag{2.5}$$

where λ and η are the Lame's parameters, $I_1 = tr(F^T F)$, $J = Det(F)$, and F the deformation gradient tensor. For incompressible material, as it is our case, the Poisson ratio $\nu \approx 0.5$, so $J = 1$ and λ goes to infinity. Thus the strain energy density function is reduced to:

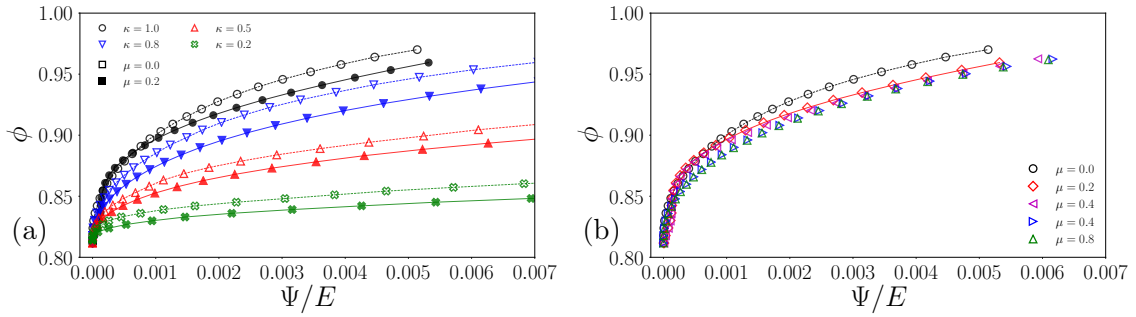

FIGURE 2.11. Packing fraction as a function of the mean strain energy density of the soft particles mormalize by the Young modulus for (a) different mixture ratios with $\mu = 0.0$, 0.2, and for (b) different friction coefficient with $\kappa = 1.0$.

$$\Psi = \frac{\eta}{2}(I_1 - 3) = \frac{E}{4(1+\nu)}(I_1 - 3). \tag{2.6}$$

We define Ψ as the mean value of the strain energy density over all the soft particles in the packing, such that Ψ is zero when the particles are not deformed, and it increases with the deformation. Figure 2.11 shows the evolution of the packing fraction ϕ as a function of Ψ/E for the mixture ratios in (a), and for different friction coefficient with $\kappa = 1.0$ in (b).

The evolution of the $\phi(\Psi)$, for all the mixtures and friction coefficients, is similar to the one with the applied pressure P (Fig. 2.3). At the initial stages of compaction, the strain energy grows very slowly since there are no large deformations of the particles (see **Section 2.3.3**). As the compaction continues, the particles achieve more significant deformations, causing the strain energy to diverge as it reaches the maximum packing fraction for each mixture ratio and friction coefficient.

2.3.6 Force distribution

The force chains in granular assemblies and the non-homogeneous spatial distribution of the contact forces are widely studied, numerically and experimentally. These studies are mainly performed on rigid particle of various sizes [52, 55, 63, 169], shapes [8, 52, 170] and contact interactions [171, 172]. However, it has seldom been studied for highly deformable particles or rigid/soft particle mixtures.

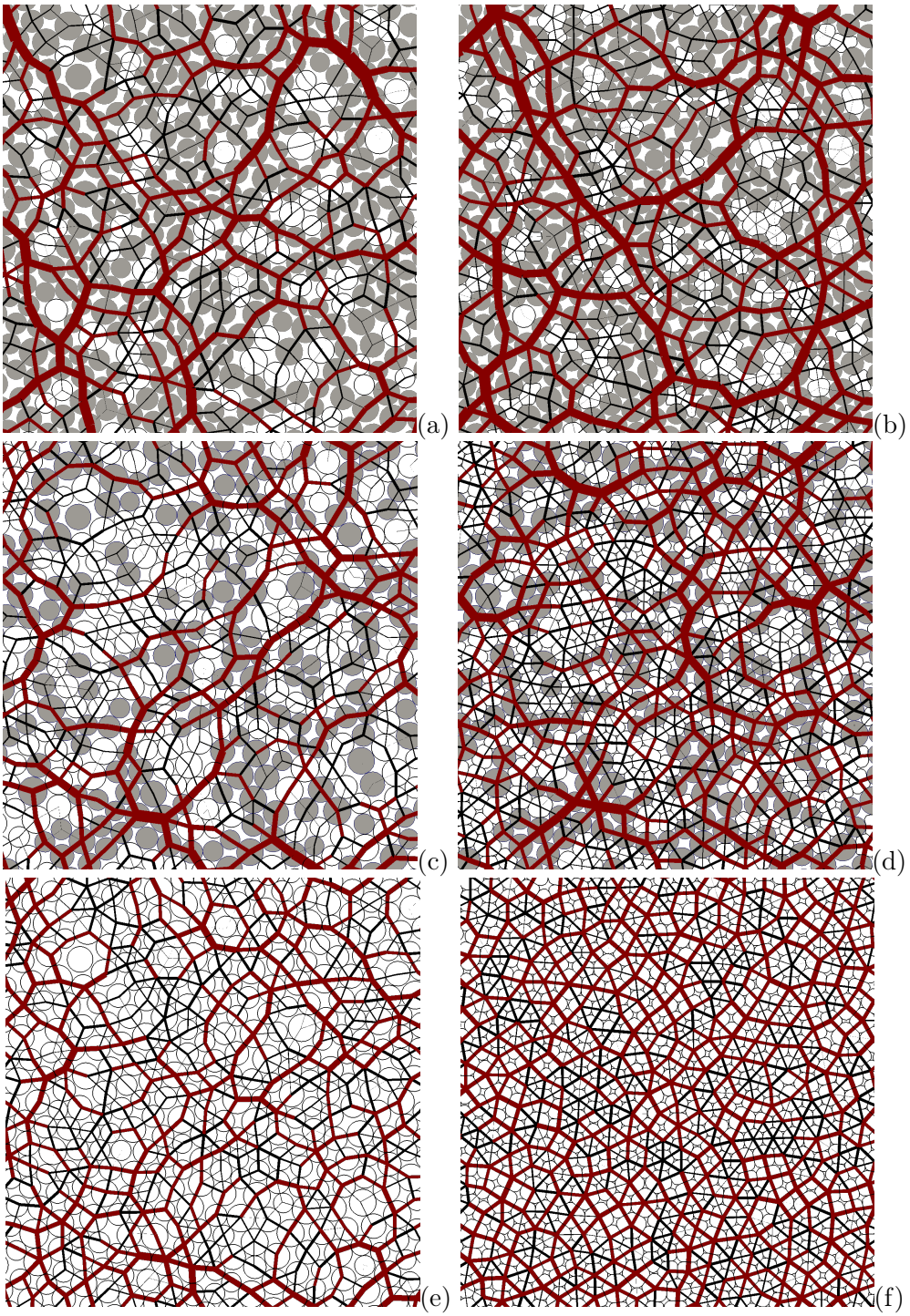

FIGURE 2.12. Close-up views of the force chains in frictionless assemblies of disks for $\kappa = 0.2$ (a,b), $\kappa = 0.5$ (c,d) and $\kappa = 0.1$ (e,f) at the jammed state (a,c,e) and for $\phi \sim \phi_{max}(\kappa)$ (b,d,f). The magnitude of each normal force is represented by the thickness of the segment joining the centers of the particles in contact. The strong forces ($f_n \geqslant \langle f_n \rangle$) and weak forces ($f_n < \langle f_n \rangle$) are plotted in red and black, respectively.The rigid particles are colored in gray

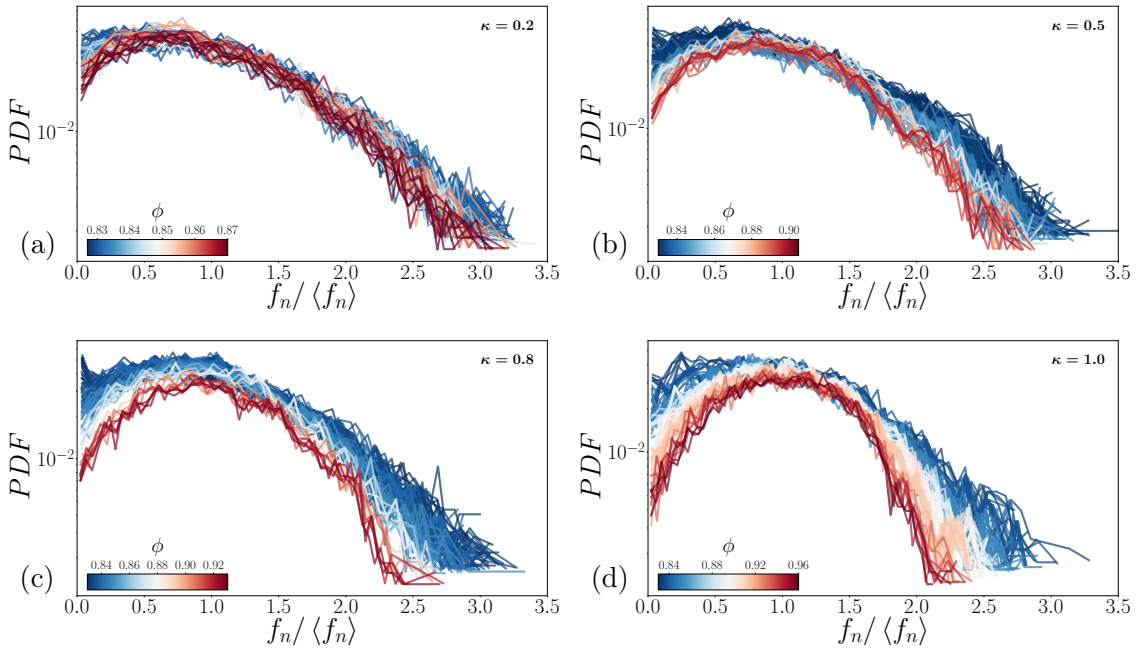

FIGURE 2.13. Probability distribution function of the normal contact force f_n, normalized by the mean value $\langle f_n \rangle$, for mixture ratios of (a) $\kappa = 0.2$, (b) $\kappa = 0.5$, (c) $\kappa = 0.8$ and (d) $\kappa = 1.0$.

Figure 2.12 shows the normal force chains of in assemblies with $\kappa = 0.2$, $\kappa = 0.5$ and $\kappa = 1$, at the jammed state (a,c,e) and for ϕ close to ϕ_{max} (d,b,f). Here, the total contact force between two particles is computed as the vector sum of the forces at the contact nodes along the common interface (a line in 2D). The force network density (i.e., the number of force chains) increases with ϕ because, as discussed before, the mean number of contacts per particle increases. In general, the force chains appear to be highly inhomogeneous close to the jammed state, where the stronger forces seems to be laid on the rigid particles. Close to ϕ_{max} the distribution of forces is more homogeneous in the case of $\kappa = 1$ while strong inhomogeneities persist for low values of κ with stronger forces mainly supported by the rigid particles.

The Probability Density Functions (PDFs) of the normal forces f_n normalized by the mean value $\langle f_n \rangle$ for different mixture ratios and increasing packing fraction are presented in Fig. 2.13. As it is commonly observed, the density of forces above the mean value, close to the jamming point, has an exponential decay, whereas the density of forces below the mean value follows a power law [62, 173]. As the packing fraction increases both, the number of weak forces and the value of stronger forces decrease. These tendencies are magnified as κ tends to 1.. Furthermore, for higher pressures and larger κ, it is observed

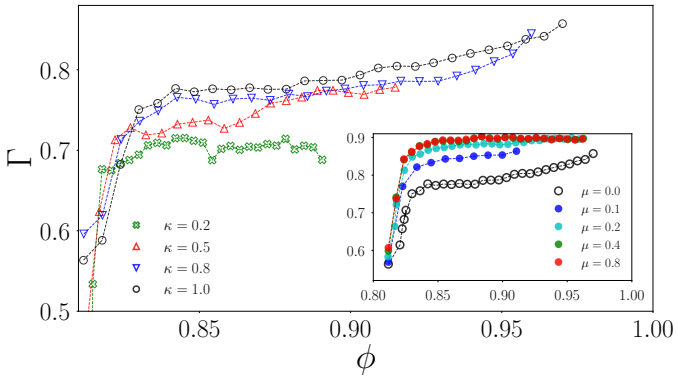

FIGURE 2.14. Participation number Γ as a function of ϕ for $\mu = 0$ and different values of κ, and for different values of μ for $\kappa = 1$ (inset)

that the assemblies reach more homogeneous distributions, with shapes close to Gaussian distributions centered around the mean value. Finally, for lower values of κ, the normal force distributions preserve a clear power law for weak forces and exponential tails for strong forces.

The degree of homogeneity of the normal force network can be quantified by the, so-called, participation number Γ defined as [18]

$$\Gamma = \left(N_c \sum_{i=1}^{N_c} q_i \right)^{-1}, \tag{2.7}$$

where N_c is the total number of contacts in the system and $q_i = f_i / \sum_{j=1}^{N_c} f_j$, with f_i the magnitude of the normal force at the contact i. For a homogeneous force distribution, Γ is equal to 1, while the limit in which the forces are entirely heterogeneous corresponds to $\Gamma \simeq 0$. The evolution of Γ for the frictionless case and for different values of κ as a function of ϕ is shown in Fig. 2.14. $\Gamma(\phi)$) for $\kappa = 1$ with different values of friction μ are presented in the inset. In general, Γ has a rapid increase with ϕ just passing the jamming point, and then a slow increase as the packing fraction approaches the maximal value. These variations of Γ verifies that the force chain network becomes more dense and homogeneous as the packing fraction is increased far beyond the jamming point. In particular, the homogeneity of force chains is enhanced when the proportion of soft grains tends to 1. It is also worth noting that Γ increases with friction, suggesting that the friction contributes to a faster homogenization of the force network.

2.4 Micromechanical approach of the compaction: Scaling from the behavior of a single grain

A proper model that pictures the compaction of soft packings should stand on a clear physical analysis of the micromechanics at the particle scale. In this direction, let us rewrite the granular stress tensor (as introduced in the Chap. 1), from the scale of the contacts as [59]:

$$\sigma_{ij} = \frac{1}{V} \sum_{c \in V} f_i^c \ell_j^c = n_c \langle f_i^c \ell_j^c \rangle_c, \tag{2.8}$$

where f_i^c is the i^{th} component of the contact force acting on a contact c and ℓ_j^c is the j^{th} component of the branch vector (i.e., the vector joining the centers of particles interacting at contacts c). The sum runs over all contacts inside the volume V, and $\langle ... \rangle_c$ is the average over contacts. The density of contact n_c, on the right hand side of Eq. (2.8), is given by $n_c = N_c/V$ with N_c the total number of contacts in the volume V. From the stress tensor, we extract the mean stress $P_\sigma = (\sigma_1 + \sigma_2)/2$, with σ_1 and σ_2 the principal stress values, and $P = P_\sigma$.

Considering a small particle size dispersion around the diameter $\langle d \rangle$, the contact density can be rewritten as $n_c = 2\phi Z/\pi \langle d \rangle^2$, with $Z = 2N_c/N_p$ the coordination number. These definitions permit to rewrite the stress tensor as $\sigma_{ij} = (2\phi Z/\pi \langle d \rangle^2) \langle f_i^c \ell_j^c \rangle_c$. Finally, taking into account the definition of P via the principal stresses of σ_{ij}, we can deduce a microstructural equation of the compression stress as [117, 163, 174]:

$$P = \frac{\phi Z}{\pi} \sigma_\ell, \tag{2.9}$$

with $\sigma_\ell = \langle f^c \cdot \ell^c \rangle_c / \langle d \rangle^2$, a measure of the inter-particle stresses, with $\cdot$ the scalar product. This way of writing P as a function of Z, ϕ, and σ_ℓ is, in fact, very common and has been successfully applied in different contexts. For example, to relate the bulk properties of an assembly to the elastic contact properties [167, 174, 175], or as well the macroscopic cohesive strength to the cohesion behavior between the interface of particles in contact [27, 176]. Equation 2.9 reveals the mutual relation between P and ϕ through the granular microstructure described in terms of both particle connectivity (Z) and inter-particle stress (σ_ℓ).

2.4.1 Voigt approximation

Elastic properties of a granular assembly can be estimated in the small-strain domain through the Effective Medium Theory EMT [74, 167, 174, 177], in which the particles are replaced by a network of bonds of length ℓ^c. From there, and by analogy with the macroscopic volumetric strain ε_v, we can define a local volumetric strain as $\varepsilon_{v,\ell} = \langle \ln(\ell^c/d) \rangle$. Our numerical simulations also show that $\varepsilon_v = 4\varepsilon_{v,\ell}$, for all values of κ and μ. Then, for small and elastic deformations we get that $\sigma_\ell \sim E\varepsilon_{v,\ell}$.

Finally, the above expressions with Eqs. 2.2, 2.9, and 2.1 together with a first-order Taylor expansion of ε_v, give an estimation of the bulk modulus as:

$$\frac{K_1}{E} = \frac{Z\phi}{4\pi}\left(\frac{5}{2} - \frac{\phi_0}{\phi}\right) - \frac{Z_0\phi}{8\pi}. \tag{2.10}$$

Note that, in the limit of $\phi \to \phi_0$, Eq. (2.10) predicts that $K_1 \to Z\phi E/(2\pi)$ which is in agreement with other equations obtained within the small-strain framework for assemblies of rigid particles with elastic interactions [74, 167, 177, 178].

The prediction given by Eq. (2.10) is shown in Fig. 2.15 for all values of κ at $\mu = 0$. We see that the measurement of the bulk modulus within an equivalent medium approach gives matching results in the small-strain domain for all values of κ. However, here the prediction given by Eq. (2.10) is still acceptable over the range of $\phi \in [\phi_0, \phi^+]$ where ϕ^+ increases from $\simeq 0.83$ for $\kappa = 0.2$ to $\simeq 0.9$ for $\kappa = 1.0$, until an increasing mismatch is observed as the packing fraction tends to ϕ_{max}. Indeed, in the limit $\phi \to \phi_{max}$, the assembly of grains starts to behave as a non-deformable solid, and thus, the corresponding bulk modulus diverges. These observations suggest that we should reconsider the definition of local the strain only by mean of the contact deformations $\sigma_\ell \sim E\varepsilon_{v,\ell}$.

2.4.2 Scaling with a single-particle configuration

Let us consider the case of an elementary system composed of a single particle isotropically compressed between four rigid walls (i.e., submitted to the same boundary conditions as the multi-particle assembly, see the upper part of Fig. 2.16). In Fig. 2.16, we present the evolution of the packing fraction ϕ_p as a function of the applied pressure P_p in the case of a single-particle. Note that the number of finite elements N_e has a minor influence on

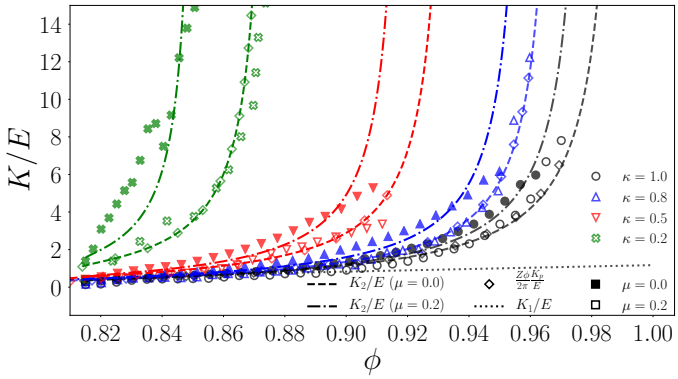

FIGURE 2.15. Bulk modulus K normalized by E along with the micro-mechanical relation proposed on Eq. (2.12) (diamont symbols) for all values of κ and $\mu = 0$. The prediction given by Eq. (2.15) is shown in dashed line for $\mu = 0$ and $\mu = 0.2$ and the one given by Eq. (2.10) is displayed in dotted line.

the results. We also observe that the single-particle compression curve $\phi_p - P_p$ is roughly similar to the multi-particle compaction curve $\phi - P$ (Fig. 2.3). This supports the idea of a strong relation between the single-particle and multi-particle systems.

Indeed, as shown in Fig. 2.16 (gray dashed line), the compaction behavior of such an elementary system is well described with the following logarithmic function:

$$P_p/E = -b \ln \left(\frac{\phi_{p,\max} - \phi_p}{\phi_{p,\max} - \phi_{p,0}} \right), \tag{2.11}$$

with $\phi_{p,\max}$ the maximum packing fraction obtained, $\phi_{p,0} = \pi/4$ the solid fraction as $P_p/E \to 0$, and b a constant of proportionality found to be $\simeq 0.14$. Equation 2.11 is derived from the analogy to the collapse of a cavity within an elastic medium under isotropic compression, the extended hollow sphere model [90, 179]. Although this relation is well adapted to the single-particle test, similar functional forms have been used for multi-particle systems, as discussed in **Section 1.3.2**. Then, the bulk modulus of the single particle assembly is given by: $K_p(\phi_p) = (dP_p/d\phi_p) \cdot (d\phi_p/d\varepsilon_{v,p})$, with $\varepsilon_{v,p} = -\ln(\phi_{p,0}/\phi_p)$.

Now, comparing these two systems at equivalent packing fraction (i.e., for $\phi_p \equiv \phi$), we obtain that, for all values of κ and μ, the macroscopic bulk modulus K of the assembly scales with K_p as (Fig. 2.15):

$$K \equiv \frac{Z\phi}{2\pi} K_p + \mathcal{O}, \tag{2.12}$$

with $\mathcal{O}$ negligible high order terms on ϕ. Equation 2.12 allows us to reinterpret the micromechanical origin of the bulk modulus of an assembly of rigid-deformable particles in

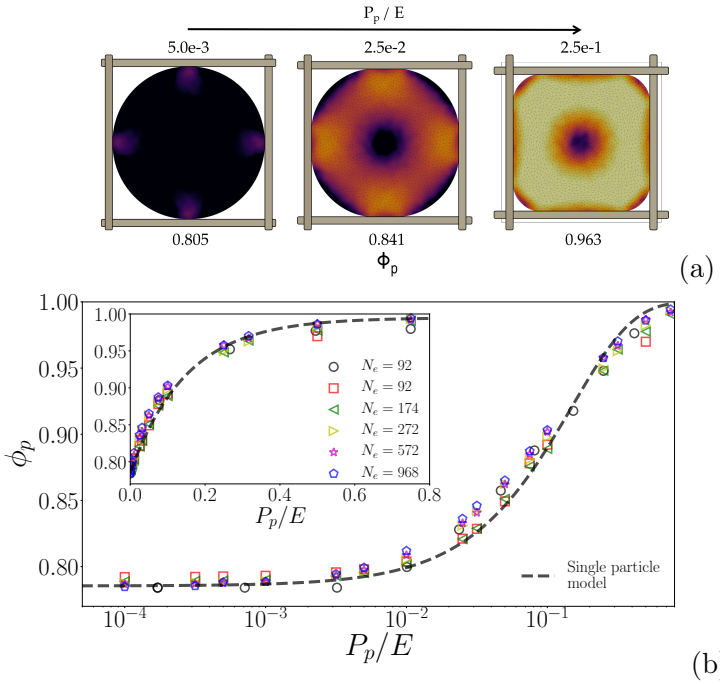

FIGURE 2.16. Compaction of a single particle inside a square box. (a) Snapshots of the simulation for $N_e = 968$ (number of finite elements) at different compression level. The color intensity of the particle is proportional to its volumetric deformation. (b) Packing fraction as a function of the pressure applied on the box. Red squares (P_p is fixed and E varies) and black circles (E is fixed and P_p varies) correspond with tests on a particle with $N_e = 92$. For the other mesh resolutions, E was fixed and P_p varied.

terms of particle connectivity, packing fraction, and the bulk property of an elementary system. We can also reinterpret Eq. (2.9) as:

$$P \simeq \frac{Z\phi}{2\pi} P_p, \tag{2.13}$$

and we deduce that $\mathcal{O}$ in Eq. (2.12) is related to the derivatives $(dZ\phi P_p + Zd\phi P_p)$. Equations 2.12 and 2.13 reveal that the elastic and compaction properties of a binary mixture are scalable from the behavior of a single-particle. This finding is aligned with the general idea of describing the macroscopical properties of a granular packing from a single representative element [180, 181].

2.4.3 A compaction and bulk equation

Finally, using the $Z - \phi$ relation (i.e., Eq. (2.2)) into Eq. (2.13), together with Eq. (2.11) at equivalent packing fraction, and noting that, for a given friction the maximum packing fraction depends on the mixture ratio (Fig. 2.5), we get the following compaction equation:

$$\frac{P(\phi,\kappa)}{E} \simeq -\frac{b\phi}{2\pi}\left\{Z_0 + \xi(\phi-\phi_0)^{\alpha}\right\} \ln\left(\frac{\phi_{\max}(\kappa)-\phi}{\phi_{\max}(\kappa)-\phi_0}\right). \tag{2.14}$$

In contrast to previous models, the only unknown parameter in Eq. (2.14) is the maximum packing fraction $\phi_{max}(\kappa)$ since all other constants are determined from either the initial state (Z_0 and ϕ_0, encoding the packing preparation), the behavior of a single representative particle (b) or the mapping between the packing fraction and coordination evolution (ξ and α).

Figure 2.17 presents our numerical data (same as in Fig. 2.3) together with the compaction equation given by Eq. (2.14). The predictions given by Eq. (2.14) are good for any pressure capturing the asymptotes for vanishing and extremely high pressures, the effect of mixture ratio, and the effect of friction. Our compaction equation also allows us to predict the asymptote for the maximal packing fraction ϕ_{max}, both as a function of κ and μ. The best ϕ_{max}-values used in Eq. (2.14) are shown in Fig. 2.5 (circular symbols) as a function of κ for $\mu \in \{0, 0.2\}$.

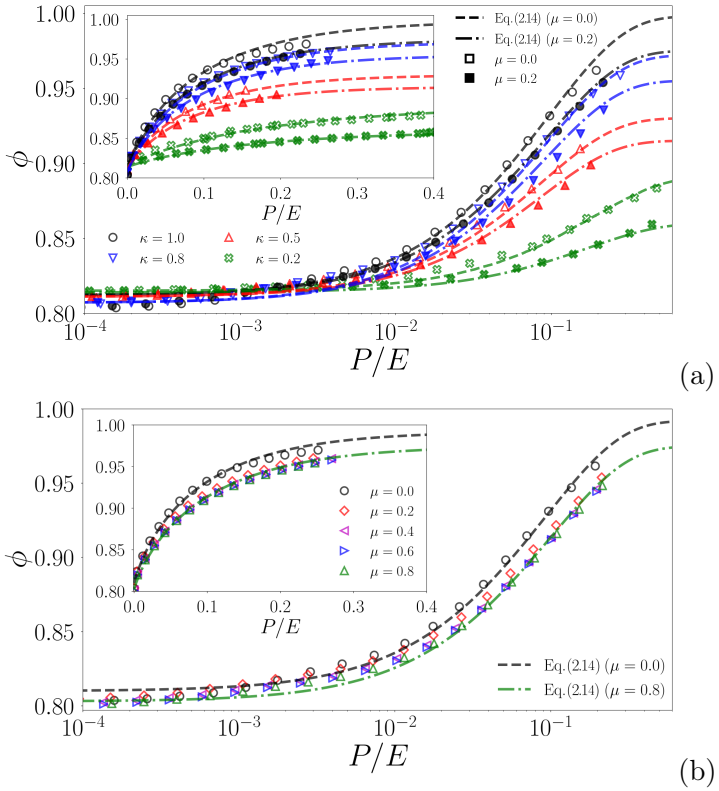

FIGURE 2.17. Compaction curves ϕ as a function of P/E for (a) rigid-deformable particles assemblies with $\kappa \in [0.2, ..., 1]$ and $\mu \in \{0, 0.2\}$, and for (b) completely deformable particle assemblies (i.e., $\kappa = 1$) with $\mu \in \{0, ...0.8\}$. In both, the curves are presented in lin-log scale in the main panel and in lin-lin scale in the inset. The predictions given by our micro-mechanical equation (Eq. (2.14)) are shown in dashed lines.

Going one step further and derivating Eq. (2.14) we get a second expression for the bulk modulus evolution as:

$$\frac{K_2(\phi,\kappa)}{E} \simeq \frac{b\phi^2}{2\pi(\phi_{\max}(\kappa)-\phi)}\{Z_0+\xi(\phi-\phi_0)^\alpha\}. \tag{2.15}$$

Figure 2.15 shows the above relation giving the evolution of K throughout the deformation for all values of κ and $\mu \in \{0, 0.2\}$.

Finally, the increase of ϕ_{max} with κ shown in Fig. 2.5, can be described by comparing our system with the following simpler one. Let us imagine an assembly where particles are separated in two phases, a rigid and a deformable one, as shown in Fig. 2.18. The total volume V of the box is then given by $V = V_{or} + V_{od}$, where V_{or} and V_{od} are the corresponding volumes of the sub-boxes containing the rigid and deformable particles respectively. Considering that the total volume of deformable particles is $V_d = \kappa V_p$ and that the one of rigid particles is $V_r = (1-\kappa)V_p$, the packing fraction of the mixture is then given by:

$$\phi(\kappa) = \frac{\phi_0\ \phi(1)}{\phi(1) + (\phi_0 - \phi(1))\kappa}, \tag{2.16}$$

with $\phi_0 = V_r/V_{or} = \phi(\kappa = 0)$, and $\phi(1) = V_d/V_{od} = \phi(\kappa = 1)$, being the packing fractions of only rigid and deformable particle assemblies, respectively. Therefore, we can write the maximal packing fraction as:

$$\phi_{max}(\kappa) = \frac{\phi_0\ \phi_{1,max}}{\phi_{1,max} + (\phi_0 - \phi_{1,max})\kappa}, \tag{2.17}$$

with $\phi_{1,max}$ the maximum packing fraction for $\kappa = 1$. As shown in Fig. 2.5 with dashed lines, Eq. (2.16) gives acceptable predictions for $\mu = 0$ and $\mu = 0.2$. So, by replacing Eq. (2.17) into Eq. (2.14) and Eq. (2.15), we obtain an equation based on the sole knowledge of the maximum compaction value reachable in assemblies composed of only deformable particles.

2.5 Conclusions

In this chapter, we analyze the compression behavior of two-dimensional granular assemblies composed of mixtures of rigid and incompressible deformable particles. The pro-

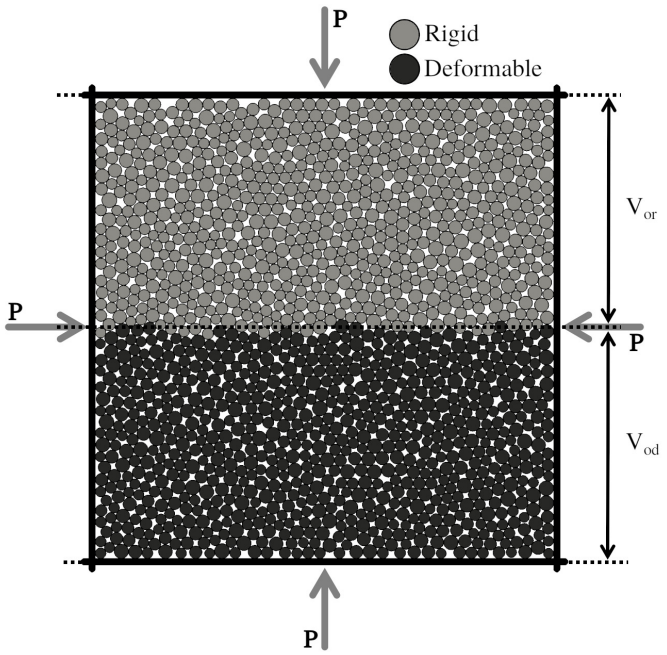

FIGURE 2.18. Sketch of the simplified geometrical approach to estimate the packing fraction of the assembly as a function of κ. Particles are separated in two distinct phases, a rigid and a deformable one.

portion of deformable particles was varied from 0.2 (i.e., assembly composed of 20% of deformable grains) to 1 (i.e., assembly composed of only deformable grains) for different friction values. Starting from the jammed state characterized by a given packing fraction ϕ_0, granular systems were isotropically compressed by gradually applying stress on the boundaries.

At the macroscopic scale, we found that the packing fraction increases from ϕ_0 and asymptotically tends to a maximum value ϕ_{max}. The decrease of the proportion of deformable particles and the increase of the friction coefficient lower the value of ϕ_{max}. Although most existing models provide acceptable predictions, the maximum packing fraction reachable must be estimated or calibrated along with other parameters and cannot be easily deduced.

At the microscopic scale, we first enlightened the existence of power-law tendencies for the excess coordination number and the excess shape parameter as a function of the excess coordination number. In the case of the coordination number, the exponents and the scale parameter of the power-law relation are conserved for different mixture ratios and friction coefficients. In the case of the shape parameter, the exponent slightly varies

with the friction coefficient but stays constant when we vary the mixture ratio. A linear relationship between the excess relative contact length and the excess packing fraction is also observed and its slope depends on the mixture ratio. And for all values of the mixture ratio and friction, an increasingly homogeneous distribution of contact forces and particle stress appear when the applied pressure increases.

A major outcome of this work is the introduction of a compaction model for binary mixtures of rigid and deformable particles, free of any *ad hoc* parameters, and standing on well-defined quantities related to (*i*) the particle connectivity, (*ii*) the bulk behavior of a single representative particle and (*iii*) the proportion of rigid-deformable particles. Our model, derived from the micro-mechanical expression of the granular stress tensor, results in satisfactory predictions of the compaction evolution for all values of the mixture ratio parameter at any friction. In addition to this, the maximum packing fraction of the assembly is deduced as the only fitting parameter at the macroscopic scale. A bulk equation is also deduced from the compaction model, resulting in a good agreement with our numerical data for all values of the mixture ratio parameter and friction.

Besides the compaction equation for the assembly of rigid-deformable particles, we would like to highlights the methodology used to develop our approach. This approach allows us to unify in a coherent framework the compaction behavior of assemblies of deformable and rigid-deformable grains beyond the jamming point. The above framework may now be used and extended to analyze much more complex deformable granular assemblies by considering a wide range of material properties, such as plastic particles, non-spherical particles, and polydisperse particles. Other loading configurations, like the oedometric compression test, could be investigated in this framework as well.

In this chapter, we have proposed a compaction model based on scaling the bulk properties of one single particle under similar loading conditions. The next chapter presents a slightly different approach for the same compaction model. This will allow us to deal with different regular geometries different from disks and overpass the need for one single particle scaling.

CHAPTER 3

Compaction of soft pentagon assemblies

This chapter is based on the following published paper:

M. Cárdenas-Barrantes, D. Cantor, J. Barés, M. Renouf, and E. Azéma, Physical Review E 103, 062902 (2021). [182]

Real-world processes usually involve particles that are not spherical, with particles that can differ significantly in their geometrical and mechanical properties.These differences in shape at the local particle scale are reflected in different ways at the global scale of the granular assembly. Thus, for example, a nonlinear variation of the packing fraction at the jamming point is seen as the particle shape moves away from the spherical shape. This chapter analyzes the isotropic compaction of assemblies composed of soft pentagons interacting through classical Coulomb friction. Assemblies of circular particles under similar loading conditions are also simulated to study the effects of the initial shape on the macro and microstructure. In addition, contact friction is also systematically studied. We characterize the evolution of the packing fraction, the elastic modulus, and the microstructure (particle rearrangement, connectivity, contact force, and particle stress distributions) as a function of the applied stress. The micromechanical compaction model presented in the previous chapter is also revised and extended to non-circular regular particles.

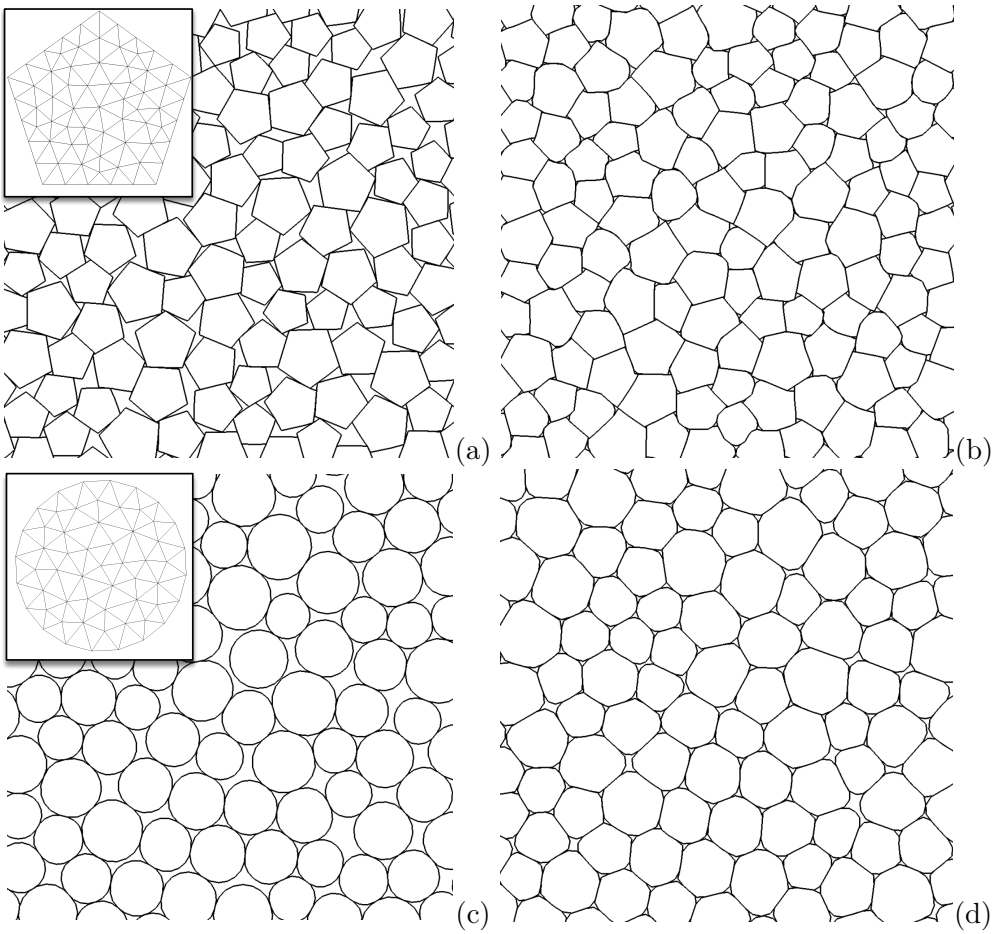

FIGURE 3.1. Close-up views of the assembly of pentagons (a,b) and disks (c,d) at $\mu = 0$ and for $P/E = 0.025$ (a,c) and $P/E = 0.3$ (b,d). The insets of (a) and (c) show the finite element mesh used for both pentagons and disks, respectively.

3.1 Numerical Procedure

In the NSCD's frame [129, 158], we simulate packings of soft and incompressible particles with two different shapes, regular pentagons and disks, under external isotropic compression.

First, $Np = 500$ rigid particles are randomly placed into a two-dimensional square box bounded by rigid walls. To avoid crystallization, a small size polydispersity around the mean diameter of the particles $\langle d \rangle$ is introduced ($d \in [0.8 \langle d \rangle , 1.2 \langle d \rangle]$). For a pentagon, d is the diameter of its circumcircle. The packing is then isotropically compressed under a small stress σ_0 up to its jamming point. We consider that the jamming point is reached once the variations of the packing fraction ϕ remain below 0.05%, with ϕ defined as $\phi = \sum_{i \in V} V_i / V$, where V_i is the volume of the particle i and V the total volume of the packing. In our

simulations, the jamming point corresponds to a packing a packing fraction $\phi_0 \approx 0.808$ and ≈ 0.817, for disks and pentagons, respectively. At this point, the box size is $L_0 \times L_0$. Second, the particles are meshed with 92 triangular elements (see inset in Fig. 3.1). We use a constant Poisson's ratio equals to 0.495 and a Young modulus E such that $\sigma_0/E << 1$. With these conditions, the strain energy of one particle is given by $\Psi = (1/4)E(I_1 - 3))/(1 + \nu)$, where $I_1 = tr(F^T F)$ and F the deformation gradient tensor [79].

Finally, the packings are isotropically compressed by imposing the same constant velocity v on the box's boundaries. The velocity v is carefully chosen to be sure that the system is always in the quasi-static regime defined by the inertial number $I = \dot{\gamma}\langle d\rangle\sqrt{\rho/P}$, with $\dot{\gamma} = v/L_0$, ρ the particle density and P the confining stress [59,136]. The quasi-static limit is ensured for $I << 1$. Thus, in all the simulations, v is computed from the inertia parameter replacing I by $I_0 = 10^{-4}$ and P by σ_0. In this way, the inertia parameters remain below 10^{-4} during the compaction process. We performed a large number of tests for different coefficients of friction between particles, $\mu \in [0.0, 0.1, 0.2, 0.4, 0.8]$, while we kept the coefficient of friction with the walls equal to zero. The gravity is set to zero. Figure 3.1 shows frictionless assemblies of pentagons and disks at the jammed state and beyond.

3.2 Packing fraction and bulk properties

Under isotropic compression, the confining stress acting on the assembly is given by $P = F/L$, where F is the computed force on the walls and L its length. For a granular assembly, we can also compute the confining stress from the granular stress tensor σ (See Eq. (5.2) in **Chapter 1**).

Figure 3.2 shows the evolution of ϕ as a function of the reduced pressure P/E for assemblies of pentagons and disks (insets). Regardless of the value of friction, the packing fraction follows the same general trends. From the jammed state, the packing fraction increases rapidly for small values of P/E and reaches an asymptote at ϕ_{max}. We observe a progressive separation of the compaction curves as the friction increases, which results in a slight decrease in the value of ϕ_{max}. This offset between the curves is more evident for pentagons than for disks. Such difference is explained by the fact that the friction and the

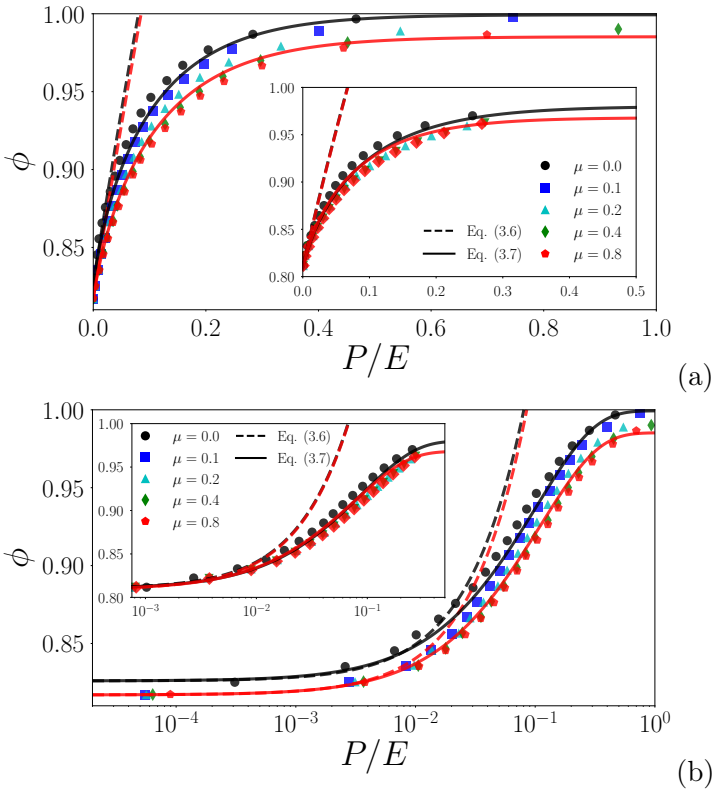

FIGURE 3.2. Packing fraction ϕ as a function of the reduced pression P/E for assemblies of soft pentagons, and different values of friction, in (a) lin-lin scale and (b) log-lin scale. The insets show the same data for assemblies composed of soft disks. The dashed lines are the elastic approximations (Eq. (3.6)) and the continuous lines are the predictions given by Eq. (3.7) for $\mu = 0$ (black) and $\mu = 0.8$ (red).

particle shape restrict the mobility of the particles. This point will be discussed in detail in **Section 3.3**.

From the $\phi - P/E$ relation, it is also possible to characterize the bulk properties of the assemblies through the definition of the bulk modulus K:

$$K(\phi) = \frac{dP}{d\phi} \cdot \frac{d\phi}{d\varepsilon}. \tag{3.1}$$

Figure 3.3 shows the evolution of $K(\phi)$ as a function of ϕ in assemblies of pentagons and disks (inset). We observe that the bulk evolution follows the same trends, regardless of the shape of the particles and friction. K appears to be an increasing function of ϕ, with divergence at ϕ_{max}. This divergence is expected since the system tends to oppose its own compression due to the progressive filling of the void space and the intrinsic incompressible behavior of the particles. In other words, the assembly of soft particles begins to behave as a rigid body.

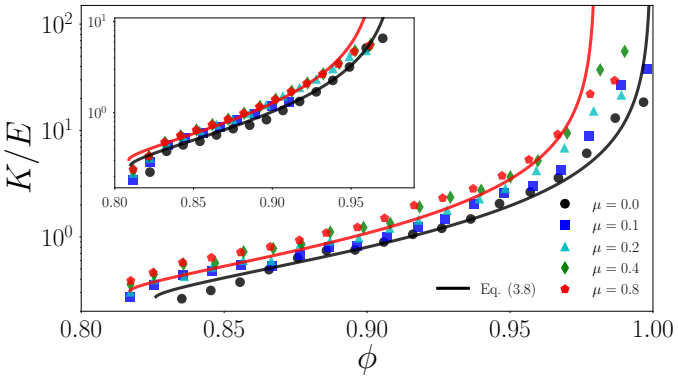

FIGURE 3.3. Evolution of the bulk modulus K normalized by E as a function of the packing fraction ϕ for soft assemblies of pentagons and disks (inset). The predictions given by Eq. (3.8) are shown in continuous lines.

In this section, we observe that, at the macroscale, the compaction behavior beyond the jamming of assembly of soft pentagons and soft disks is similar. Small differences appear mainly on the values of the maximum packing fraction that each system can reach, which mainly depends on the friction.

3.3 Microstructural aspects

3.3.1 Particle connectivity

Figure 3.4 show the evolution of Z as a function of ϕ for pentagons and discs assemblies (inset) and different friction values. As consistently reported in the case of circular shapes, Z increases following a power-law

$$Z - Z_0 = \xi(\phi - \phi_0)^{\alpha}, \tag{3.2}$$

with $\alpha \sim 0.5$, and $\xi = (Z_{max} - Z_0)/(\phi_{max} - \phi_0)^{\alpha}$, where ϕ_{max} and Z_{max} are the values of Z and ϕ when $P/E \to \infty$. As already discussed, this relation has been observed in simulations and experiments for different kinds of deformable systems (foams, emulsions, rubber-like particles, and more recently in mixtures of rigid and soft particles [35, 79, 111, 156, 164]). We found the same tendency for pentagonal shapes in our simulations, independently of the friction coefficient. Thus, our results extend such relation to non-circular particles assemblies.

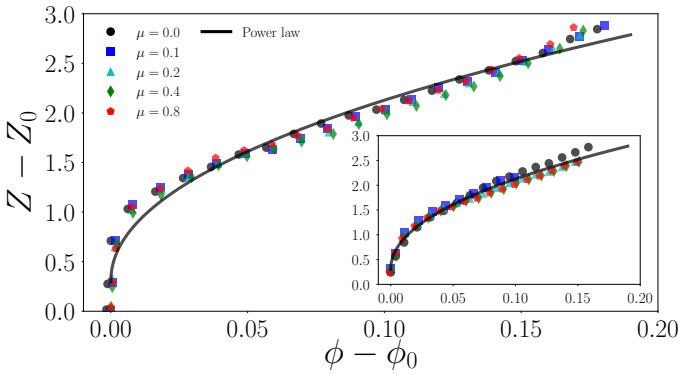

FIGURE 3.4. Evolution of the reduced coordination number $Z - Z_0$ as a function of the reduced packing fraction $\phi - \phi_0$ for assemblies of pentagons and disks (inset), and for different values of friction coefficient. The power-law relation $Z - Z_0 = \xi(\phi - \phi_0)^\alpha$ with $\alpha = 0.5$ and $\xi = 5.1$ is shown in a continuous line.

The particle connectivity can be characterized in more detail by considering P_c, the probability of having c contacts per particle. In Fig. 3.5, P_c is plotted as a function of ϕ for different values of c. We see that P_c is nearly independent of μ for all ϕ values. The evolutions of P_c are basically the same for both assemblies; this is, P_3 and P_4 decreas from ~ 0.2 and ~ 0.4 respectively, to 0, whereas P_6 increases from 0 to ~ 0.6. P_7 increases too, but in a much slower way, from 0 to values close to 0.1. In contrast, P_5 follows a parabola with its maximum value at $\phi \sim 0.92$.

In fact, the coordination number is linked to P_c by $Z = \sum_{c=1}^{\infty} cP_c$. So, the monotonous increases of the coordination number, seen in Fig. 3.2, results from complex compensation mechanisms related to the grains' role in the contact network. The increase in Z with ϕ comes from the increase of $5P_5$ and $6P_6$ until $\phi \simeq 0.92$ and beyond, mainly from $6P_6$ and $7P_7$. Finally, the variations of $3P3$ and $4P4$ with ϕ have a minor effect on Z because of the low value of c.

3.3.2 Particle rearrangements

Following the definition presented in **Section 2.3.2** , Fig. 3.6 shows a color map of the particle rearrangement parameter for each particle at three different levels of compaction in the frictionless case. For disks, we observe that although on average, the non-affine movement is lower than in the case of pentagons, these rearrangements are more localized, with small zones of higher dynamics at different stages of the compaction. Since no friction and edges are blocking the movement, disks can easily rearrange and find a state of min-

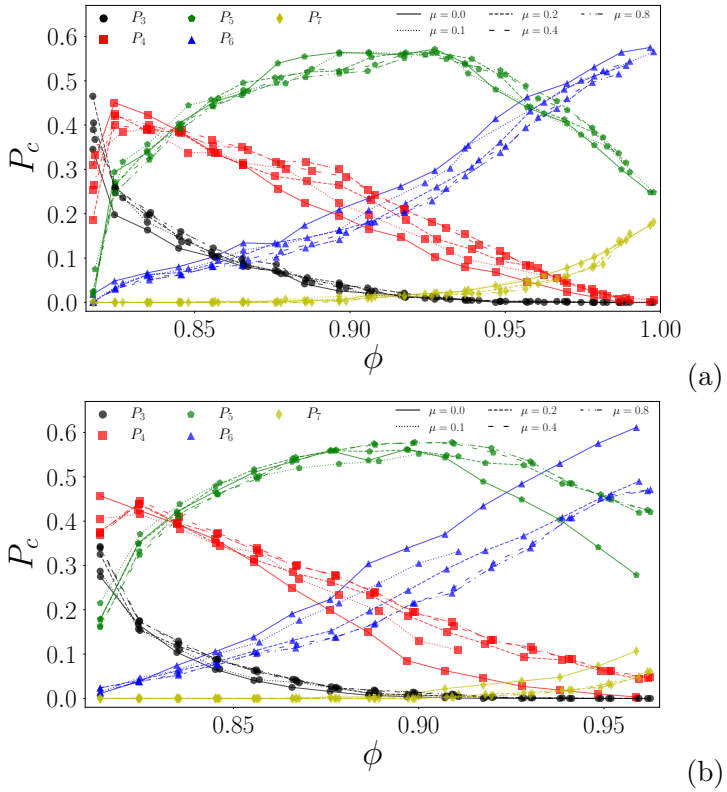

FIGURE 3.5. Evolution of particle connectivity P_c as a function of ϕ: for assemblies of (a) pentagons and (b) for discs.

imum energy more rapidly. On the other hand, the non-affine movement for pentagons, for high compaction values, is much more homogeneous with no clear zones of strong dynamics. This is because, as opposed to disks, the geometry of the pentagons prevents the free movement of the particles, only allowing the non-affine movement in certain specific directions along the particles' edges, not always the best direction to reach the state of minimum local energy.

In the inset of Fig. 3.7 we see the evolution of the mean value of the rearrangement parameter $\hat{\theta} = \langle \hat{\theta}_i \rangle_i$ as a function of the packing fraction, for $\mu = 0$ and $\mu = 0.8$. Basically, for low friction coefficient, $\hat{\theta}$ slowly increases with ϕ, while it decreases for larger friction coefficients. In other words, the particle rearrangements, although small, occurs even after the jamming point and at each stage of the deformation.

To have a better idea of the reorganization of the particles along the compaction process, we compute $\hat{\theta}_\phi$, the asymptotic value of $\hat{\theta}$ as the packing fraction goes to ϕ_{max}, and plot it as a function of the friction coefficient in Fig. 3.7. We see that low friction allows larger particle rearrangements while high friction tends to prevent it. Another point to

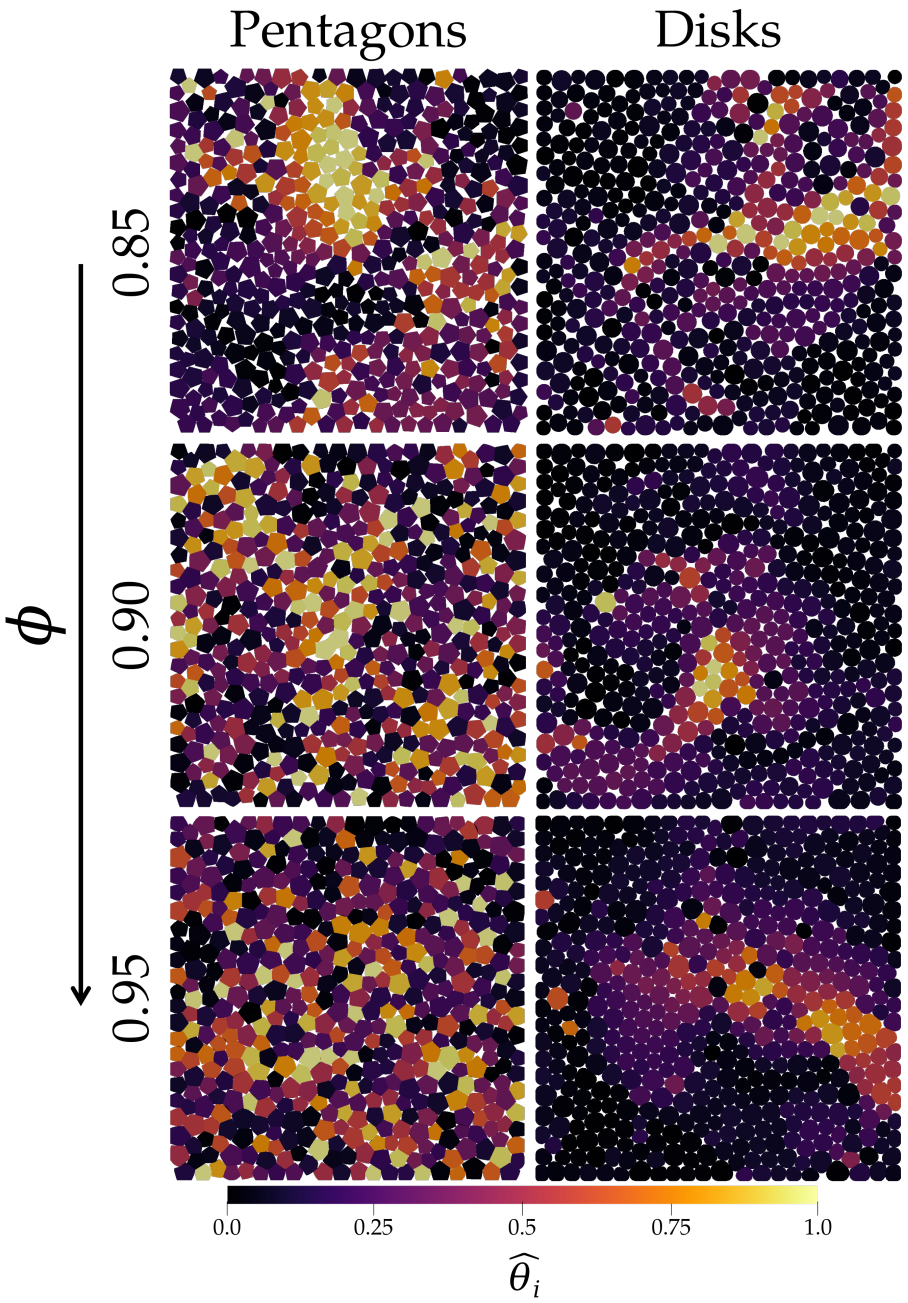

FIGURE 3.6. Color map of the particles rearrangement parameter $\hat{\theta}_i$ in assemblies of frictionless disks and pentagons for different levels of compaction.

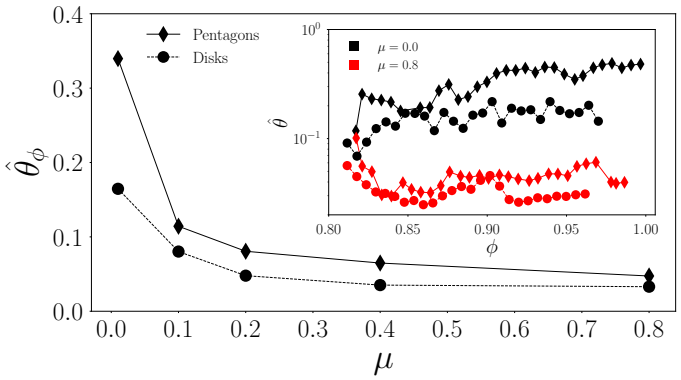

FIGURE 3.7. $\hat{\theta}_\phi$ as a function of the friction coefficient for assemblies of pentagons (continuous line) and disks (dashed line). The inset shows the evolution of $\hat{\theta}$ as a function of the packing fraction ϕ for two different values of friction.

note is that the particle reorganization is higher in pentagon assemblies. In this case, sliding is enhanced by side-side contact as previously shown in rigid particle assemblies [57, 183]. From these measures, we can deduce that the differences in the evolution of the compaction curves observed in Fig. 3.2 are related to the small local rearrangements in the system. This observation also highlights the irreversible nature of the compaction beyond the jamming, confirming recent works [13, 80].

3.3.3 Shape parameter

We study the evolution of the particle shapes through the circularity index with the definition presented in **Section 2.3.3**,

$$\hat{R} = \left\langle 4\pi \frac{V_i}{a_i^2} \right\rangle_i , \tag{3.3}$$

with a_i the particle perimeter and $\langle ... \rangle_i$ the average over the particles in the volume V.

In Fig. 3.8(a), we present the evolution of the excess circularity as a function of the excess packing fraction for different values of the friction coefficient for pentagons, and disks in the inset. For disks, $\hat{R}_0 = 1$, and for pentagons, $\hat{R}_0$ is $\simeq 0.86$ (the value of the circularity for regular pentagons). For disks, $-(\hat{R} - \hat{R}_0)$ increases following a power-law with an exponent ~ 2.6 for the frictionless case, and ~ 2.4 for friction coefficients $\mu > 0.2$ (as already discussed in **Section 2.3.3**). As shown in Fig. 3.8(b), the disks turn progressively into non-regular polygonal shapes with rounded corners. In contrast, for pentagons, $-(\hat{R} - \hat{R}_0)$ decreases with $(\phi - \phi_0)$ to a minimum friction-dependent value and

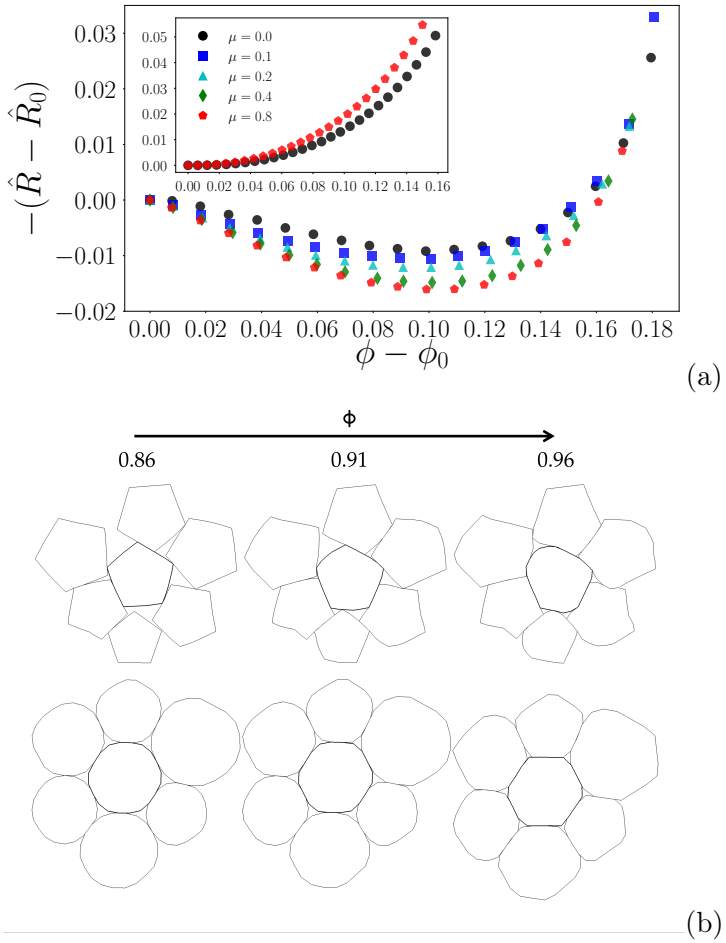

FIGURE 3.8. (a) Evolution of $\hat{R}-\hat{R}_0$ as a function of ϕ for different values of friction in assemblies of pentagons and disks (inset). (b) Group of particles extracted from the assemblies of pentagons and disks, respectively, undergoing the same cumulative packing fraction.

quickly increases, regardless of the friction, not displaying the same power-law tendency observe in the case of disks. Initially, as illustrated in Fig. 3.8(b), the pentagons tend to adopt a rounded and regular shape by smoothing the corners. However, beyond a maximal circularity value, a non-regular polygonal shape is observed. This, along with intruding-corner effects into free space, are some of the facts that contribute to pentagons achieving higher packing fraction compared to assemblies of disks.

3.3.4 Specific contact length

Figure 2.10 shows the evolution of the excess average specific contact length per particle (as defined in **Section 2.3.4**) as a function of the excess packing fraction for pentagons with friction coefficients and disks in the inset.

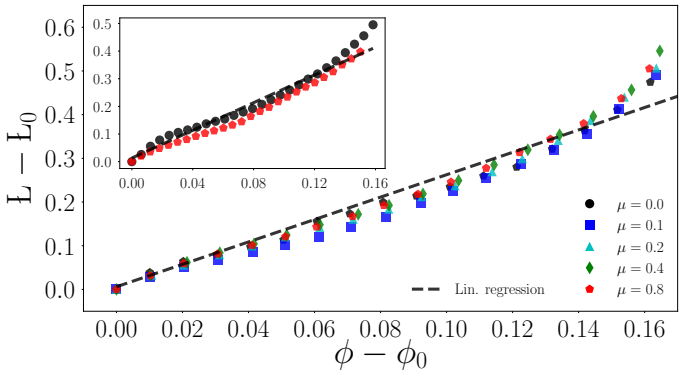

FIGURE 3.9. Evolution of the excess of the average contact length $Ł - Ł_0$ as a function of the excess packing fraction $\phi - \phi_0$ for pentagons for different friction coefficient μ. The inset displays the same information but for disks. The dashed lines in both figures are linear fits with a similar slope ~ 2.5.

Following similar behavior observed for disks (see inset of Fig. 2.10), the excess of average specific contact length follows a linear tendency with the excess packing fraction also for pentagons assembly. The important point to note here is that for both, the linear regression has approximately the same slope $m \sim 2.6$, which suggests that the contact length between particles depends mainly on the material properties, leaving aside their shape.

3.3.5 Force distribution

Figure 3.10 shows a view of the normal force network in assemblies of pentagons and disks at the jammed state and for ϕ close to 1. Here, the total contact force between two particles is computed as the vectorial sum of the forces at the contact nodes along the common interface (a line in 2D). The force network density (i.e., the number of force chains) increases as ϕ increases because, as discussed before, the mean number of contacts per particle increases. In particular, in the case of pentagons close to the jammed state, we observe slightly stronger and more tortuous force chains, compared with disks. But, far beyond the jamming point, the force network appears to be more homogeneous in both cases.

The probability density functions (PDF) of the normal forces f_n normalized by the mean normal force $\langle f_n \rangle$ for frictionless assemblies of pentagons and disks are shown in Fig. 3.11. As it is usually observed, the density of forces above the mean value, at the jamming

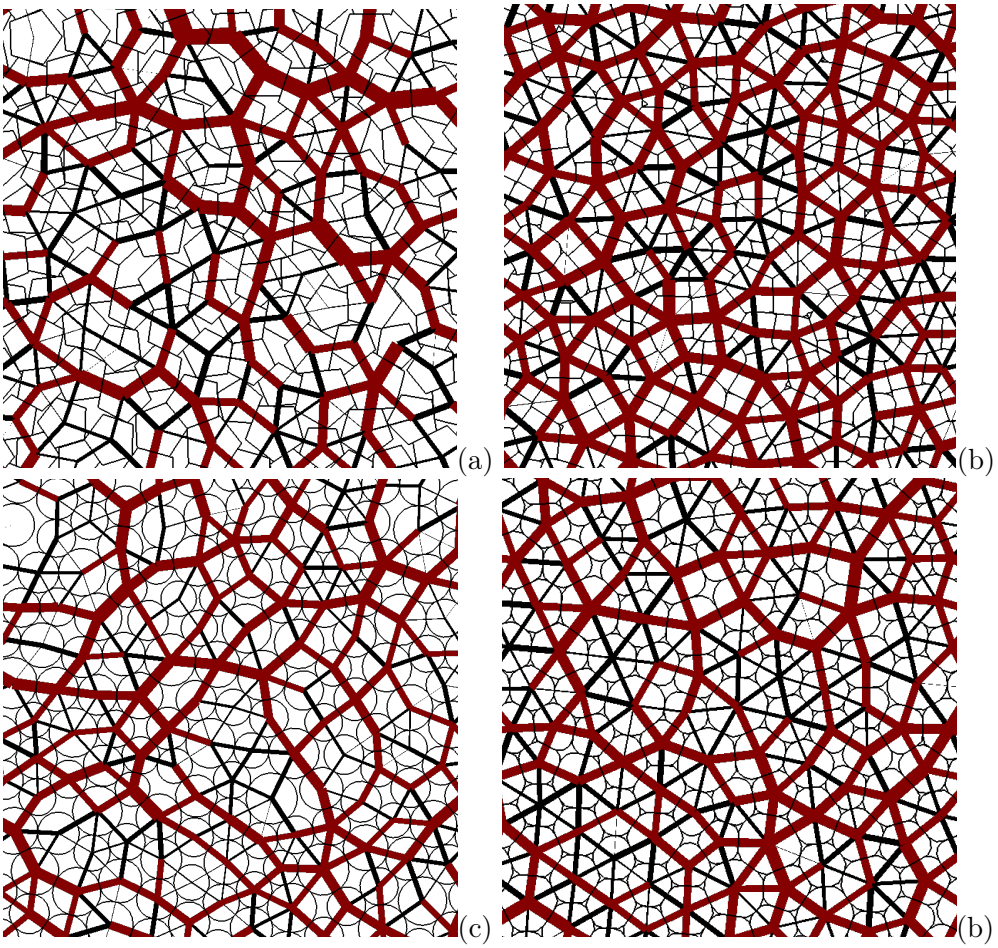

FIGURE 3.10. Close-up views of the force chains in frictionless assemblies of pentagons (a,b) and disks (c,d) at the jammed state (a,c) and for $\phi \sim 1$ (c,d). The magnitude of each normal force is represented by the thickness of the segment joining the centers of the particles in contact. The strong forces ($f_n \geqslant \langle f_n \rangle$) and weak forces ($f_n < \langle f_n \rangle$) are plotted in red and black, respectively.

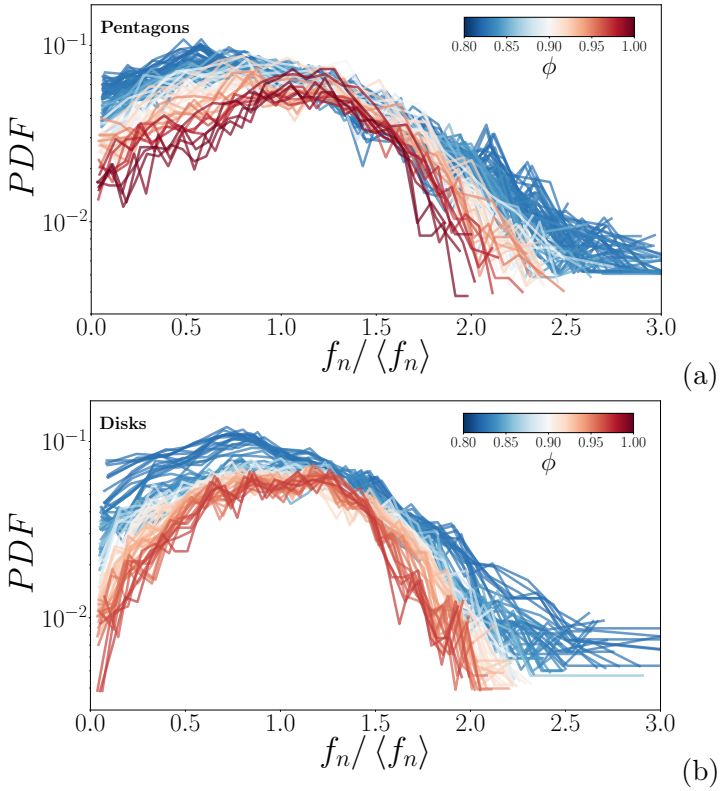

FIGURE 3.11. Probability distribution function of the normal forces f_n normalized by the average normal force $\langle f_n \rangle$ for frictionless (a) pentagon and (b) disk packings, and for different packing fraction.

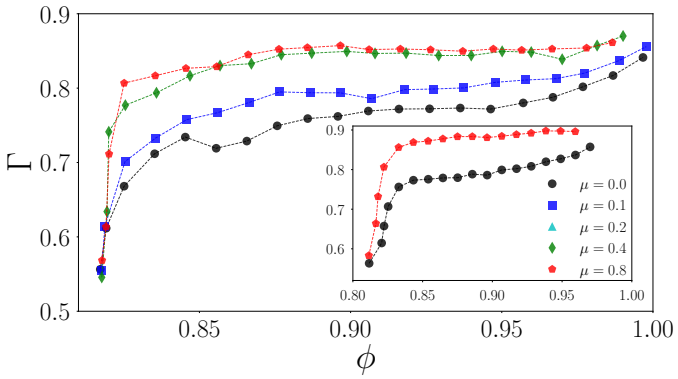

FIGURE 3.12. Participation number Γ as a function of ϕ for assemblies of pentagons and disks (inset) and different friction coefficients.

point, has an exponential decay, whereas the density of forces below the mean follows a power law [62, 173].

At the jamming point (dark blues in Fig. 10), the difference between the packings is almost indiscernible except for a longer exponential decay in the packings of pentagons. This difference is also seen in the wider contact lines in Fig. 3.10.(a) vs. Fig. 3.10.(c), which is consistent with previous analyses [183]. On the contrary, for higher pressures, it is observed that the disks reach highly homogeneous PDFs, with distributions closer to Gaussian-like forms, in complete agreement with previous results presented by Kramar et al. [184]. For pentagon packings, the normal force distributions also tend to Gaussian-like forms but do not reach a very high homogeneity, preserving clear power laws for weak forces and having shorter exponential tails for strong forces. Yet, as in the disks, they show a higher density of normal forces around the mean value as the packing fraction increases.

The degree of homogeneity of the normal force network can be quantified by the participation number Γ defined as [18] (**Section 2.3.6**):

$$\Gamma = \left(N_c \sum_{i=1}^{N_c} q_i^2 \right)^{-1}, \tag{3.4}$$

where N_c is the total number of contacts in the system and $q_i = f_i / \sum_{j=1}^{N_c} f_j$, with f_i the magnitude of the normal force at the contact i. For a homogeneous force distribution, Γ is equal to 1, while the limit in which the forces are completely heterogeneous corresponds to $\Gamma \simeq 0$. The evolution of Γ as a function of ϕ is shown in Fig. 3.12. In general, Γ increases with ϕ from $\sim$ 0.6 at the jammed state to values close to 0.85 at ϕ close to

unity. These variations of Γ verifies that the force chain network becomes more dense and homogenous as the packing fraction is increased far beyond the jammed point. It is worth noting that Γ increases with the friction, which suggests that the friction contributes to a faster homogenization of the force network.

3.3.6 Particle stress distribution

According to the definition of the tensorial moment (Eq. (1.4)), one can assign to each particle i a stress tensor $\boldsymbol{\sigma}^i = \boldsymbol{M}^i/V_i$, where $\boldsymbol{M}^i = \sum_{c\in i} f^c_\alpha r^c_\beta$, with f^c_α the α^{th} component of the contact force acting on the particle i at the contact $c \in i$ and r^c_β the β^{th} component of the position vector of the same contact $c \in i$. From this particle stress tensor, we define the mean particle stress as $P_i = (\sigma^i_1 + \sigma^i_2)/2$, with σ^i_1 and σ^i_2 the principal values of $\boldsymbol{\sigma}^i$. The probability density function (PDF) of this particle stress, normalized by the mean $\langle P_i \rangle$, for frictionless assemblies of pentagons and for increasing packing fraction ϕ, is shown in Fig. 3.13(a). As a first approximation, the general shape of the distribution could be compared to a gaussian distribution around $\langle P_i \rangle$. As the packing fraction increases, the particle stress distribution narrows around the mean value, highlighting the increasing homogenization of the stresses (in a similar way to the normal force distributions).

Figure 3.13(b) shows the evolution of the relative standard deviation SD of the distribution P_p, as a global measure of the heterogeneities, as a function of ϕ. In both assemblies and for all values of inter-particles friction, SD declines with ϕ. Furthermore, we see that for a given value of ϕ, SD declines also with the inter-particle friction. In other words, as observed for the distributions of forces just before (see Fig. 3.12), the particle stress also tends to be more homogeneous as the friction increases.

3.4 Micromechanical approach of the compaction: limit to small deformation

In the previous (**Section 2.4**), the description of the compaction and the evolution of the packing fraction in a soft granular assembly was developed by comparing a system with similar compaction conditions but composed of a single particle. This section aims to address the same description, but from a slightly different perspective, the consideration

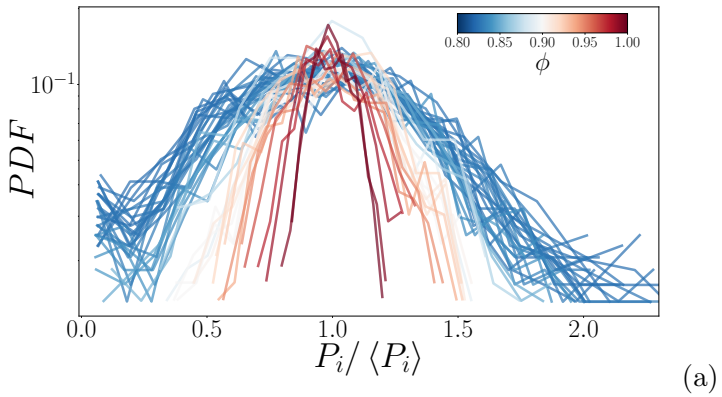

(a)

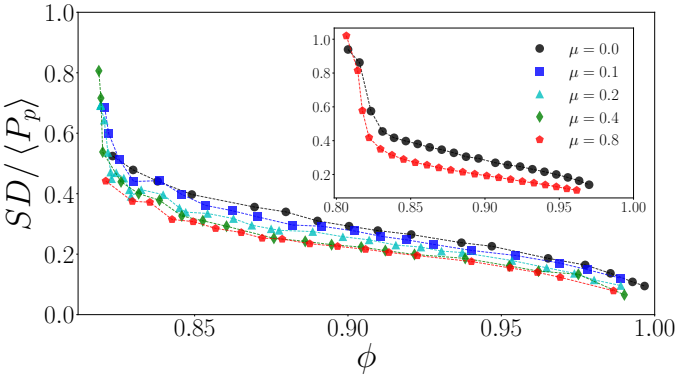

(b)

FIGURE 3.13. (a) Probability distribution function of the particle stress P_i, normalized by the mean $\langle P_i \rangle$, for frictionless assemblies of pentagons and increasing packing fraction ϕ. (b) Standard deviation of the distribution P_p as a function of the packing fraction ϕ for assemblies of pentagons and disks (inset) and for various values of the friction coefficient.

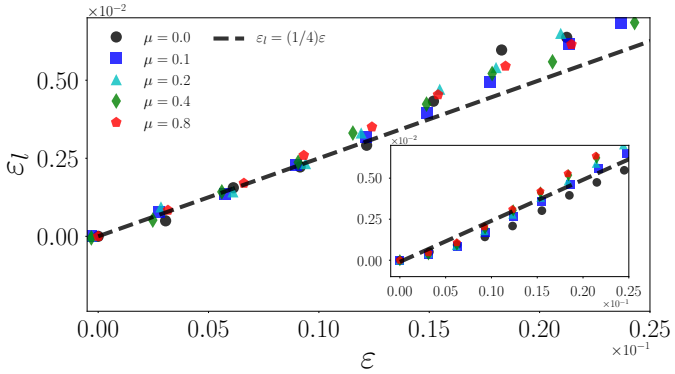

FIGURE 3.14. Macroscopic volumetric strain ϵ_v as a function of the local strain ε_ℓ at the small deformation domain in assemblies of pentagons and disks (inset) for different values of friction.

of regular non-circular particles and the limit to small deformations of previous theoretical developments.

In this direction, considering the volume V_i of a regular polygonal particle with n_s sides, $V_i = (n_s d^2/8)\sin(2\pi/n_s)$, we can write the contact density as $n_c \simeq 4\phi Z/(n_s d^2 \sin 2\pi/n_s)$. Therefore, we get that the pressure from the stress tensor $\boldsymbol{\sigma}$ (Eq. (2.8) in **Chapter2**) takes the following form:

$$P \simeq \frac{\phi Z}{\frac{n_s}{2}\sin\frac{2\pi}{n_s}}\sigma_\ell, \tag{3.5}$$

with $\sigma_\ell = \langle f^c \cdot \ell^c \rangle_c / \langle d \rangle^2$, a measure of the mean contact stress, with $\cdot$ the scalar product.

3.4.1 Small deformation approach

Let us consider the particle assemblies as a network of bonds of length ℓ_c, centered on the contact point of two particles. In the case of small and elastic deformations, we get that $\sigma_\ell \sim \langle f^c \rangle_c / d = E\varepsilon_\ell$, with $\varepsilon_\ell = \langle \ln(\ell^c/d) \rangle_c$ a local strain, defined as the mean bond strain is still valid for assemblies of soft pentagons. Furthermore, our simulations, for random packings and at small deformation, show that the local strain and the macroscopic volumetric strain are linearly dependent as $\varepsilon_\ell \simeq (1/4)\varepsilon_v$ (Fig. 3.14). Then, considering that $Z \to Z_0 \simeq 4$, Eq. (5.5) leads to:

$$\frac{P_{sd}}{E} = -\frac{\phi}{\frac{n_s}{2}\sin\frac{2\pi}{n_s}} \ln\left(\frac{\phi_0}{\phi}\right), \tag{3.6}$$

the limit of $P(\phi)$ at small and elastic deformations.

The prediction given by Eq. (3.6) is shown in Fig. 3.2. As expected, we see a fair approximation of the compaction evolution in the small-strain domain but an increasing mismatch as the solid fraction increases.

3.4.2 Large deformation approach

As discussed in **Section 1.3.2**, there are various theoretical approximations that relate P as a function of ϕ for large deformations [3,11,16,24,40,89,90,93]. All of them are based on different macroscopic assumptions that forget the micromechanical fundaments revealed by Eq. (3.5), and thus, fitting parameters are needed to adjust the proposed theoretical expressions to the data. Nonetheless, it is relevant to note that most of them find that $P \propto \ln[(\phi_{max} - \phi)/(\phi_{max} - \phi_0)]$.

In the micromechanical development presented here, the challenging task consists in finding a functional form for both $\sigma_\ell(\phi)$ and $Z(\phi)$. First, for $\sigma_\ell(\phi)$ taking advantage of the proportionality of P with ϕ, together with Eq. (3.5), it is easy to show that $\sigma_\ell = -\alpha \ln[(\phi_{max} - \phi)/(\phi_{max} - \phi_0)]$. Where the coefficient $\alpha = (\phi_{max} - \phi_0)/(4\phi_0)$ is obtained from the limit to small deformation of Eq. (3.6). Second, we have shown that $Z(\phi)$ evolves as a power law of ϕ following Eq. (3.2). Then, using the above relations, together with Eq. (3.5), we get the final expression of P as a function of ϕ:

$$\frac{P}{E} = -\left(\frac{\phi_{max} - \phi_0}{4\phi_0 \frac{n_s}{2} \sin\frac{2\pi}{n_s}}\right) \{Z_0 - \xi(\phi - \phi_0)^\alpha\} \phi \ln\left(\frac{\phi_{max} - \phi}{\phi_{max} - \phi_0}\right). \tag{3.7}$$

Figure 3.2 presents our numerical data for pentagons and disks (inset) assemblies together with the compaction equation given by Eq. (3.7) for $\mu_s = 0$ and $\mu_s = 0.8$. The predictions given by Eq. (3.7) are in good agreement with our simulations, capturing the asymptotes for small and very high pressures, the effect of the coefficient of friction and the effect of the particle shape. In contrast to previous models, the only unknown parameter in this new model is the maximum packing fraction ϕ_{max}, all other constants are determined from either the initial state, the mapping between the packing fraction and the coordination number, and the number of sides of the particles.

Going one step further, derivating Eq. (3.7) following Eq. (3.1) and neglecting small terms on $\phi \ln \phi$, we can obtain an explicit equation for the Bulk evolution

$$\frac{K}{E} = \left(\frac{\phi_{max} - \phi_0}{4\phi_0 \frac{n_s}{2} \sin \frac{2\pi}{n_s}} \right) \frac{\phi^2}{(\phi_{\max} - \phi)} \{Z_0 + k(\phi - \phi_0)^\alpha\}. \tag{3.8}$$

Fig. 3.3 shows the evolution of the above relation K/E as a function of ϕ, with a good fit for $\mu = 0.0$ and $\mu = 0.8$.

3.5 Conclusions

We investigate the compaction behavior of assemblies composed of soft pentagons by means of non-smooth contact dynamics simulations. In order to see the effects of particle shape, we also simulate assemblies composed of soft circular particles. In both cases, the soft particles are simulated following a hyper-elastic neo-Hookean constitutive law using classical finite elements. The effect of friction was also systematically investigated by varying the coefficient of friction from 0 to 0.8. From the jammed state, packings were isotropically compressed by applying a constant velocity on the boundaries.

As a general finding, we observed that beyond the jamming state, both systems have similar behavior. At the macroscopic scale, the packing fraction increases rapidly and tends asymptotically to a maximum value ϕ_{max}, where the bulk modulus diverges. At the microscopic scale, we show three important facts. First, the particle rearrangement is still important even after the jamming point. Second, the power-law relation between the coordination number and the packing fraction is still valid for assemblies of soft pentagons. And third, the contact forces and particle stress distributions become less broad as the level of compaction increases.

The main differences between the two systems come from the effect of friction. Basically, ϕ_{max} declines as the friction is increased, but it decreases faster in assemblies of pentagons than in assemblies of disks. At the micro-scale, the rearrangement of the particles is higher for soft pentagons, although it declines as the inter-particle is increased. Interestingly, the friction between the particles also contributes to a better homogenization of the contact force network in both systems.

Another relevant result is the extension of the compaction equation previously established for soft and soft-rigid mixture circular assemblies of particles, presented in the previous chapter, to soft non-circular particle assemblies. An advantage of this new approach over the approach of the previous chapter is that it reproduces the same compaction equation but reduces the number of parameters to only one, the maximum packing fraction that the system can reach. This new model, derived from the micromechanical expression of the granular stress tensor and its limit to small and elastic deformation, is based on the joint evolution of the particle connectivity and the contact stress.

Finally, the good numerical results of the compaction model developed in this chapter and the previous one motivate its experimental validation and extension to other types of loading conditions, such as uniaxial loads, which are presented in the next chapter.

CHAPTER 4

Compaction of mixtures of rigid and soft particles: experimental study

In this chapter, to improve our understanding of the behavior of real granular materials, we perform a set of experiments applying oedometric compaction of 2D bidisperse granular media made of both soft (hyperelastic) and rigid grains, varying their proportion. The importance of this study is not only on the validation of the numerical findings presented in the previous chapters, but is also in the design of new constitutive equations and a new experimental approach. The experimental set-up is based on the very accurate imaging of a granular system coupled with a digital image correlation software dedicated to granular matter. Media composed of both soft and rigid grains are uniaxially compressed in this set-up and their evolution is followed all along the loading. We measure the evolution of the main mechanical observables, from the global ones (pressure, packing fraction, coordination...) down to the strain field inside each particle, for systems far beyond the jamming point. First, we corroborate power law and linear relations between local parameters such as the circularity and the contact length as a function of global parameters such as the packing fraction and the applied pressure. Second, we validate and extend the compaction model presented in the previous chapters. Finally, we introduce a critical strain separating two different linear regimes in the compaction process, independently from the mixture

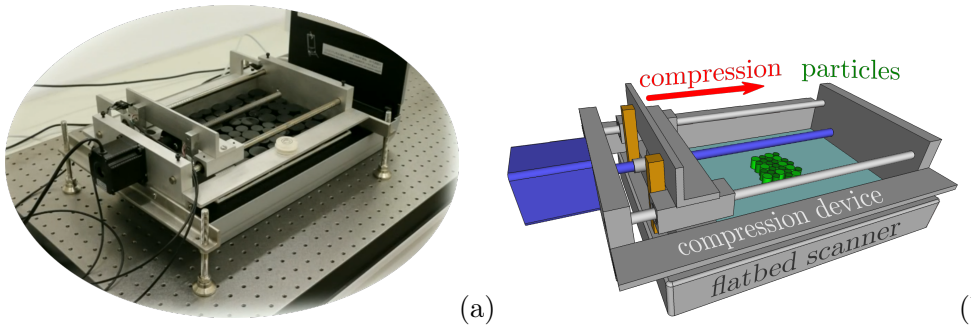

FIGURE 4.1. Experimental set-up. A bidimensional bidisperse granular system, composed of soft and rigid particles, lays on the top glass of a flatbed scanner. An oedometric compression device stresses it while it is imaged from below by a scanner. (a) Photo and (b) digital representation of the experimental set-up.

ratio. Above this critical loading, the granular system behaves like a bulk one displaying a linear relation between the local strain and the global stress.

4.1 Experimental approach

4.1.1 Experimental set-up

The experiment consists of a bidimensional piston of initial dimension (270×202) mm^2 which compresses oedometrically a bidisperse assembly of rigid and soft cylinders with parallel axis, randomly and gently (avoiding strong contacts between particles) placed on top of a flatbed scanner. The loading piston is composed of a stepper motor rotating a screw that moves the edge of the piston in the inward direction. Two force sensors are attached to this latter. Figure 4.1(a) shows a photo of the experimental device described in the previous lines, with its digital representation in Fig. 4.1(b). The force sensors continuously measure the force (F) evolution in the compression direction at a frequency of 100 Hz, and the pressure P in the same direction is directly computed (σ_{yy} by convention). For each loading step, the piston moves of 0.5 mm at a speed of 2 mm/min to assure that we are always in the quasistatic regime. Then, the system relaxes during 1 min and is imaged from below with a high-resolution scanner [185] at a resolution of 2400 pi (10.6 μm/px). The compaction stops when the force in the perpendicular direction to the scanner plane is high enough that it causes the particles to leave the scanner plane. Figure 4.2 shows the evolution of the measured force as a function of the global strain $\varepsilon = ln(\phi/\phi_0)$ for different mixture ratios.

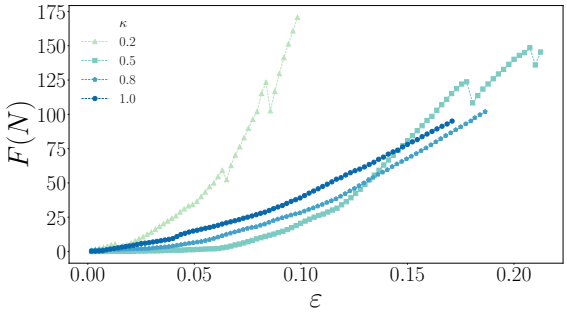

FIGURE 4.2. Evolution of the measured force, F, as a function of the global strain, ε, for different values of mixture κ.

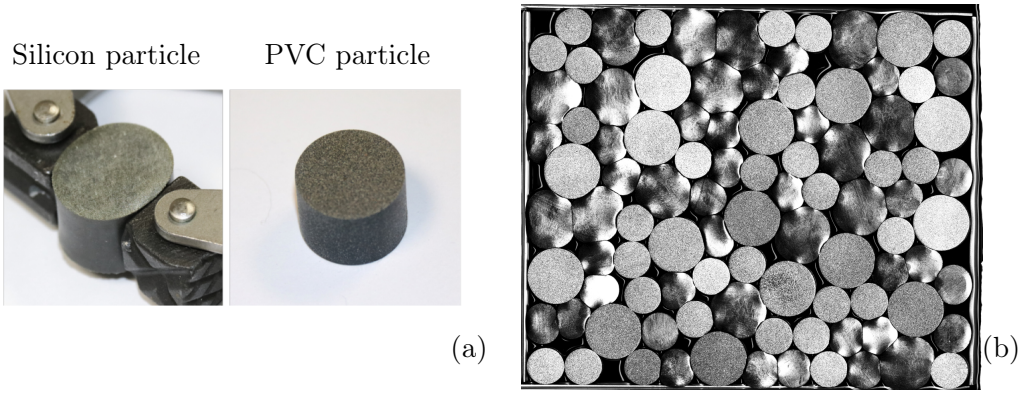

FIGURE 4.3. (a) Squeezed soft silicon particle and PVC particle used in the experiment. (b) Scan of a compressed random configuration of particles with soft/rigid mixture ratio $\kappa = 0.5$.

The compressed granular systems are composed of both hyperelastic silicone cylinders [79,186] and rigid PVC cylinders (see Fig. 4.3(a)) with young moduli $E = 0.7$ MPa [23] and 1.2 GPa, respectively. In both cases the Poisson ratio is close to 0.5, since the two materials can be considered as uncompressible. Both soft and rigid cylinders are bidisperse in size with diameters of 20 mm and 30 mm and height of 15 mm. For each experiment, about $n = 100$ particles are used with the ratio between rigid and soft particles $\kappa = \mathrm{N_{soft}/N}$, where N is the number of particles. This ratio is equally spread among soft and rigid particles and varies in the set $\kappa \in [0.2, 0.5, 0.8, 1.0]$. Figure 4.3(b) shows a raw scanned image of a highly compressed mixture packing with $\kappa = 0.5$. To avoid basal friction, the scanner glass is coated with oil which also lubricates the contacts between particles, making them virtually frictionless. The bottom of each particle is painted with thin metallic glitter, which creates a random pattern with a correlation length of approximately 50 μm [23].

4.1.2 Image processing

For each experiment, a set of about 90 pictures of $\sim$ 500 Mpx shows the evolution of the bottom face of the granular system. These pictures are post-processed with a DIC algorithm modified from [23, 187]. First, each particle center is tracked over the entire set of the images. Particles are detected on the undeformed picture by contrasting the dark background of the images and the bright aspect of the particles (see Fig. 4.3(b)). Then, each particle is tracked from one image to the next one by convolving a small area in the center of the particle picture at the step n (I_n) with the same sub-image at the step $n+1$ (I_{n+1}). The convolution is first done in the Fourier domain using the well-known Fast Fourier Transform (FFT). This increases a lot the convolution computation. The maximum value of the convolution gives the particle translation with an accuracy of one pixel. To improve this measurement to sub-pixel accuracy and to consider particle rotation, the following weight function is minimized for the same sub-images:

$$\mathcal{W}(di, dj, \theta)_{I_n, I_{n+1}} = \sum_{i,j} |I_{n+1} - \mathcal{T}_{di,dj,\theta}(I_{n+1})| \tag{4.1}$$

with $\mathcal{T}_{di,dj,\theta}$ an image/matrix transformation performing a translation of (di, dj) and a rotation of θ by interpolating linearly the image/matrix. Then, the new position of the particles is found, giving both their displacement and their rotations. This permits to track particles individually and for each of them to extract, from the main images, sub-sets of images centered around each particle and correcting the solid rigid motion.

For soft particles, the DIC algorithm proposed for large deformations and already tested in [79] is used to obtain the displacement field ($\{\boldsymbol{u}$) inside each particle from its corresponding sub-set of images. In this latter, a regular grid (about 40 px $\sim$ 400 μm of length per element) is placed on the particle and gives the center of each correlation cell (cf. left panel of Fig. 4.4). The position of each of them is then tracked along the compaction process using a process similar to the one describe for the particle tracking. More particularly, here the size, d, of each correlation cell is self-adapted to contain a significant random pattern (cf. middle panel of Fig. 4.4). The optimum d value is chosen such that it maximizes the correlation obtained by FFT. So then, FFT correlation is performed before a weight function minimization. This latter is similar to the one given in equation 4.1 but without considering the rotation. This computation is parallelized

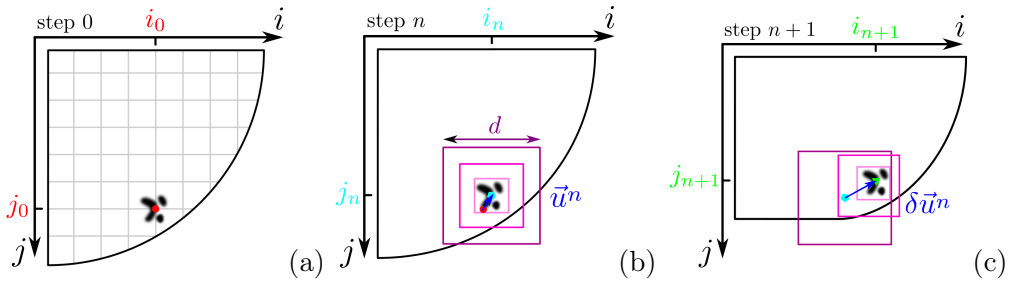

FIGURE 4.4. Schematic view of the digital image correlation algorithm for large deformations on an individual particle. On the initial image at step 0 (a), a regular grid is place on the particle. The system is deformed from the step n and displacement field $\boldsymbol{u}_i^n$ (b) to the step $n+1$ (c) by a small $\delta\boldsymbol{u}^n$ increment such that the new displacement field is $\boldsymbol{u}_i^{n+1} = \boldsymbol{u}_i^n + \delta\boldsymbol{u}_i^n$.

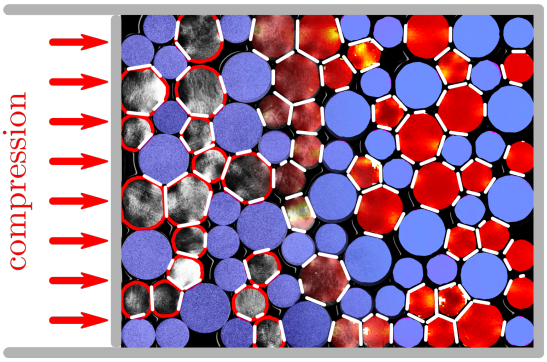

FIGURE 4.5. Composite view of measured fields. Rigid particles are colored in blue. Raw image, in gray level, is shown on the left and in Fig. 4.3(b), particle boundaries are in red. Von Mises strain field, $\mathcal{C}$, is shown on the right with a color scale going from dark red (low value) to yellow (high value). Contacts are shown in white.

over the correlation cells of the particles. Each image n is correlated to the image $n-1$ to consider large deformation and displacements $\delta\boldsymbol{u}^n$ are summed-up from one step to the other. This process gives the displacement field inside each particle $\boldsymbol{u}(x,y)_i^n$ with an accuracy of about 0.01 px ~ 0.1 μm. This DIC process is briefly schematized in Fig. 4.4. For the rigid particles, a similar algorithm is used but instead of correlating image $n+1$ to image n and summing relative displacements, it directly correlates image n to the initial underformed image.

As presented in Fig. 4.5, the particle boundaries are obtained from the displacement fields $\boldsymbol{u}$ [23]. The system packing fraction is directly deduced from it, as well as the particle circularity defined by Eq. (5.8). For the soft particles, the right Cauchy-Green strain tensor field, $\boldsymbol{C}$ is computed [23, 155] and its von Mises strain, $\mathcal{C}$, is deduced. For the rigid particles, the local stresses are too low to induce any significant deformation of the PVC, so we assume that they do not deform. Finally, contacts between particles and their

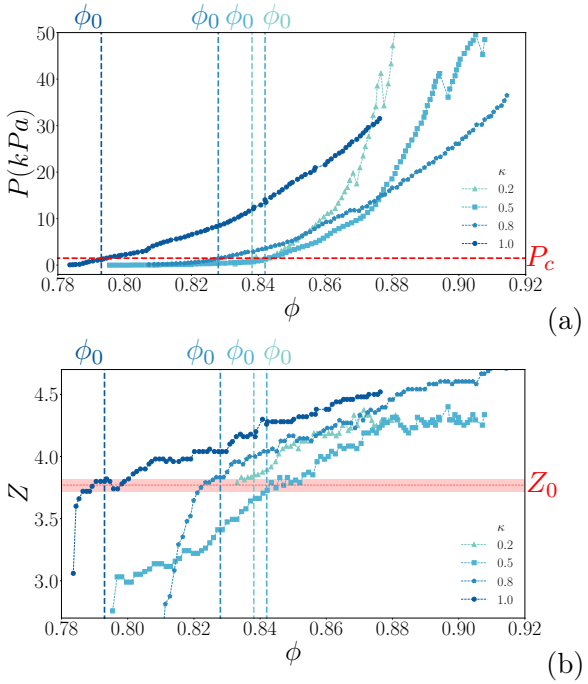

FIGURE 4.6. (a) Evolution of the pressure as a function of the packing fraction. An horizontal dashed red line is plotted for $P = 1$ kPa. (b) Evolution of the coordination number as a function of the packing fraction. The horizontal dashed red line shows the critical coordination number Z_0 at the defined jamming transition. In both figures the different curves correspond to different soft/rigid ratio, κ. In both figures, vertical dashed lines show the values of the packing fraction at the jamming transition.

contact length, l_i, are measured from the proximity of the boundaries and the von Mises strain.

4.2 Macroscopic aspects

4.2.1 Jamming transition

The jamming transition corresponds to the transition of a granular system from a fluid-like to solid-like behavior. Many definitions of this transition exist associated with different experimental ways to detect it (see **Section 1.2.1**). In this experiment, we have selected the jamming transition point where the system can support a non-negligible load. From the measurement accuracy of the force sensors, this load has been chosen to be $P_c = 1$ kPa. This value corresponds to a different jamming packing fraction ϕ_0 for each mixture (see Fig. 4.6 (a,b)), and well-defined critical coordination number $Z_0 = (3.77 \pm 0.05)$ (see Fig. 4.6 (b)). The chosen criterion to determine the jamming transition finds its agreement

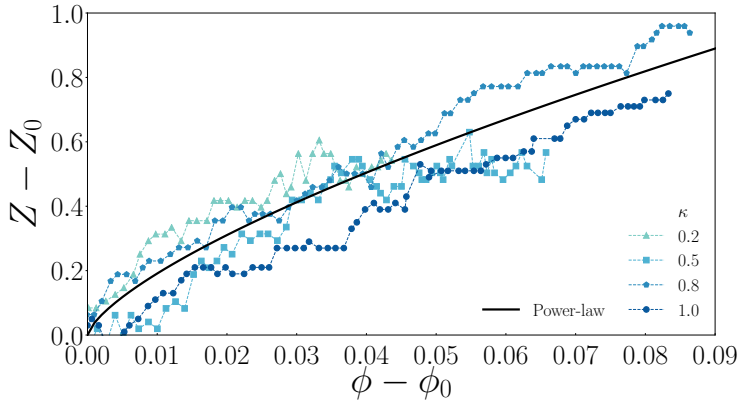

FIGURE 4.7. Evolution of the excess coordination number, $Z - Z_0$, with $Z_0 \approx 3.8$, as a function of the excess packing fraction, $\phi - \phi_0$ for different mixtures ratios κ. The solid line is the power-law relation $Z - Z_0 = \xi(\phi - \phi_0)^\alpha$, with $\alpha = (0.7 \pm 0.15)$.

in the fact that Z_0 is found to be between 3 and 4 and closer from 4. This corresponds to particles with low friction coefficient [51], which is the case here due to the lubricant added to the system. Considering the smallness of the system, it is remarkable that the jamming transition is observed at an almost constant coordination number, regardless of the κ ratio. This proves that the system is large enough not to be too strongly dependant on the initial conditions.

4.2.2 Particle Connectivity

In the Fig. 4.7 we show the excess of coordination number, $Z - Z_0$, as a function of the excess of packing fraction, $\phi - \phi_0$. All the curves collapse fairly well on the power-law relation $Z - Z_0 = \xi(\phi - \phi_0)^\alpha$ (see **Section 2.3.1**), with exponent $\alpha = (0.7 \pm 0.15)$ and scale parameter $\xi = 4.8$. Although the exponent α is slightly overestimated compared to previous experimental and numerical studies [59, 79, 99] (see **Section 2.3.1**), within the error bars, we are in the same domain of $\alpha \approx 0.5$. This large error bar is mainly due to the smallness of the system. This relation constitutes a first step of the description of local observable from global measurements.

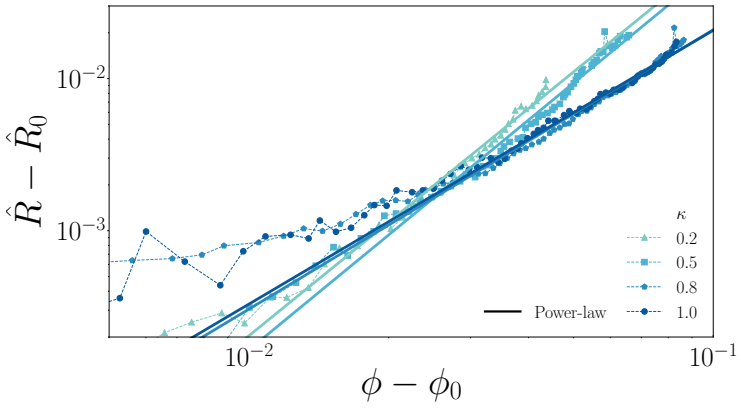

FIGURE 4.8. Evolution of the average of the soft particle excess circularity, $\hat{R} - \hat{R}_0$, as a function of the excess packing fraction, $\phi - \phi_0$. The solid lines are power-law fits for each value of κ.

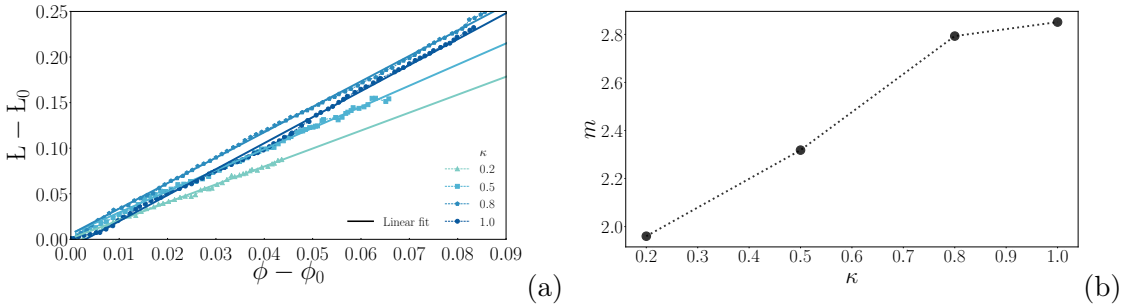

FIGURE 4.9. (b) Evolution of the average value of the excess of specific contact length, $\text{Ł} - \text{Ł}_0$, as a function of the distance to the jamming transition for the packing fraction, $\phi - \phi_0$. The solid lines represent linear fits. (b) Slope of the linear fits a function of κ.

4.3 Microstructural aspects

4.3.1 Shape parameters

Figure 4.8 shows how the average of the soft particle excess of circularity, $\hat{R} - \hat{R}_0$ (defined in **Section 2.3.3**), increases with the excess of packing fraction, $\phi - \phi_0$. Apart from few sharp grain rearrangements, this increase seems to follow a power-law tendency (Eq. (5.8)) with similar exponents, $\beta \approx 2.4,\ 2.5,\ 1.9$ and 1.8 for $\kappa = 0.2,\ 0.5,\ 0.8$ and 1.0, respectively. This power-law tendency is also observed in simulations with a small overestimation for the value of the exponents (see **Section 2.3.3**).

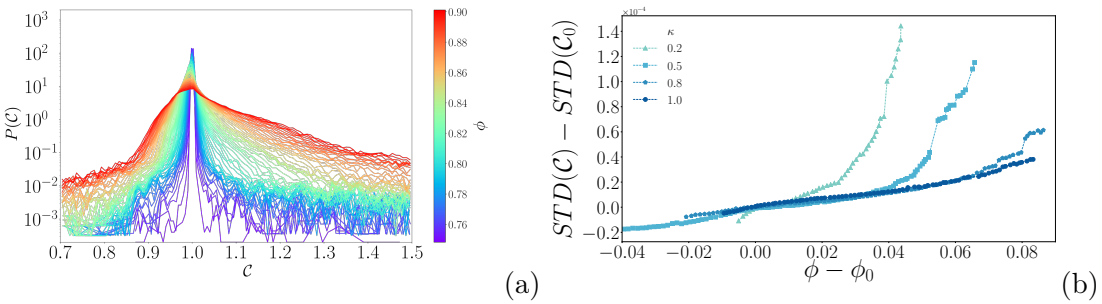

(a) (b)

FIGURE 4.10. (a) Evolution of the probability density function of the von Mises strain, $\mathcal{C}$, for a mixture ratio κ equal to 0.5. The colors of the curves give the packing fraction evolution. (b) Evolution of the relative standard deviation, $STD(\mathcal{C}) - STD(\mathcal{C}_0)$ of the von Mises strain in soft particles as a function of the excess packing fraction, with $\mathcal{C}_0$ the von Mises strain at the jamming point.

4.3.2 Contact length

In Fig. 4.9 we plot the evolution of the average over the particles of the excess specific contact length, $Ł - Ł_0$, with the excess specific contact length defined as the ratio between the contact length and the perimeter of the particle (see **Section 2.3.4**). It increases linearly with the excess of packing fraction for any κ in agreement with our simulations for isotropic compaction. This point is in agreement with numerical results and the analytical solution evidenced in **Section 2.3.4**. Moreover, the slope of the linear fits also increases linearly with the mixture ratio before it gets saturated around 2.8 for $\kappa \approx 0.8$.

4.3.3 Von Misses strain

At the particle scale, it is also possible to relate the strain inside the particles to macroscopic observables. Under the small deformation assumption the infinitesimal strain tensor, $\boldsymbol{\varepsilon}$, is related to the Cauchy-Green strain tensor $\boldsymbol{C}$ by $\boldsymbol{\varepsilon} = 1/2(\boldsymbol{C} - \boldsymbol{I})$, with $\boldsymbol{I}$ the second-order identity tensor. In a compressed bulk material, this strain tensor and the global stress and strain are linearly related. Since deep in the jammed state, the material has a density close to a bulk material, one can wonder if this relation is still observed.

Figure 4.10(a) shows the evolution of probability distribution function of the von Mises strain $\mathcal{C}$ for a mixture ratio $\kappa = 0.5$, during compaction. We see that the average strain evolves during compression, and its distribution gets wider with the increase of the packing fraction. In the Figure 4.10(b), we present the increasing evolution of the standard deviation of $\mathcal{C}$ as a function of the packing fraction. This result was previously observed in [23]

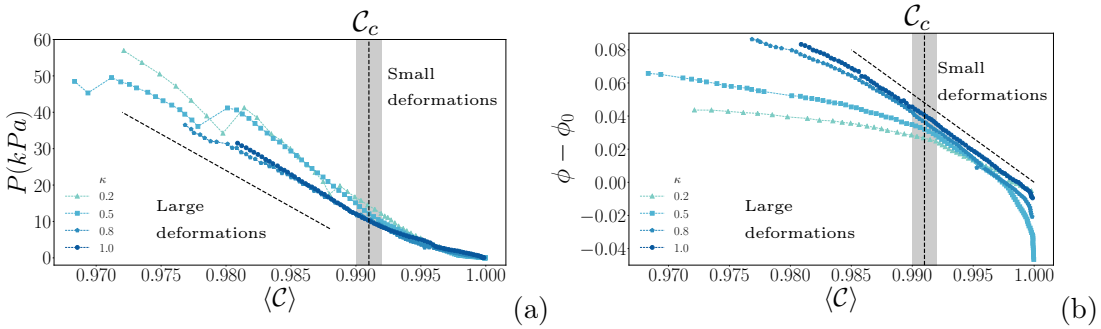

FIGURE 4.11. (a),(b): Evolution of the global stress, P, and of the excess of packing fraction $\phi - \phi_0$, as a function of the average value of the von Mises strain, $\langle\mathcal{C}\rangle$ in soft particles, for different κ values. In (a) and (b) the straight black dashed lines show a slope of 2.2 kPa and 5.4 respectively, displaying the linear regimes. The vertical gray line and the shaded area shows the critical strain $\mathcal{C}_c = 0.991 \pm 1.2 \times 10^{-3}$ and its errorbar, respectively. It splits the space horizontally between small and large deformation levels.

in the study of hyperelastic and plastic particles. When shifted from ϕ_0, curves collapse on a linear law whatever the softness ratio, up to a cut-off which increases linearly with κ. This cut-off value saturate near $\kappa = 0.8$ as already observed for the specific contact length.

As seen in Fig. 4.11(a) and (b), when the system is compressed, the mean von Misses strain $\langle\mathcal{C}\rangle$ inside soft particles decreases from 1 while the pressure and the packing fraction increase. At low compaction level, for $\langle\mathcal{C}\rangle > \mathcal{C}_c \approx 0.991$, it decreases linearly with the packing fraction regardless of the mixture ratio:

$$\langle\mathcal{C}\rangle \sim \phi - \phi_0. \tag{4.2}$$

For a higher level of compression, it leaves this linear regime decreasing more rapidly for higher values of κ. It is worth noting that in the linear regime, all curves collapse regardless of the mixture ratio. On the contrary, at a high compression level, for $\langle\mathcal{C}\rangle < \mathcal{C}_c$, the mean von Misses strain decreases linearly with the global pressure except for some noise due to the particle rearrangements:

$$\langle\mathcal{C}\rangle \sim P. \tag{4.3}$$

For low deformation levels, all curves collapse on a parabolic curve. In the first regime ($\langle\mathcal{C}\rangle > \mathcal{C}_c$), the linearity is reminiscent of the one observed between the global strain scale and the packing fraction (see **Section 3.4.1**). In the second regime ($\langle\mathcal{C}\rangle > \mathcal{C}_c$), the linearity between the local strain and the global stress suggests that the material behaves like a bulk one. This is consistent with the material's low porosity. It is also consistent with the fact

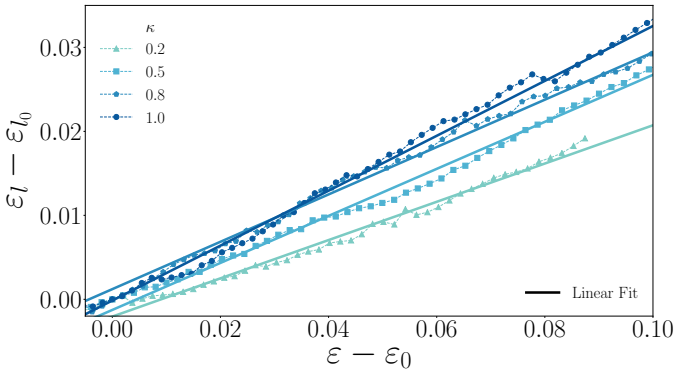

FIGURE 4.12. Macroscopic volumetric strain ϵ as a function of the local strain ϵ_l at the small deformation domain for all κ values.

that, at large compression levels, the pressure decreases faster with the strain for lower mixture ratio: the material gets stiffer for lower κ. On the contrary, in small compression levels, linear relations collapse and do not significantly depend on the mixture ratio.

4.4 Validation and extension of the compaction model

For the description of the compaction of cylindrical particles, the theoretical framework presented in **Section 3.4** is used and adapted to an uni-axial, plain-stress compaction. In this case P is related to the granular stress tensor through its yy component by: $P = \sigma_{yy}$. This consideration, together with the fact that the volume V_i of a cylinder is given by $V_i = \pi L d^2/4$, with L the cylinder height, leads to a slightly different micromechanical expression of P in the form of [188]:

$$P \simeq \alpha_a \frac{Z\phi}{\pi L d^2} \langle \ell \rangle \langle f_n \rangle = \alpha_a \frac{Z\phi}{\pi} \sigma_l, \tag{4.4}$$

where, in this case, $\sigma_l = \langle \ell \rangle \langle f_n \rangle / (L d^2)$, and α_a a constant encompassing various microscopic parameters related to the anisotropy of the contact and force network, specific to uniaxial compression [188]. In practice α_a is hardly measurable in experiments, nevertheless it has been shown that these anisotropies define the macroscopic friction μ_M of the assembly, leading to rewrite $\alpha_a \simeq 1 + \mu_M$ [188], with μ_M known to be close to 0.25 for an assembly of frictional disks, and assimilated here for cylinders.

Additionally, different contact conditions in the small deformation limit must be introduced to deal with the new contacts between cylinders with parallel axis. In this case,

κ	ϕ_0	ϕ_{max}	E^* (MPa)	Γ
0.2	0.836	0.88	2.67	4.38
0.5	0.841	0.93	1.00	3.57
0.8	0.826	0.96	0.62	3.54
1.0	0.791	0.97	0.50	3.05

TABLE 4.1. Parameters used in Eq. (4.6) for the different mixture ratios. For all values of κ, $Z_0 = (3.77 \pm 0.05)$ and $\alpha = 0.7$.

using the Hertz contact law, the mean contact pressure has the following form:

$$\sigma_l \simeq \frac{\pi}{4} E^* \varepsilon_l, \tag{4.5}$$

with E^* the mean effective Young modulus, and ε_l the mean local deformation. In mixtures, thanks to the homogeneous distribution of the particles within the assemblies, with equal mean number of contacts for the two types of particles, it is easy to show that $E^* \approx E/(2\kappa(1-\nu^2))$. Finally, our experiments show that the linear trend between ε_l and ε is preserved. However, the factor of proportionality Γ depends on the mixture ratio (see Fig. 4.12). Table 4.1 presents the values of E^* and Γ for the mixture ratios studied. With these new conditions, the compaction equation is as follows:

$$P \simeq \frac{E^*}{4\Gamma}(1+\mu_M)\frac{\phi_{max}-\phi_0}{\phi_0}(Z_0 + k(\phi-\phi_0)^{0.7})\phi \ln\left(\frac{\phi_{max}-\phi_0}{\phi_{max}-\phi}\right), \tag{4.6}$$

where ϕ_{max} is the asymptotic maximum packing fraction. For $\kappa = 1$, $\phi_{max} = 0.97$ close to 1, while for $\kappa = 0.2$, $\phi_{max} = 0.88$ is closer to the random close packing. The values of the different parameters used in Eq.(4.6) are given in Tab. 4.1.

Figure 4.13 presents our experimental data together with Eq. (4.6) (full lines). We get excellent predictions from Eq. (4.6) for the different values of κ, excepted for $\kappa = 0.2$ for which small discrepancy are observed, although the general tendency is reproduced. For this last case, we can invoke finite size-effect and sharp particle rearrangement due to the small number of deformable grains.

Apart from these small differences observed for the extremely small values of κ, this new step is a clear validation and an extension of our micromechanical approach for the compaction of soft granular media.

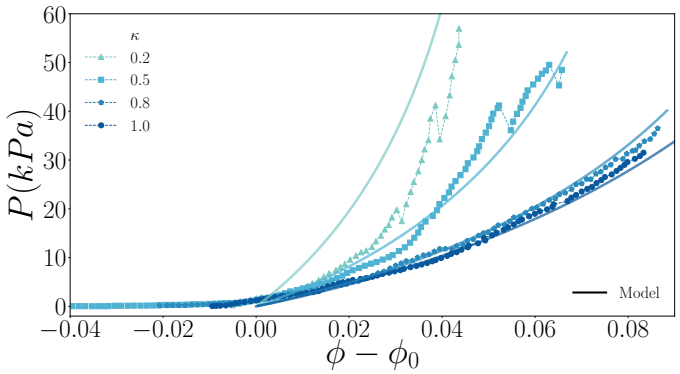

FIGURE 4.13. Evolution of the global stress applied to the system, P, as a functions of $\phi - \phi_0$ for different mixture ratio κ. Plain curves correspond with Eq. (4.6).

4.5 Conclusions

In this chapter, we analyzed experimentally the oedometric compaction of granular assemblies composed of mixtures of both, rigid and deformable cylindrical particles. First, we corroborate the power-law tendency for the excess coordination number as a function of the excess packing fraction, although its exponent is overestimated because of the small size of the system. A power-law relation between the shape parameter and the excess packing fraction also seems to be observed. Second, a linear relation between the specific contact length averaged over the particles as a function of the excess coordination number is seen, in close agreement with the previous chapters. Third, for a small level of deformation, the average strain inside soft particles evolves linearly with the packing fraction, while in the case of high loading levels, it scales with the global pressure applied to the system. This evidences two distinct regimes separated by a critical value independent of κ. Finally, these experimental results validate the compaction model, here developed, in the case of the oedometric compaction of a quasi-two-dimensional system.

In general manner, in the three previous chapters, we showed the direct relation between local properties such as the coordination number or the deformation of the particles with the global properties such as the pressure and the packing fraction. From these relations, we built a theoretical model that, by using the analysis of the local interactions, can reproduce the compaction evolution of materials composed of only deformable particles and also mixtures with solid particles.

CHAPTER 5

Three-dimentional compaction of soft granular packings

This chapter extends the findings in two dimensions to the three-dimensional compaction of assemblies composed of soft (elastic) spherical particles, using the NSCD method. In practice, the three-dimensional studies imply additional numerical and complex difficulties for managing the deformation of the particles, which explain the few numerical analysis on compaction of soft particles assemblies in 3D. The assembly's compactness is characterized by both the evolution of the packing fraction and the coordination number of the particles as the confining stress increases. The microstructure is analyzed in terms of stress distributions within the particles. The 3D simulations follows similar results to the 2D case: the packing fraction increases and tends toward a maximum value close to 1, and the mean coordination number increases as a square root of the packing fraction. As the confining stress increases, a continuous transition is observed from a granular-like material with exponential tails of both the mean and shear stress distributions to a more homogeneous and continuous-like material characterized by Gaussian-like distributions of the mean and shear stresses, which become narrower as the packing fraction increases. Using the formulation of the Hertz law, together with the micromechanical expression of the granular stress tensor and the power-law relation between the packing fraction and the coordination of the particles, we develop a new compaction equation that describes the

evolution of the packing fraction as a function of the applied pressure for assemblies of spheres.

5.1 Numerical Approach

When dealing with three-dimensional and highly deformable particles, a problematic issue is finding the right compromise between sample representativeness and numerical efficiency. In this study, we are interested in the isotropic compression of elastic spherical particles. Therefore, one necessary condition is to verify that the mesh used is, at least, sufficiently accurate concerning the Hertz approximation in the range of small deformation domain [189, 190]. Let us first consider the case of an elastic spherical particle of diameter d, with a Poisson's ratio ν equals 0.495 and a Young modulus E, subjected to axial compression as shown in Fig. 5.1(a). The bottom wall is fixed while the top wall moves downwards at a constant velocity v_0 chosen, such as the inertial effects, defined in this case by $I = v_0\sqrt{\rho_0/E}$ [136], where ρ_0 is the density of the particles, are negligible (i.e., $I << 1$). Figure 5.1(b) shows the evolution of the normal force f as a function of the vertical displacement δ using 444, 808, 6685 and 14688 tetrahedral elements with four nodes, together with the corresponding prediction of the Hertz analysis given by [189, 190]:

$$\frac{f}{d^2} = \frac{2^{3/2}}{3}\frac{E}{1-\nu^2}\left(\frac{\delta}{d}\right)^{3/2}. \tag{5.1}$$

As it can be seen, we have a good prediction for 14688 and 6685 elements, while it fails for 444 elements. On the contrary, with 808 elements, the force-displacement relation is slightly overestimated at the beginning of the deformation, but the response quickly reaches the prediction at higher deformation. Following this simple analysis, we fixed the number of elements to 808 for all the simulations presented below.

In the condition over the number of particles, we adopt a double approach. First, we rely on previously published works by different groups in which it is shown that a number between 32 and 200 particles is sufficient to qualitatively represent the loading surfaces, the compaction, or the plastic flow of a compressed assembly of deformable spherical particles [21, 191–194]. Second, we will adopt a statistical analysis by considering several geometrically independent samples and focusing on their averaged behavior.

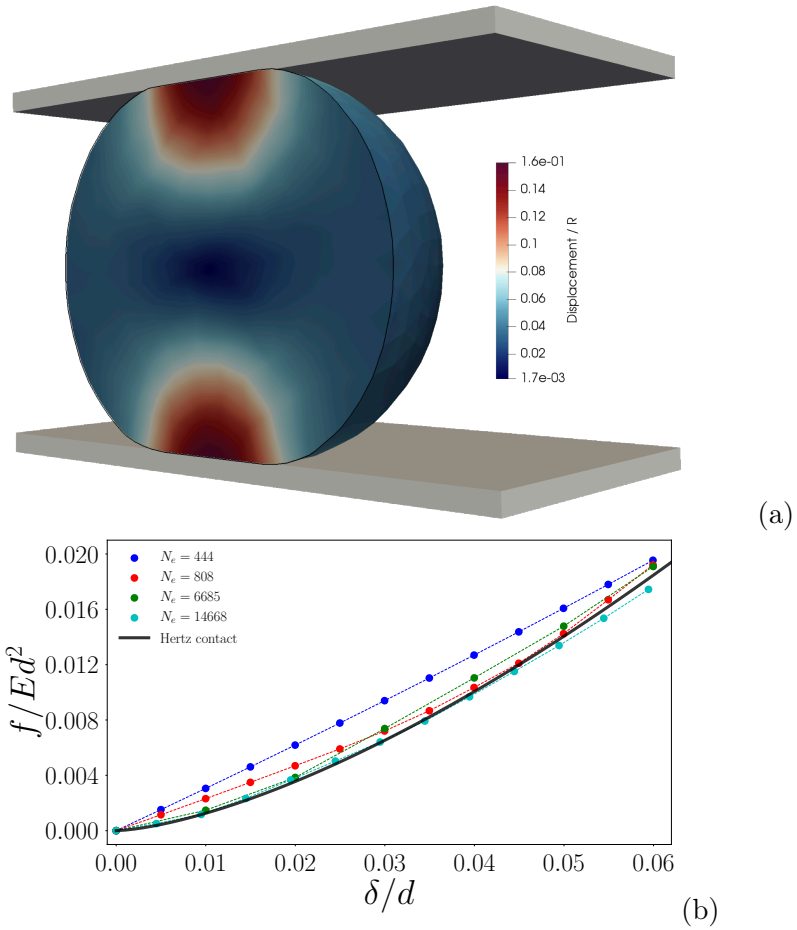

FIGURE 5.1. (a) A 3D cross-section of the vertical compression of an elastic spherical particle between two walls. Color intensity is proportional to the mean displacement field. (b) Normal contact force applied on a single spherical particle as a function of the deformation for different meshes. The continuous black line is the approximation given by the Hertz law Eq. (5.1).

Thus, in this study, we consider in total 8 systems, 4 systems composed of $N = 50$ and 4 systems composed of $N = 100$ elastic spheres all with a constant Poisson's ratio equals to 0.495 and a Young modulus E. The systems are constructed with geometrically independent initial conditions. The particles are first randomly deposited in a cubic box with a small particle size polydispersity around their mean diameter $\langle d \rangle$ in order to avoid crystallization ($d \in [0.8 \langle d \rangle , 1.2 \langle d \rangle]$). All packings are then isotropically compressed under a small stress σ_0, such that $\sigma_0 / E << 1$ (i.e. the particles can be considered as rigid, in comparaison to the applied stress). This initial compression ends when the change of the packing fraction ϕ is below 0.01%; after that, all systems can be considered as being in the jammed state, characterized by the initial packing fraction ϕ_0. At this point, the box size is $L_0 \times L_0 \times L_0$

Then, all packings are again isotropically compressed by imposing a constant velocity v on the box's boundaries. The velocity v is carefully chosen to ensure that all systems are always in the quasi-static regime, characterized by an inertial number $I << 1$. In our simulations, we use a constant friction coefficient between particles $\mu = 0.3$, and we keep the friction coefficient with the walls equal to zero. The gravity is also set to zero. Figure 5.2 presents the view of an assembly composed of 100 particles both at the jammed state ($\phi \sim 0.49$) and close to the maximal dense state with $\phi \sim 0.96$. In the following, the mean behavior for systems composed of $N_p = 50$ and $N_p = 100$ particles is obtained by averaging over the 4 corresponding independent sets. The averaged jammed packing fraction ϕ_0 obtained is 0.5 for 50 particle assemblies and 0.51 for 100 particle assemblies.

5.2 Results

5.2.1 Packing compaction and particle connectivity

This section analyzes the compactness of the assemblies, characterized by the evolution of the packing fraction ϕ as a function of the mean confining stress P and the mean particle connectivity Z. As in the previous numerical chapters, the mean confining stress, in the granular system, is extracted from the granular stress tensor $\boldsymbol{\sigma}$, which is computed at each

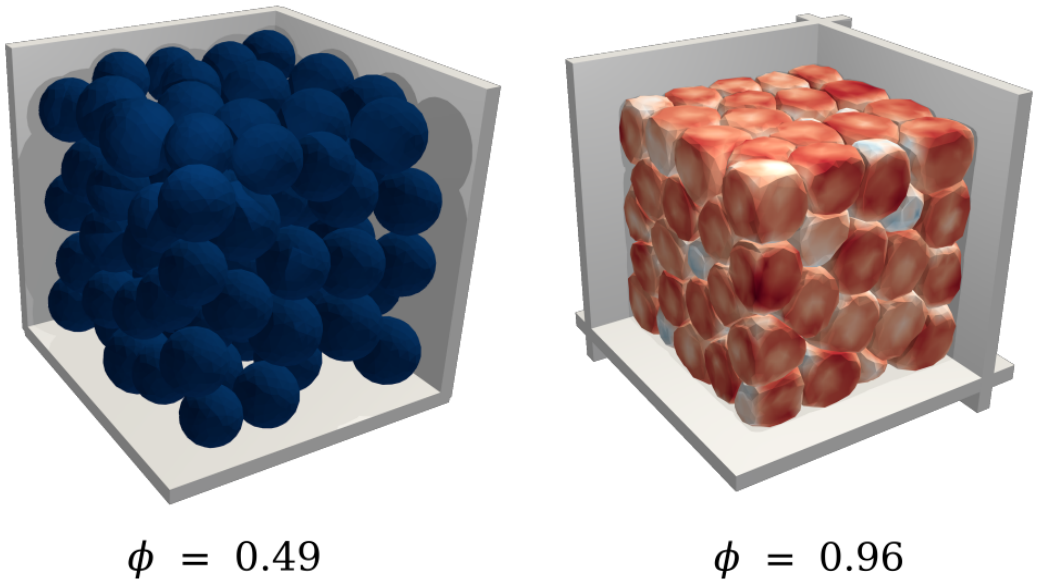

FIGURE 5.2. View of a granular assembly composed of 100 soft spherical particles at (a) the initial configuration and (b) close to $\phi = 0.96$. The color intensity, from blue to red, is related to the mean stress on each node.

step of the compression as [59]:

$$\sigma_{\alpha\beta} = \frac{1}{V} \sum_{c \in V} f_\alpha^c \ell_\beta^c, \tag{5.2}$$

where α and β correspond to x, y or z, f_α^c is the component α of the contact force at the contact c, and ℓ_β^c is the β component of the vector that join the two centers of the particles interacting at the contact c. Note that the total contact force between two deformable particles is computed as the vectorial sum of the forces at the contact nodes along the shared interface. The mean confining stress is then given by $P = (\sigma_1 + \sigma_2 + \sigma_3)/3$, where σ_1, σ_2 and σ_3 are the principal stress values of $\boldsymbol{\sigma}$. The packing fraction ϕ is also related to the macroscopic deformation ε, by $\varepsilon = -\ln(\phi_0/\phi)$.

Figure 5.3(a) shows the evolution of ϕ as a function of the mean confining stress P, normalized by the reduced Young Modulus $E^* = E/2(1-\nu^2)$, for the assemblies composed of 50 and 100 particles. From the jammed state, the packing fraction follows a monotonic increase, with a first rapid increase at low pressure, followed by a slowdown toward an asymptotic value of ϕ_{max}, at high pressure. As previously shown in 2D, the maximal packing fraction depends mainly on the friction coefficient and also on the shape of particles [80, 156, 182]. It is also interesting to note that the compaction curves for the 50 and 100 particle systems collapse on the same curve, which is in line with the previously cited work

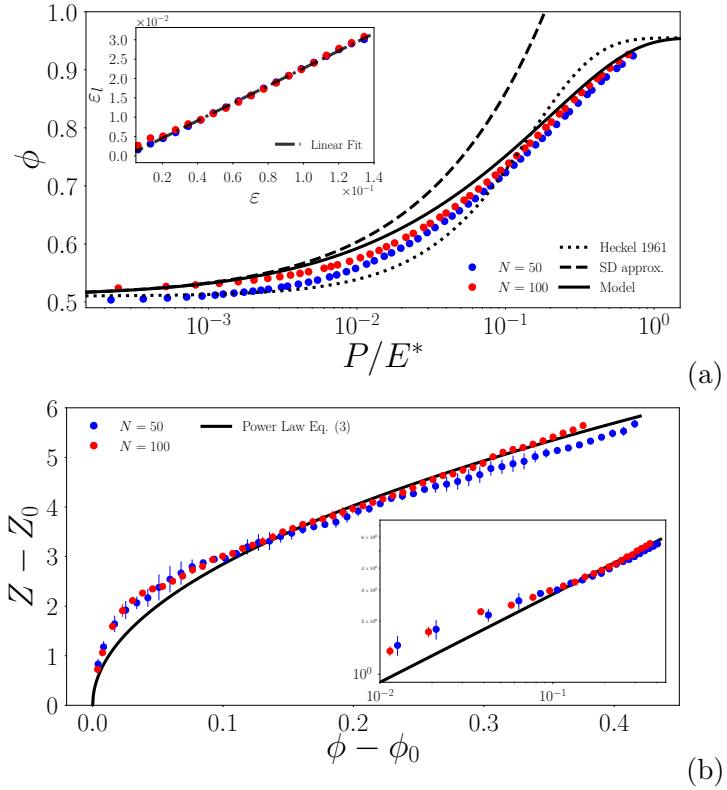

FIGURE 5.3. (a) Packing fraction ϕ as a function of the mean confining stress P normalized by the reduced Young Modulus E^*. The dotted line is the approximation given by the Heckel equation Eq. (5.3), the dashed line is the small strain approximation given by Eq. (5.6), and the continuous black line is the prediction given by our micromechanical approach Eq. (5.7). The inset shows the macroscopic volumetric strain ε as a function of the mean contact strain $\langle \varepsilon_\ell \rangle$ at the small deformation domain. (b) Reduced coordination number $Z - Z_0$ as a function of the reduced solid fraction $\phi - \phi_0$ (its log-log graph is shown in the inset). The continuous black line is the power-law relation given by Eq. (5.4) with exponent 0.5. Error bars represent the standard deviation on the averaged behavior performed over 4 independent samples.

mentioning the minimum number of grains necessary to capture the average behavior. On these compaction curves, we also show the approximation proposed by Heckel-Secondi, with the following form [11, 89]:

$$\frac{P}{E^*} = -A \ln\left(\frac{\phi_{max} - \phi}{\phi_{max} - \phi_0}\right), \tag{5.3}$$

with A a fitting constant equal to 0.15 in our case, and $\phi_{max} = 0.965$.

In Fig.5.3(b), we plot the evolution of the mean particle connectivity Z as a function of ϕ. At the jammed state, the packing structure is characterized by a minimal value Z_0, which depends on the coefficient of friction, the packing preparation, and the shape of the particles [51, 166, 195]. For spherical assemblies, Z_0 is equal to 6 if the friction is

set to 0, and it varies between 4 and 6, otherwise. In our two frictional systems, we get that $Z_0 \simeq 3.5$. Beyond the jammed state, Z continues to increase and, as is shown in the previous Chapters as well as in 2D numerical [80, 156, 182] and experimental [35, 79, 164] studies, the increases of Z follows a power law:

$$(Z - Z_0) = \psi\sqrt{\phi - \phi_0}, \tag{5.4}$$

with $\psi \approx 8.5$, a constant fully determine through the characteristics of both, the jammed state and the final dense state as $\psi = (Z_{max} - Z_0)/\sqrt{\phi_{max} - \phi_0}$, with Z_{max} the maximum packing fraction as $\phi \to \phi_{max}$. Thus, we extend to 3D soft particle assemblies this power-law relation.

5.2.2 A 3D compaction equation

We briefly recall the general framework introduced in **Chapter 2** and **3** allowing us to relate the packing fraction to the applied stress through the micromechanical specificity of a given system. We then apply this general framework to the case of three-dimensional soft spherical particles. The stress tensor Eq. (5.2) can be rewritten, as a sum over all contacts, as $\sigma_{\alpha\beta} = n_c\langle f^c_\alpha \ell^c_\beta\rangle_c$, where $\langle ...\rangle_c$ is the average over all contacts, and the density of contacts n_c is given by $n_c = N_c/V$, with N_c the total number of contacts in the volume V. Considering a small particle size distribution around the diameter $\langle d\rangle$, $\sum_{p\in V} V_p \simeq N_p V_p$, with $V_p = (\pi/6)d^3$, the contact density can be rewritten as $n_c \simeq 3Z\phi/(\pi d^3)$, with $Z = 2N_c/N_p$. From the definition of P via the principal stresses of σ, we get [106, 117, 163, 188]:

$$P \simeq \frac{\phi Z}{\pi}\sigma_\ell, \tag{5.5}$$

with $\sigma_\ell = \langle f^c \cdot \ell^c\rangle_c/\langle d\rangle^3$, a measure of the mean contact stress.

First, we focus on the small deformation domain. We can rely on Hertz's prediction where, in 3D, the force f^c at a contact c between two touching particles is related to the contact deflection δ^c by $f^c = (2/3)E^* d^{1/2}\delta^{c3/2}$. Then, since $\ell_c \sim d$ in the range of small deformation domains, we get $\sigma_\ell \sim (2/3)E^*\langle\varepsilon_\ell\rangle^{3/2}$, where $\varepsilon_\ell = \delta^c/d$ the deformation at a contact c, and assuming that $\langle\varepsilon_\ell^{3/2}\rangle \sim \langle\varepsilon_\ell\rangle^{3/2}$ which is well verified in our weakly polydisperse systems. Also, with a good approximation, we get that $Z = Z_0$. Finally, for random packings and at small deformation, simulations show that the mean contact

strain $\langle\varepsilon_\ell\rangle$ and the macroscopic volumetric strain are linearly dependent as $\langle\varepsilon_\ell\rangle \sim (1/\Gamma)\varepsilon$, with $\Gamma \sim 4.4$ (see inset in Fig.5.3(a)). This value is close to the one obtained in 2D with disks and non-circular particles **Section 3.4**. Note that $\Gamma = 3$ in the ideal case of a cubic lattice arrangement of spheres. Finally, by considering all these ingredients, Eq. (5.5) is re-written as:

$$\frac{P_{SD}}{E^*} = -\frac{2}{3\pi\Gamma^{3/2}} Z_0 \phi \ln^{(3/2)}\left(\frac{\phi_0}{\phi}\right), \tag{5.6}$$

with P_{SD} the limit of $P(\phi)$ at small deformations. The prediction given by Eq. (5.6) is shown in Fig. 5.3. As expected, we see a fair approximation of the compaction evolution in the small-strain domain, but Eq. (5.6) fails to predict the evolution at large strain.

The critical issue for the large strain domain is to find a proper functional approximation of $\sigma_\ell(\phi)$. In this case, the idea consists of combining the previous microscopic approach with a macroscopic development, in particular, the one of Carroll and Kim [90, 196]. By assuming that the compaction behavior can be equivalent to the collapse of a cavity within the elastic medium, they show that $P \propto \ln[(\phi_{max}-\phi)/(\phi_{max}-\phi_0)]$. Using this macroscopic approximation together with the micromechanical expression of P given by Eq. (5.5), and remarking that the quantity $Z\phi$ is finite, it is easy to show that, necessarily, $\sigma_\ell = \alpha(\phi)\ln[(\phi_{max}-\phi)/(\phi_{max}-\phi_0)]$, with α a function that depends, *a priori*, on ϕ. Then, by i) introducing the above form of σ_ℓ into Eq. (5.5), ii) ensuring the continuity to low deformation (i.e., $P \to P_{SD}$ for $\phi \to \phi_0$), and iii) introducing also the $Z-\phi$ relation (Eq. (5.4)) into Eq. (5.5), we get:

$$\frac{P}{E^*} = -\frac{2}{3\pi\Gamma^{3/2}}\left(\frac{\phi_{max}-\phi_0}{\phi_0^{3/2}}\right)\phi\sqrt{\phi-\phi_0}\left[Z_0 - \psi\sqrt{\phi-\phi_0}\right]\ln\left(\frac{\phi_{max}-\phi}{\phi_{max}-\phi_0}\right). \tag{5.7}$$

The compaction equation given by Eq. (5.7) is ploted with a black solid line in Fig. 5.3(a) together with our numerical data. As it can be seen, the prediction well-captures the asymptote close to the jammed state and the asymptote at high pressures. Equation (5.7), in contrast to previous models, has only one unknown parameter, the maximum packing fraction ϕ_{max}, since all other constants are entirely determined through the initial jammed state and the mapping between the packing fraction and coordination curve.

Finally, we would like to point out the differences between Eq. (5.7) and its two-dimensional equivalent Eq. (3.7) in **section 3.4**. In two dimensions, the numerical simulations show that σ_ℓ depends linearly on the mean contact strain (consistently with the

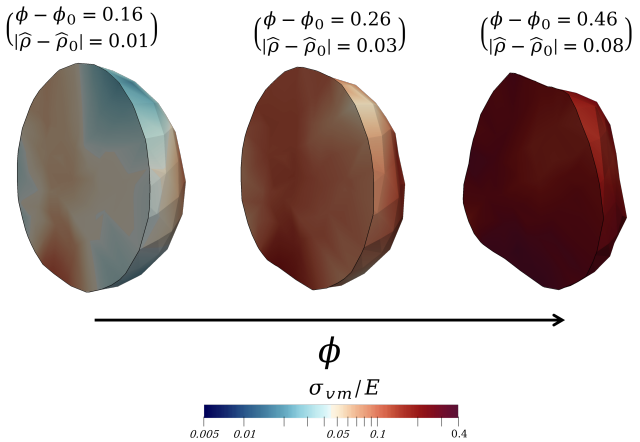

FIGURE 5.4. Shape evolution of a particle during the compaction extracted from the center of the packing. The color intensity is proportional to the von Mises stress scale by the Young modulus, σ_{vm}/E.

approximation classically used in 2D MD-like simulations [109]). This linear dependence in 2D then simplifies the development by replacing the terms $(2\sqrt{\phi - \phi_0})/(3\Gamma\phi_0)^{3/2})$ in the Eq. (5.7) to only $1/(\Gamma\phi_0)$. Thus, this work provides a clear example that, although the rheology of granular media (in general terms) is not specifically sensitive to space dimension, the detail of the structural and mechanical organization, in a perspective of predictive modeling, can only be appreciated in a 3D geometry.

5.2.3 Shape Parameter

To characterize the shape of the spherical particles during the compaction evolution, we use the sphericity parameter $\hat{\rho}$

$$\hat{\rho} = \left\langle \pi^{1/3} \frac{(6V_i)^{2/3}}{a_i} \right\rangle_i , \tag{5.8}$$

with a_i the surface area of the particle and $\langle ... \rangle_i$ the average over the particles in the volume V. Thus, by definition, the sphericity of a sphere is one, with values below one for any other geometry. The shape of a particle extracted from the center of the packing in different stages of the compaction is presented in Fig. 5.4.

In Fig. 5.5 we plot the evolution of $(\hat{\rho} - \hat{\rho}_0)$, with $\hat{\rho}_0$ the initial sphericity of the particles (~ 1, depending on the number of finite elements that discretize the particle) as a function of the excess packing fraction, $\phi - \phi_0$. Remarkably, the shape parameter of compressed soft spheres follows the same power-law tendency observe for the shape

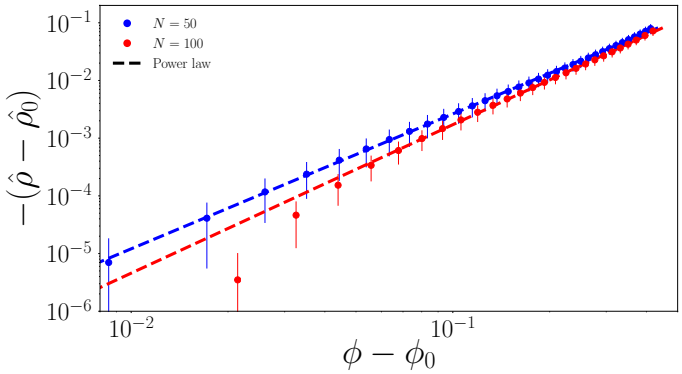

FIGURE 5.5. Evolution of the excess sphericity, $\hat{\rho} - \hat{\rho}_0$ as a function of the excess packing fraction $\phi - \phi_0$ for the isotropic compaction of soft spheres. The dashed line is the power-law relation given by Eq. (5.9).

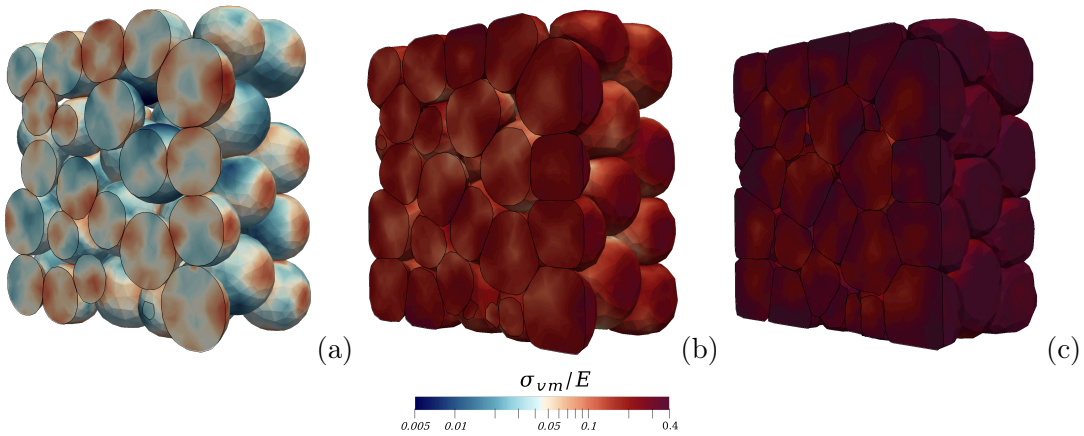

FIGURE 5.6. Three dimensional cross-section of the stress P_n at each node of the particles and for different packing fraction $\phi = 0.66$ (a), $\phi = 0.86$ (b) and $\phi = 0.96$ (c), respectively, in the assembly of 100 particles. The color intensity is proportional to the von Mises stress scale by the Young modulus, σ_{vm}/E.

parameter of compressed disks (see **Section 2.3.3**),

$$(\hat{\rho} - \hat{\rho}_0) = A(\phi - \phi_0)^{\beta}, \tag{5.9}$$

with $\beta \approx 2.5$ and $A \approx 0.6$. What is even more surprising is that the exponent of this power law is very similar to the exponent in two dimensions, which somehow shows a universal geometrical characteristic of the compaction of rounded soft particles.

5.2.4 Particle stress distribution

In this section, we focus on the stress distribution evolution within the particles during the compression. Let us consider the Cauchy stress tensor $\boldsymbol{\sigma}^C$ calculated inside the grains.

Note that $\boldsymbol{\sigma}^C$ have not to be confused with the granular stress tensor $\boldsymbol{\sigma}$ defined above and calculated from the contact forces. Figure 5.6 shows a cross-section images of an assembly of 100 particles, where the color scale represents the von Mises stress computed at each node. After the jammed state, strong heterogeneities in the stress distribution inside the particles can be seen (see Fig.5.6(a)). The grains are mainly deformed at the contact points, which generally support the maximum stress. Far beyond the jammed state (Fig.5.6(b,c)), the shape of the grains strongly changes, the size of the pore declines, and the spatial stress distributions tend to homogenize.

Fig. 5.7 shows the evolution of the probability density functions (PDF) for the equivalent von Mises stress σ_{vm}. Close to the jammed state, we observe exponential decays, as reminiscent of the distribution of contact forces classically observed in rigid particle assemblies [52,60,63,139], underlining that, although the assembly is isotropically compressed at the macroscopic scale, the particles may undergo large shear stress. As the packing fraction increases, the PDFs get narrower and gradually transform into Gaussian-like distributions centered around their mean value.

From these observations, and consistently to the previous observations made in the two dimensions, a schematic picture emerges to describe the compaction from a local perspective. During the compaction, the assembly shifts from a rigid granular material to a continuous-like material. In the granular-material state, the voids are filled by affine displacement of the particles and small deformations that do not change the spherical shape of the particles significantly. Then, due to the increasing average contact surface and the mean coordination number, stress and contact force homogenization within the packing occurs. This progressive shift of the distributions to Gaussian-like distributions evidence that the system is reaching a more continuous-like material as the packing fraction approaches its maximum value. This is verified by the decreasing standard deviation of such distributions (inset in Fig. 5.7(b)).

5.3 Conclusions

In this chapter, we investigated the compaction behavior of three-dimensional soft spherical particle assemblies through the Non-Smooth Contact Dynamic Method. From the jammed state to packing fraction close to 1, various packings composed of 50 and 100

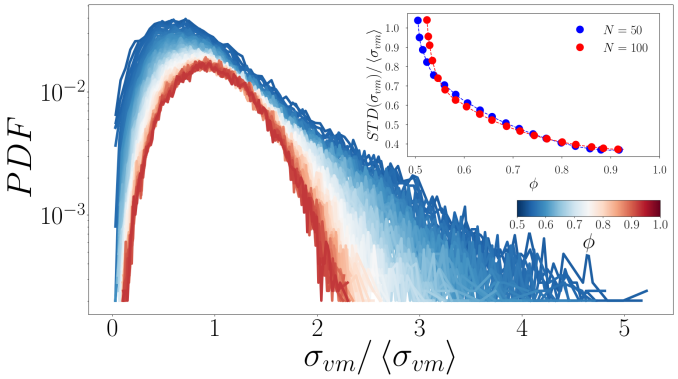

FIGURE 5.7. Probability density function (pdf) of the local von Mises stress σ_{vm} computed at each node and normalized by the corresponding mean in one of the systems composed of 100 particles. The inset shows the standard deviation of the distribution of σ_{vm} as a function of the packing fraction ϕ for 50 and 100 particles assemblies (averaged over the four independent systems).

meshed spherical particles were isotropically compressed by applying a constant velocity on the boundaries. One of the main results of this work is the extension of the compaction model developed in the previous chapters to the compaction of 3D soft spherical particle assemblies based on micromechanical considerations and entirely determined from the structural properties of the packing. Moreover, we also show that the power-law relation between the coordination number and the packing fraction, after the jamming, is still valid in three-dimensional compaction of elastic spheres, the same as the power-law relation between the packing fraction and the shape parameter for disks and spheres.

Further, we show that the stress distribution within the particles becomes more homogenous as the packing fraction increases. Close to the jammed state, the probability density functions of von Mises stress decrease exponentially as the maximum stress increases, and progressively shift into a Gaussian-like shape at high packing fractions, which means that the system reaches a more continuous material.

Although the compaction curves in two and three dimensions appear to be similar in their overall shape, it is interesting to note that the equation describing the variation of P with ϕ established with the same micromechanical framework depends on the dimensionality. This dependence on the dimension has its origin in the functional form of the contact law at the small deformation domain. Thus, for pursuing a more general compaction equation, it is possible to apply the same micromechanical framework described in this work to assemblies of grains whose particles have more complex behaviors, such as plastic, elastoplastic, or visco-elastoplastic particles, and also to polydisperse systems. It

will be enough to identify the force law between two particles and then integrate it into the framework presented here for all these cases.

Finally, we would like to point out that, from our best knowledge, this is the first work in which the Non-Smooth Contact Dynamics approach is applied to the compaction of three-dimensional assembly of soft particles. Nevertheless, many efforts still need to be made on numerical optimization and parallelization of resolution algorithms to increase performance. In particular, it would be interesting to consider periodic conditions in 3D, at least in two directions.

Conclusions and perspectives

In Nature, granular matter is composed of grains very diverse in terms of shape, size, and bulk properties. However, most of the time, they are studied in the simplified framework of disks and in the small deformation regime. In this work, we are interested in the compaction behavior of granular material made of soft particles, mixtures of soft/rigid particles, and soft non-circular particles, all of them being driven well beyond the jammed state up-to high levels of deformations. This rheological study is performed numerically on two- and three-dimensional systems, using the non-smooth contact dynamics (NSCD) and experimentally using quasi-bidimensional systems of soft and rigid cylinders together with high-resolution images and new image correlation methods.

First, we studied the effect of the particle Young modulus dispersity on the evolution of the packing's main structural and mechanical parameters during the compaction. Second, the effect of the initial particle shape has been discussed by comparing the arrangements of pentagons with the arrangements of soft circular particles with increasing local friction. Third, the uniaxial compaction of mixtures of soft/rigid cylinders with parallel axes has been experimentally investigated. Finally, the effect of the space dimensionality on the compaction behavior has been numerically investigated using soft spherical particles.

As a general finding, we showed that the maximum value of the packing fraction achieved by the systems does not strongly depend on the shape of the particles but highly depends on the friction coefficient and the soft/rigid mixture ratio. In the frictional case, ϕ_{max} decreases proportionally to the friction coefficient with a seemingly saturation for values higher than $\mu = 0.2$. The decrease of the particle rearrangement explains this: as

the rearrangement in the system is low, the deformed particles cannot reach void spaces by simple deformation, making the maximal packing fraction decreasing. For mixtures, it is observed that the dependence of ϕ_{max} is inversely proportional to the relation of soft particles in the assembly.

Empirical laws describing different microscopic quantities of the assembly are corroborated, and new others are found. For the systems studied, it is observed that the power-law relation between the coordination number and the packing fraction is conserved, keeping the same value of the exponent. On the other hand, it is found that the average contact length evolves linearly with the packing fraction, with a scale factor that does not strongly depend on the friction or the particle shape but depends quasi-linearly on the mixture of solid and rigid particles. For circular and spherical particles, it is also found that their shape parameter (circularity and sphericity, respectively) also follows a power-law with the packing fraction, the exponents being similar.

A major outcome of this work is the development of a theoretical and micro-mechanical-based approach for the compaction of soft granular assemblies far beyond the jamming point. This model is derived from the micromechanical expression of the granular stress tensor, its limit to small and elastic deformation, and the evolution of the connectivity. From the expression of these well-defined quantities, we establish a compaction and bulk equations, free of any ad hoc parameters, well-fitting our numerical and experimental data. The only unknown parameter appearing in our equations is the maximum packing fraction value. This approach results in different compaction equations that functionally depend on dimensionality, where the characteristics of shape and elastic bi-dispersity are considered only as input parameters in the model.

The theoretical framework presented allows us to unify the compaction behavior of assemblies of soft, soft/rigid, noncircular soft particles coherently, beyond the jamming point, both in 2D and in 3D, both for isotropic and uniaxial compression. The above framework may now be used and extended to analyze much more complex deformable granular assemblies by considering a wide range of material properties, such as plastic, elastoplastic, or visco-elastoplastic particles, other noncircular/spherical particles, and polydisperse packings in size. Other loading configurations could be investigated in this framework as well. These alternative mechanical considerations may lead to distinct functional forms for the compaction equation but settled on the same micro-mechanical arguments.

Another aspect that we would also like to point out is that (from our very best knowledge) this is the first time that the Non-Smooth Contact Dynamics Method is applied to the compaction of deformable grains assembly in 3D. Therefore, the work presented in the last chapter confirms the capabilities of this numerical method for modeling not just rigid assemblies (commonly used for) but also for soft grain assemblies in 3D.

In this work, two different types of compaction were studied, isotropic compaction and uniaxial compaction. A logical research direction is to study the effect of other types of loading conditions on the assemblies, such as shear loadings or combined compression and shear laodings, which are widely used in several applications. A necessary forward step is also to observe whether the different empirical laws evidenced in this work, along with the stated hypotheses, are still conserved under different types of loading, and perhaps constitute universal laws for the rheology of soft granular media. Another possible direction of research is to study deformable granular assemblies with different polydispersity, a high level of concavity in shape and even maybe fragmentable. This would be more, representative of the reality of this type of material in a closer way.

From a numerical point of view, it is necessary to study the Non-Smooth Contact Dynamics method in more details. This in order to to find computationally more efficient algorithms to solve the different particles interactions and the possible addition of new material constitutive laws. But from an experimental point of view the challenge is even larger. In 2D, simulations have been done with different particles shapes and on larger systems. Experiments should be done with different other particle shapes and maybe hollow ones. The experimental set-up should also be improved to treat systems with more particles, with different rheologies and frictionnal properties, and loaded with more complex geometries. Finally, a last logical step is to scale the methods used here to three-dimensional systems, allowing thus the study of more common systems in nature and increasing the possibility to be confronted to many exciting phenomena.

Résumé étendu en français

Ce chapitre présente un résumé étendu en Français du manuscript de thèse. Nous y présentons la problématique générale de la compaction des assemblages de grains mous et à composition complexe. Nous présentons ensuite de maniére chronologique le détail de chaque chapitre. Nous terminons par une conclusion sur les résultats les plus importants obtenus durant ces 3 années de thèse et nous dessinons plusieurs perspectives à ce travail.

Introduction

Le comportement mécanique des systèmes granulaires est régi par le comportement mécanique individuel de chacune des particules qui les composent. Par exemple, lorsque des particules dures (c'est-à-dire ayant une rigidité élevée par rapport à la contrainte appliquée) sont comprimées à l'intérieur d'une boîte, elles ont tendance à se réarranger de manière plus compacte. La compression prend fin lorsqu'un réseau de forces permanent est atteint. Cet état, également appelé état de blocage (ou "Jamming state" en anglais), dépend principalement de la morphologie des particules (c'est-à-dire de leur taille et de leur forme), du frottement inter-grain et de la loi d'interaction entre les particules. Maintenant, si l'on considère des assemblages de particules molles, lorsque la contrainte appliquée devient significative, les particules subissent de grandes déformations. La compression se poursuit au-delà de l'état de blocage, principalement en raison du changement de forme des particules et, dans une moindre mesure, en raison de leurs réarrangements (rendu possible par leur deformation individuelle). La compacité ϕ (c'est-à-dire le rapport entre le volume des particules et le volume de la boîte) dépasse alors la compacité de l'état de blocage

ϕ_0, et tend vers des valeurs proches de 1 avec un nombre croissant de contacts et une augmentation de la taille des surfaces de contact.

Parmi ces matériaux mous ou deformables, nous trouvons les tissus biologiques composés de cellules molles, les mousses, les suspensions, les matériaux argileux et tout matériau fritté comme les céramiques, les poudres métalliques ou les pilules pharmaceutiques, pour n'en citer que quelques-uns. Dans un contexte génie civil, des questions émergentes récentes ont conduit à la conception de nouveaux matériaux sous la forme de mélange de particules du sol avec des morceaux de caoutchouc (fabriqués à partir de pneus usagés). Ces matériaux composites présentent des propriétés mécaniques nouvelles et fascinantes, telles qu'une meilleure relaxation des contraintes, une meilleure isolation sismique et un meilleur amortissement des fondations, tout en réduisant le poids des structures ou en augmentant la fraction de remplissage des composites granulaires. La gamme d'application des composites rigides-déformables est potentiellement large et ouvre la porte à un champ extensif de sujets fondamentaux encore peu étudiés.

Trés recemment, des expériences innovantes et des méthodes numériques avancées (y compris les méthodes par éléments discrets, les approches sans maillages, et les méthodes couplant les approches éléments finis et discrets) ont permis de faire un pas en avant dans la compréhension de l'évolution microstructurale au-delà du point de blocage. Cependant, une modélisation théorique du processus de compaction fait toujours défaut. En effet, au cours des dernières décennies, un grand nombre d'équations de compactage ont été proposées, mais la plupart d'entre elles ont peu de fondements physiques ou micromécaniques très clairs. En général, tous les modèles existants sont basés sur des hypothèses macroscopiques, et donc plusieurs paramètres d'ajustement sont nécessaires pour faire correspondre chaque expression aux données numériques ou expérimentales. De même, les mécanismes qui conduisent à la transition d'un milieu à structure granulaires vers à un milieu à structure continue sont aussi très mal décrits.

Dans ce travail de thèse, au moyen de simulations numériques et d'expériences modèles, nous analysons la compaction de grains frottants hautement déformables, de différentes formes, ou encore des mélanges de grains déformable/rigide en deux et trois dimensions. Numériquement, nous utilisons la méthode de dynamique des contacts non régulière ("Non-Smooth Contact Dynamics", NSCD) couplant la méthode de Dynamique des Contacts (pour gérer le contact entre grains) à la méthode des Eléments Finis (pour

la déformation de la matière constituant les grains). Expérimentalement, nous utilisons des techniques d'imagerie à très haute résolution couplées à des algorithmes de corrélation d'image numérique ("Digital Image correlation", en angalis, DIC) sur un système de grains quasi-2D sollicités en compression unixialle.

Compaction 2D de mélanges de grains mous et rigides

Dans ce chapitre, nous analysons la compaction isotrope de mélanges composés de particules incompressibles rigides et déformables par l'approche de la dynamique de contact non régulière (NSCD). Les particules déformables sont simulées en utilisant une loi constitutive néo-hookéenne hyper-élastique au moyen d'éléments finis classiques. Pour des mélanges allant d'assemblages de particules exclusivement rigides à exclusivement déformables (voir Fig. R.1), nous caractérisons l'évolution de la compacité, du module d'élasticité et de la microstructure (connectivité, distribution des efforts...) en fonction des contraintes appliquées et pour différentes valeurs du coefficient de frottement inter-granulaire.

Nous montrons d'abord que la compacité augmente et tend asymptotiquement vers une valeur maximale ϕ_{max}, qui dépend à la fois du rapport de mélange et du frottement inter-granulaire. Nous montrons également que le module élastique apparent augmente avec la compacité et diverge à mesure qu'il s'approche de ϕ_{max}. Puis, nous observons que la coordination moyenne des particules ou encore que l'exentricité moyenne des particules varient en loi de puissance avec la compacité. Pour le nombre de coordination, les exposants de la relation de puissance et le paramètre d'échelle sont conservés pour différents rapports de mélange et pour différents coefficients de frottement. Pour le paramètre de forme, l'exposant varie légèrement avec le coefficient de frottement mais reste constant lorsque l'on fait varier le rapport de mélange. Une relation linéaire entre l'augmentation de longueur relative des contacts et la compacité est également observée, dont la pente dépend du rapport de mélange. Pour les différentes valeurs du rapport de mélange et de frottement, une distribution de plus en plus homogène des forces de contact apparaît lorsque la pression appliquée augmente.

A partir de l'expression micro-mécanique du tenseur des contraintes granulaires, nous développons un modèle pour décrire le comportement de la compaction en fonction de la pression appliquée, du module d'Young des particules déformables, et du rapport de

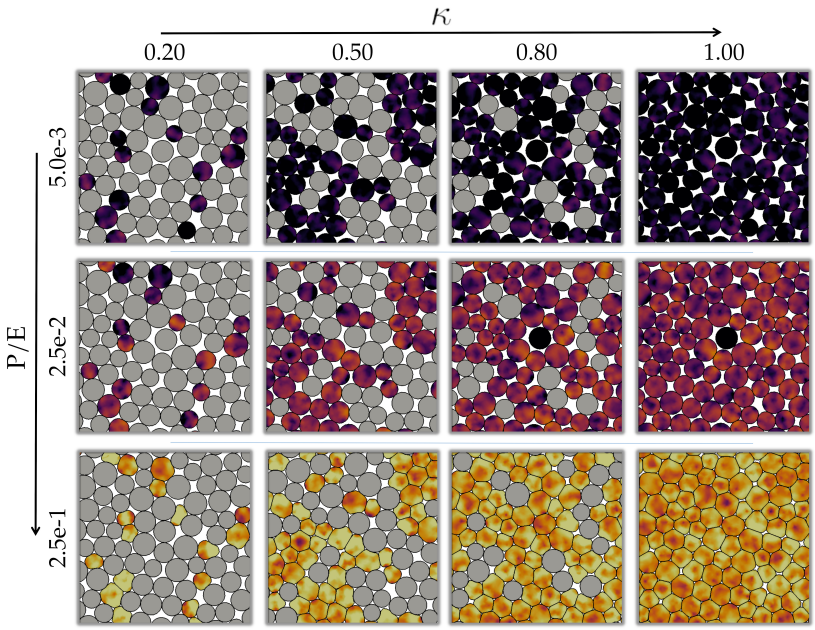

FIGURE R.1. Visualisation au coeur d'échantillons pour différents rapports de mélange κ et différentes valeurs de pression réduite P/E. Ici, le frottement entre grain est fixé à $0,2$. Les particules rigides sont représentées en gris et l'intensité de la couleur pour les particules déformables est proportionnelle à la déformation volumétrique des particules.

mélange. Une équation décrivant l'évolution du module élastique est également dérivée de l'équation de compaction. Ce modèle repose sur la caractérisation d'une seule particule déformable sous compression, ainsi que sur la relation en loi de puissance entre la connectivité et la compacité. Ce modèle de compaction, défini par des quantités physiques bien définies, donne lieu à de très bonnes prédictions de l'évolution de la compacité à partir du point de blocage jusqu'à de très hautes densités et nous permet de donner une prédiction directe de ϕ_{max} en fonction du rapport de mélange et du coefficient de friction.

Compaction 2D d'assemblages de pentagones déformables

Dans ce chapitre nous étudions la compaction d'assemblages de pentagones déformables au moyen de la methode NSCD. Afin de voir les effets de la forme des particules, nous avons également simulé des assemblages composés de particules circulaires molles (see Fig R.2). L'effet du frottement a été systématiquement étudié.

De manière générale, nous avons observé qu'au-delà du point de de blocage, les deux systèmes ont un comportement similaire. À l'échelle microscopique, premièrement, le réar-

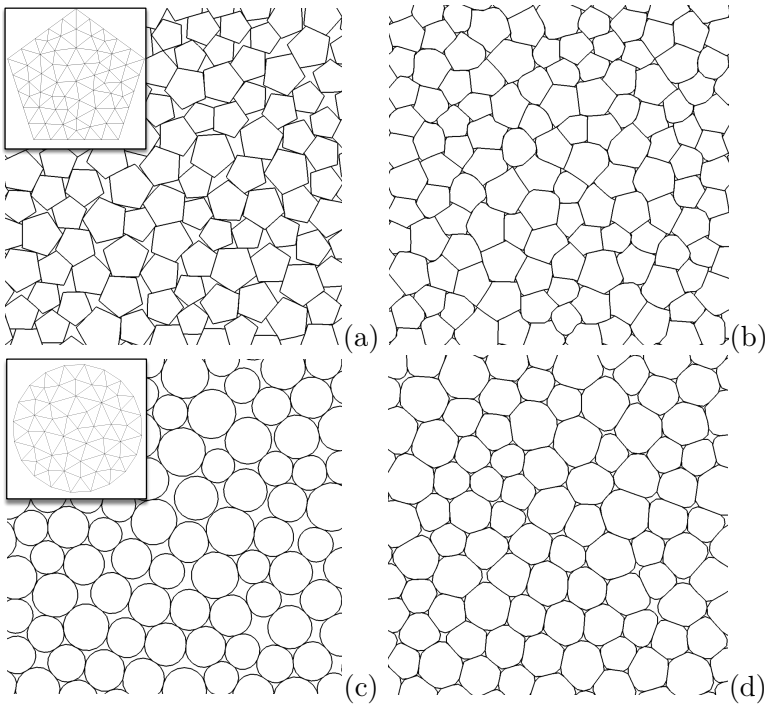

FIGURE R.2. Zoom dans des assemblages de pentagones (a,b) et de disques (c,d) mous pour $\mu = 0$ et pour $P/E = 0.025$ (a,c) et $P/E = 0.3$ (b,d). Les inserts des figures (a) et (c) montrent le maillage éléments finis utilisé respectivement pour les pentagones et les disques.

rangement des particules est toujours présent. Deuxièmement, la relation de puissance entre le nombre de coordination et la compacité est toujours valable pour les assemblages de pentagones mous. Troisièmement, les forces de contact et les distributions de contraintes des particules deviennent moins larges lorsque le niveau de compaction augmente. Les principales différences entre les deux systèmes proviennent de l'effet du frottement. La valeur de ϕ_{max} diminue lorsque le frottement augmente, mais elle diminue plus rapidement dans les assemblages de pentagones que dans les assemblages de disques. A l'échelle micro, le réarrangement des particules est plus élevé pour les pentagones mous, bien qu'il diminue lorsque le frottement inter-granulaire augmente. Il est intéressant de noter que le frottement entre particules contribue également à une meilleure homogénéisation du réseau de forces dans les deux systèmes.

L'équation de compaction établie précédemment pour les mélanges de disques déformables et rigides, est ainsi étendue aux assemblages de particules déformables et non circulaires. Un avantage de cette nouvelle approche par rapport à l'approche du chapitre précédent est qu'elle reproduit la même équation de compaction mais réduit le nombre de paramètres à un seul: la compacité maximale.

Compaction de mélanges de grains mous et rigides : une étude expérimentale

Dans ce chapitre, nous avons analysé expérimentalement la compaction uniaxiale d'assemblages granulaires composés de mélanges de particules cylindriques rigides et déformables (voir Fig. R.3). Ces particules sont posées sur un scanner photographique. Un très fin mouchetis est dessiné sur leur face inférieur et après chaque pas de chargement, l'évolution de ce dernier et imagé par le scanner. Un algorithme de corrélation d'images dédiés aux milieux granulaires et aux matériaux en grandes déformations mesure alors l'évolution du champs de déplacement dans chaque grain. Tous les observables locaux et globaux des milieux granulaires en sont alors déduits.

Tout d'abord, nous corroborons la tendance en loi de puissance pour le nombre de coordination en fonction de la compacité. L'exposant est toutefois legèrement surestimé en raison de la petite taille du système. Une relation en loi de puissance entre le paramètre de forme et la compacité est également observée. Ensuite, une relation linéaire entre la longueur de contact spécifique moyennée sur les particules et la compasité du système est observée, ce qui est en accord avec les chapitres précédents. Aussi, pour un petit niveau de déformation, la déformation moyenne à l'intérieur des particules molles évolue linéairement avec la compacité, alors que pour des niveaux de chargement élevés, elle évolue linéiarement avec la pression globale appliquée au systéme. Ceci met en évidence deux régimes distincts séparés par une valeur critique indépendante de κ. Enfin, ces résultats expérimentaux valident le modèle de compaction, ici développé dans le cas de la compaction uniaxiale d'un système quasi bidimensionnel.

Compaction 3D d'assemblages de sphères molles

Dans ce chapitre, nous avons étudié la compaction, au delà du point de blocage, d'assemblages tridimensionnels de particules sphériques molles par la méthode de dynamique des contacts non régulière (voir Fig. R.4). Nous montrons également que la relation en loi de puissance entre le nombre de coordination et la compacité est toujours valide dans le cas de la compaction 3D de sphères élastiques, tout comme la relation en loi de puissance entre la compacité et le paramètre de forme. En outre, nous montrons que

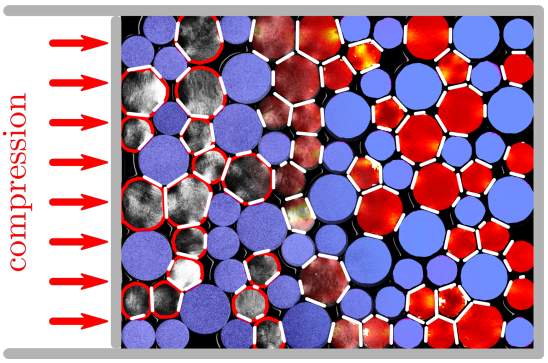

FIGURE R.3. Vue composée des champs mesurés. Les particules rigides sont teintées en bleu. L'image brute, en niveau de gris, est représentée en arrière plan à gauche et dans la Fig. 4.3(b), les frontières des particules sont désinées en rouge sur la gauche. La valeur au sens de von Mises du champ de déformation, $\mathcal{C}$, est représentés sur la droite avec une échelle de couleurs allant du rouge foncé (valeurs faibles) au jaune (valeurs élevées). Les contacts sont représentés en blanc.

la distribution des contraintes à l'intérieur des particules s'homogénéise lorsque la compacité augmente. Proche de l'état de blocage, les fonctions de densité de probabilité de la contrainte de von Mises diminuent exponentiellement lorsque la contrainte maximale augmente. Au fur et à mesure que la compacité augmente, les distributions prennent progressivement une forme gaussienne, ce qui signifie que le système atteint un état "plus continu".

Un premier résultat de ce chapitre est l'extension du modèle de compaction à la compaction d'assemblages de particules sphériques molles en 3D. Toutefois, bien que les courbes de compaction en deux et trois dimensions semblent être similaires dans leur forme générale, il est intéressant de noter que l'équation décrivant la variation de P avec ϕ établie dans le même cadre micromécanique dépend de la dimension du problème. Cette dépendance trouve son origine dans la forme fonctionnelle de la loi de contact dans le domaine des petites déformations.

Conclusions

Dans ce travail de thèse, nous nous sommes intéressés au comportement en compression de matériaux granulaires constitués de particules molles, de mélanges de particules molles/rigides et de particules molles non circulaires, bien au-delà de l'état de blocage. L'étude rhéologique a été réalisée numériquement dans des systèmes bi- et tridimensionnels, en utilisant la dynamique de contact non régulière (NSCD) et expérimentalement

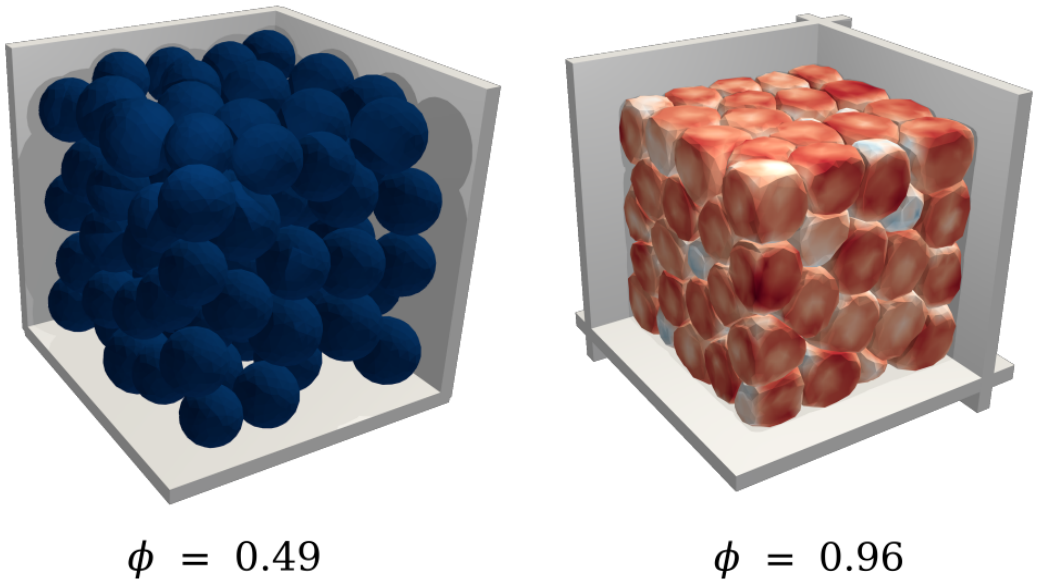

FIGURE R.4. Vue d'un assemblage granulaire composé de 100 particules sphériques molles dans (a) la configuration initiale et (b) proche de $\phi = 0.96$. L'intensité de la couleur, du bleu au rouge, est liée à la contrainte moyenne sur chaque nœud.

en utilisant des systèmes quasi-bidimensionnels constitués de mélange de cylindres souples/rigides et des techniques avancées basées sur une imagerie à haute résolution et de nouvelles méthodes de corrélation d'images.

De manière générale, nous avons montré que la valeur maximale de la compacité atteinte par les systèmes ne dépend pas fortement de la forme des particules mais dépend fortement du coefficient de frottement et du rapport de mélange deformable/rigide. Nous observons que, la compacité maximale ϕ_{max} diminue proportionnellement avec le coefficient de frottement et sature pour des valeurs supérieures à $\mu = 0.2$. Pour les mélanges, on observe que la dépendance de ϕ_{max} est inversement proportionnelle à la proportion de particules molles dans l'assemblage. Nous avons également constaté que la variantion en loi de puissance du nombre de coordination et de la compacité est conservée pour les systèmes étudiés. De plus, on constate que la longueur moyenne des contacts évolue linéairement avec la compacité, avec un facteur d'échelle ne dépendant pas fortement du frottement ou de la forme des particules. Au contraire, il dépend quasi-linéairement de la proportion de mélange de particules déformable/rigides. Pour les particules circulaires et sphériques, on constate également que leur paramètre de forme suit une loi de puissance avec la compacité.

Un résultat majeur de ce travail est le développement d'une approche théorique micromécanique pour la compaction d'assemblages granulaires mous bien au-delà du point de

blocage. Ce modèle est dérivé de l'expression micromécanique du tenseur des contraintes granulaires, de sa limite aux petites déformations élastiques et de l'évolution de la connectivité. À partir de l'expression de ces quantités, nous établissons différentes équations de compaction, libres de tout paramètres *ad hoc*, reproduisant parfaitement nos données numériques et expérimentales. Ces équations dépendent principalement de la dimensionnalité (2D/3D), et prennent en compte les caractéristiques de forme, de bi-dispersité élastique, ou de géométrie de compression (uniaxiale *vs* isotrope). Le cadre micromécanique proposé permet d'unifier le comportement de compactage des assemblages de particules molles, molles/rigides et non circulaires de manière cohérente, à la fois en 2D et en 3D, pour une compression isotrope et uniaxiale.

Le cadre micromecanique établi dans cette thèse peut maintenant être utilisé et étendu pour analyser des assemblages granulaires déformables beaucoup plus complexes en considérant une large gamme de propriétés matérielles, telles que des particules plastiques, élastoplastiques ou visco-élastoplastiques, d'autres particules circulaires/sphériques et des systèmes polydisperses en taille et forme. D'autres configurations de chargement pourraient également être étudiées dans ce cadre.

List of publications

M. Cárdenas-Barrantes, D. Cantor, J. Barés, M. Renouf, and E. Azéma, Compaction of mixtures of rigid and highly deformable particles: A micromechanical model, Physical Review E 102, 032904 (2020).

D. Cantor, **M. Cárdenas-Barrantes**, I. Preechawuttipong, M. Renouf, and E. Azéma, Compaction model for highly deformable particle assemblies, Physical Review Letters 124, 208003 (2020).

M. Cárdenas-Barrantes, D. Cantor, J. Barés, M. Renouf, and E. Azéma, Micromechanical description of the compaction of soft pentagon assemblies, Physical Review E 103, 062902 (2021).

Conference proceedings

M. Cárdenas-Barrantes, D. Cantor, J. Barés, M. Renouf, and E. Azéma, A micromechanical compaction model for granular mix of soft and rigid particles, EPJ Web Conferences 249, 02008 (2021).

J. Barés, **M. Cárdenas-Barrantes**, D. Cantor, M. Renouf, and E. Azéma, Highly strained mixtures of bidimensional soft and rigid grains: an experimental approach from

the local scale, EPJ Web Conferences 249, 05004 (2021).

D. Cantor, **M. Cárdenas-Barrantes**, J. Barés, M. Renouf, and E. Azéma, Bulk modulus of soft particle assemblies under compression, EPJ Web Conferences 249, 14014 (2021).

6

Bibliography

[1] Y. Forterre and O. Pouliquen, "Flows of dense granular media," *Annual Review of Fluid Mechanics*, vol. 40, no. 1, pp. 1–24, 2008.

[2] L. Atia, D. Bi, Y. Sharma, J. A. Mitchel, B. Gweon, S. A. Koehler, S. J. DeCamp, B. Lan, J. H. Kim, R. Hirsch, A. F. Pegoraro, K. H. Lee, J. R. Starr, D. A. Weitz, A. C. Martin, J.-A. Park, J. P. Butler, and J. J. Fredberg, "Geometric constraints during epithelial jamming," *Nature Physics*, vol. 14, pp. 613–620, Jun 2018.

[3] J. M. Montes, F. G. Cuevas, J. Cintas, Y. Torres, and E. Caballero, "On the compressibility of metal powders," *Powder Metallurgy*, vol. 61, no. 3, pp. 219–230, 2018.

[4] T. Zhang, G. Cai, S. Liu, and W. Duan, "Laboratory observation of engineering properties and deformation mechanisms of cemented rubber-sand mixtures," *Construction and Building Materials*, vol. 120, no. 3, pp. 514 – 523, 2016.

[5] L. E. Silbert, "Jamming of frictional spheres and random loose packing," *Soft Matter*, vol. 6, pp. 2918–2924, 2010.

[6] A. Donev, I. Cisse, D. Sachs, E. A. Variano, F. H. Stillinger, R. Connelly, S. Torquato, and P. M. Chaikin, "Improving the density of jammed disordered packings using ellipsoids," *Science*, vol. 303, no. 5660, pp. 990–993, 2004.

[7] R. P. Behringer, D. Bi, B. Chakraborty, A. Clark, J. Dijksman, J. Ren, and J. Zhang, "Statistical properties of granular materials near jamming," *Journal of Statistical Mechanics: Theory and Experiment*, vol. 2014, p. P06004, jun 2014.

[8] E. Azéma, F. Radjai, and G. Saussine, "Quasistatic rheology, force transmission and fabric properties of a packing of irregular polyhedral particles," *Mechanics of Materials*, vol. 41, pp. 729–741, June 2009.

[9] F. Radjai, "Modeling force transmission in granular materials," *Comptes Rendus Physique*, vol. 16, no. 1, pp. 3–9, 2015. Granular physics / Physique des milieux granulaires.

[10] E. Somfai, M. van Hecke, W. G. Ellenbroek, K. Shundyak, and W. van Saarloos, "Critical and noncritical jamming of frictional grains," *Phys. Rev. E*, vol. 75, p. 020301, Feb 2007.

[11] J. Secondi, "Modelling powder compaction: From a pressure-density law to continuum mechanics," *Powder Metallurgy*, vol. 45, no. 3, pp. 213–217, 2002.

[12] F. Huang, X. An, Y. Zhang, and A. B. Yu, "Multi-particle FEM simulation of 2D compaction on binary Al/SiC composite powders," *Powder Technology*, vol. 314, pp. 39–48, 2017.

[13] T.-L. Vu, S. Nezamabadi, and S. Mora, "Effects of particle compressibility on structural and mechanical properties of compressed soft granular materials," *Journal of the Mechanics and Physics of Solids*, vol. 146, p. 104201, 2021.

[14] M. Asadi, A. Mahboubi, and K. Thoeni, "Discrete modeling of sand-tire mixture considering grain-scale deformability," *Granular Matter*, vol. 20, 05 2018.

[15] R. Machaka and H. Chikwanda, "Analysis of the cold compaction behavior of titanium powders: A comprehensive inter-model comparison study of compaction equations," *Metallurgical and Materials Transactions A*, vol. 46, no. 9, pp. 4286–4297, 2015.

[16] A. Platzer, S. Rouhanifar, P. Richard, B. Cazacliu, and E. Ibraim, "Sand-rubber mixtures undergoing isotropic loading: derivation and experimental probing of a physical model," *Granular Matter*, vol. 20, no. 4, p. 81, 2018.

[17] G. Katgert, B. P. Tighe, and M. van Hecke, "The jamming perspective on wet foams," *Soft Matter*, vol. 9, pp. 9739–9746, 2013.

[18] H. P. Zhang and H. A. Makse, "Jamming transition in emulsions and granular materials," *Physical Review E*, vol. 72, p. 011301, Jul 2005.

[19] B. Harthong, J.-F. Jérier, V. Richefeu, B. Chareyre, P. Dorémus, D. Imbault, and F.-V. Donzé, "Contact impingement in packings of elastic-plastic spheres, application to powder compaction," *International Journal of Mechanical Sciences*, vol. 61, no. 1, pp. 32–43, 2012.

[20] T. L. Vu, *Milieux Granulaires á Particules Molles : Modélisation Expérimentale et Numériq*. PhD thesis, Ecole doctorale de Information, Structures, Systémes, Université De Montpellier, Montpellier, 11 2018.

[21] N. Abdelmoula, B. Harthong, D. Imbault, and P. Dorémus, "A study on the uniqueness of the plastic flow direction for granular assemblies of ductile particles using discrete finite-element simulations," *Journal of the Mechanics and Physics of Solids*, vol. 109, pp. 142–159, 2017.

[22] Z. Cheng, J. Wang, and W. Li, "The micro-mechanical behaviour of sand-rubber mixtures under shear: An experimental study based on x-ray micro-tomography," *Soils and Foundations*, vol. 60, no. 5, pp. 1251–1268, 2020.

[23] T.-l. Vu and J. Barés, "Soft-grain compression : Beyond the jamming point," *Physical Review E*, vol. 100, no. 4, p. 42907, 2019.

[24] Y. X. Zhang, X. Z. An, and Y. L. Zhang, "Multi-particle FEM modeling on microscopic behavior of 2D particle compaction," *Applied Physics A: Materials Science and Processing*, vol. 118, no. 3, pp. 1015–1021, 2014.

[25] B. Maurin, P. Cañadas, H. Baudriller, P. Montcourrier, and N. Bettache, "Mechanical model of cytoskeleton structuration during cell adhesion and spreading," *Journal of Biomechanics*, vol. 41, no. 9, pp. 2036 – 2041, 2008.

[26] W. R. Ketterhagen, "Modeling the motion and orientation of various pharmaceutical tablet shapes in a film coating pan using dem," *International Journal of Pharmaceutics*, vol. 409, no. 1, pp. 137–149, 2011.

[27] E. Azéma, P. Sánchez, and D. J. Scheeres, "Scaling behavior of cohesive self-gravitating aggregates," *Phys. Rev. E*, vol. 98, p. 030901, Sep 2018.

[28] A. J. Rogers, A. Hashemi, and M. G. Ierapetritou, "Modeling of particulate processes for the continuous manufacture of solid-based pharmaceutical dosage forms," *Processes*, vol. 1, no. 2, pp. 67–127, 2013.

[29] E. Clément, F. Malloggi, B. Andreotti, and I. S. Aranson, "Erosive granular avalanches: a cross confrontation between theory and experiment," *Granular Matter*, vol. 10, pp. 3–11, Dec 2007.

[30] R. A. Bagnold, "Experiments on a gravity-free dispersion of large solid spheres in a newtonian fluid under shear," *Proceedings of the Royal Society of London. Series A. Mathematical and Physical Sciences*, vol. 225, no. 1160, pp. 49–63, 1954.

[31] E. I. Corwin, H. M. Jaeger, and S. R. Nagel, "Structural signature of jamming in granular media," *Nature*, vol. 435, pp. 1075–1078, June 2005.

[32] J. A. Dijksman, N. Brodu, and R. P. Behringer, "Refractive Index Matched Scanning and Detection of Soft Particle," *Review of Scientific Instrument*, vol. 88, no. 5, p. 051807, 2017.

[33] R. Stannarius, D. Sancho Martinez, T. Finger, E. Somfai, and T. Börzsönyi, "Packing and flow profiles of soft grains in 3D silos reconstructed with X-ray computed tomography," *Granular Matter*, vol. 21, no. 3, p. 56, 2019.

[34] J. Barés, N. Brodu, H. Zheng, and J. A. Dijksman, "Transparent experiments: releasing data from mechanical tests on three dimensional hydrogel sphere packings," *Granular Matter*, vol. 22, no. 1, p. 21, 2020.

[35] G. Katgert and M. van Hecke, "Jamming and geometry of two-dimensional foams," *Europhysics Letters*, vol. 92, p. 34002, nov 2010.

[36] D. Bi, X. Yang, M. C. Marchetti, and M. L. Manning, "Motility-driven glass and jamming transitions in biological tissues," *Physical Review X*, vol. 6, no. 2, p. 021011, 2016.

[37] J. Mauer, S. Mendez, L. Lanotte, F. Nicoud, M. Abkarian, G. Gompper, and D. A. Fedosov, "Flow-Induced Transitions of Red Blood Cell Shapes under Shear," *Physical Review Letters*, vol. 121, no. 11, p. 118103, 2018.

[38] N.-M. Ilieş, V.-S. Farcaş, O.-C. Mureşan, M.-C. Gherman, and V.-F. Chiorean, "Soil improvement with polyetylene waste materials in order to improve mechanical parameters," *International Multidisciplinary Scientific GeoConference: SGEM: Surveying Geology & mining Ecology Management*, vol. 17, no. 1.2, pp. 751–758, 2017.

[39] M. O. B. Rúa and P. Bustamante-Baena, "Modeling the mechanical behavior of a kaolin ceramic paste owing to the variation in the particle size," *Boletín de la Sociedad Española de Cerámica y Vidrio*, vol. 59, no. 3, pp. 105 – 112, 2019.

[40] L. Parilak, E. Dudrova, R. Bidulsky, and M. Kabatova, "Derivation, testing and application of a practical compaction equation for cold die-compacted metal powders," *Powder Technology*, vol. 322, pp. 447–460, 2017.

[41] W. Tsoi and K. Lee, "Mechanical properties of cemented scrap rubber tyre chips," *Géotechnique*, vol. 61, no. 2, pp. 133–141, 2011.

[42] B. Indraratna, Y. Qi, T. Ngo, C. Rujikiatkamjorn, F. Neville, Bessa-Ferreira, and A. Shahkolahi, "Use of geogrids and recycled rubber in railroad infrastructure for enhanced performance," *Geosciences*, vol. 9, p. 30, 2019.

[43] H. Khatami, A. Deng, and M. Jaksa, "The arching effect in rubber-sand mixtures," *Geosynthetics International*, pp. 1–58, 2019.

[44] E. Mavronicola, P. Komodromos, and D. Charmpis, "Numerical Investigation of Potential Usage of Rubber-Soil Mixtures as a Distributed Seismic Isolation Approach," *Proc. of the 10th Inter. Conf. on Computational Structures Technology*, p. 168, 2010.

[45] K. Senetakis, A. Anastasiadis, and K. Pitilakis, "Dynamic properties of dry sand/rubber (srm) and gravel/rubber (grm) mixtures in a wide range of shearing strain amplitudes," *Soil Dynamics and Earthquake Engineering*, vol. 33, no. 1, pp. 38 – 53, 2012.

[46] A. Tsiavos, N. A. Alexander, A. Diambra, E. Ibraim, P. J. Vardanega, A. Gonzalez-Buelga, and A. Sextos, "A sand-rubber deformable granular layer as a low-cost seismic isolation strategy in developing countries: Experimental investigation," *Soil Dynamics and Earthquake Engineering*, vol. 125, p. 105731, 2019.

[47] M. Mashiri, J. Vinod, M. N. Sheikh, and H.-H. Tsang, "Shear strength and dilatancy behaviour of sand-tyre chip mixtures," *Soils and Foundations*, vol. 55, no. 3, pp. 517 – 528, 2015.

[48] J.-N. Roux, "Geometric origin of mechanical properties of granular materials," *Physical Review E*, vol. 61, pp. 6802–6836, Jun 2000.

[49] S. Henkes, M. van Hecke, and W. van Saarloos, "Critical jamming of frictional grains in the generalized isostaticity picture," *EPL (Europhysics Letters)*, vol. 90, p. 14003, apr 2010.

[50] R. P. Behringer, "Jamming in granular materials," *Comptes Rendus Physique*, vol. 16, no. 1, pp. 10–25, 2015. Granular physics / Physique des milieux granulaires.

[51] M. van Hecke, "Jamming of soft particles: geometry, mechanics, scaling and isostaticity," *Journal of Physics: Condensed Matter*, vol. 22, p. 033101, dec 2009.

[52] D.-H. Nguyen, E. Azéma, F. Radjai, and P. Sornay, "Effect of size polydispersity versus particle shape in dense granular media," *Physical Review E*, vol. 90, p. 012202, Jul 2014.

[53] S. Torquato and F. H. Stillinger, "Jammed hard-particle packings: From kepler to bernal and beyond," *Rev. Mod. Phys.*, vol. 82, pp. 2633–2672, Sep 2010.

[54] D. Bi, J. Zhang, B. Chakraborty, and R. P. Behringer, "Jamming by shear," *Nature*, vol. 480, pp. 355–358, Dec 2011.

[55] W. F. Oquendo-Patiño and N. Estrada, "Densest arrangement of frictionless polydisperse sphere packings with a power-law grain size distribution," *Granular Matter*, vol. 22, no. 4, p. 75, 2020.

[56] H. Zheng, D. Wang, J. Barés, and R. Behringer, "Jamming by compressing a system of granular crosses," in *EPJ Web of Conferences*, vol. 140, p. 06014, EDP Sciences, 2017.

[57] E. Azéma, F. Radjai, and F. Dubois, "Packings of irregular polyhedral particles: Strength, structure, and effects of angularity," *Physical Review E*, vol. 87, p. 062203, Jun 2013.

[58] M. Skoge, A. Donev, F. H. Stillinger, and S. Torquato, "Packing hyperspheres in high-dimensional euclidean spaces," *Phys. Rev. E*, vol. 74, p. 041127, Oct 2006.

[59] B. Andreotti, Y. Forterre, and O. Pouliquen, *Granular media: between fluid and solid*. Cambridge University press, 2013.

[60] K. E. Daniels, J. E. Kollmer, and J. G. Puckett, "Photoelastic force measurements in granular materials," *Review of Scientific Instruments*, vol. 88, no. 5, p. 051808, 2017.

[61] C. h. Liu, S. R. Nagel, D. A. Schecter, S. N. Coppersmith, S. Majumdar, O. Narayan, and T. A. Witten, "Force fluctuations in bead packs," *Science*, vol. 269, no. 5223, pp. 513–515, 1995.

[62] F. Radjai, D. E. Wolf, M. Jean, and J.-J. Moreau, "Bimodal character of stress transmission in granular packings," *Physical Review Letters*, vol. 80, pp. 61–64, Jan 1998.

[63] D. M. Mueth, H. M. Jaeger, and S. R. Nagel, "Force distribution in a granular medium," *Physical Review E*, vol. 57, pp. 3164–3169, Mar. 1998.

[64] N. Estrada, A. Taboada, and F. Radjaï, "Shear strength and force transmission in granular media with rolling resistance," *Phys. Rev. E*, vol. 78, p. 021301, Aug 2008.

[65] A. Singh, V. Magnanimo, and S. Luding, "Effect of friction on the force distribution in sheared granular materials," *Proc. of NUMGE2014*, pp. 409–14, 2014.

[66] J. Moreau, "Some numerical methods in multibody dynamics: application to granular materials," *European Journal of Mechanics A Solids*, vol. 19, pp. 93–114, 1994.

[67] T. Binaree, E. Azéma, N. Estrada, M. Renouf, and I. Preechawuttipong, "Combined effects of contact friction and particle shape on strength properties and microstructure of sheared granular media," *Physical Review E*, vol. 102, p. 022901, 2020.

[68] J. O'Donovan, E. Ibraim, C. O'Sullivan, S. Hamlin, D. Muir Wood, and G. Marketos, "Micromechanics of seismic wave propagation in granular materials," *Granular Matter*, vol. 18, p. 56, Jun 2016.

[69] K. Taghizadeh, H. Steeb, S. Luding, and V. Magnanimo, "Elastic waves in particulate glass-rubber mixtures," *Proceedings of the Royal Society A: Mathematical, Physical and Engineering Sciences*, vol. 477, no. 2249, p. 20200834, 2021.

[70] K. Walton, "The effective elastic moduli of a random packing of spheres," *Journal of the Mechanics and Physics of Solids*, vol. 35, no. 2, pp. 213–226, 1987.

[71] P. J. Digby, "The Effective Elastic Moduli of Porous Granular Rocks," *Journal of Applied Mechanics*, vol. 48, pp. 803–808, 12 1981.

[72] W. G. Ellenbroek, Z. Zeravcic, W. van Saarloos, and M. van Hecke, "Non-affine response: Jammed packings vs. spring networks," *EPL (Europhysics Letters)*, vol. 87, p. 34004, aug 2009.

[73] J. D. Goddard, "Nonlinear Elasticity and Pressure-Dependent Wave Speeds in Granular Media," *Proceedings of the Royal Society A: Mathematical, Physical and Engineering Sciences*, vol. 430, no. 1878, pp. 105–131, 1990.

[74] H. A. Makse, N. Gland, D. L. Johnson, and L. M. Schwartz, "Why effective medium theory fails in granular materials," *Physical Review Letters*, vol. 83, no. 24, pp. 5070–5073, 1999.

[75] H. Jonsson, G. r. Alderborn, and G. Frenning, "Evaluation of bulk compression using a discrete element procedure calibrated with data from triaxial compression experiments on single particles," *Powder Technology*, vol. 345, pp. 74–81, 2019.

[76] A. Cooper and L. Eaton, "Compaction behavior of several ceramic powders," *Journal of the American Ceramic Society*, vol. 45, no. 3, pp. 97–101, 1962.

[77] I. Popescu and R. Vidu, "Compaction behaviour modeling of metal-ceramic powder mixtures. A review," *Materials and Mechanics*, vol. 16, no. 14, 2018.

[78] I. Wünsch, J. H. Finke, E. John, M. Juhnke, and A. Kwade, "A mathematical approach to consider solid compressibility in the compression of pharmaceutical powders," *Pharmaceutics*, vol. 11, no. 3, p. 121, 2019.

[79] T.-L. Vu, J. Barés, S. Mora, and S. Nezamabadi, "Numerical simulations of the compaction of assemblies of rubberlike particles: A quantitative comparison with experiments," *Physical Review E*, vol. 99, no. 6, p. 062903, 2019.

[80] T.-L. Vu, S. Nezamabadi, and S. Mora, "Compaction of elastic granular materials: inter-particles friction effects and plastic events," *Soft Matter*, vol. 16, pp. 679–687, 2020.

[81] G. A. Holzapfel, *Nonlinear Solid Mechanics: A Continuum Approach for Engineering Science*. Wiley, 2000.

[82] J. Lopera-Perez, C. Kwok, and K. Senetakis, "Micromechanical analyses of the effect of rubber size and content on sand-rubber mixtures at the critical state," *Geotextiles and Geomembranes*, vol. 45, no. 2, pp. 81–97, 2017.

[83] ASTM, *Standard practice for use of scrap tires in civil engineering applications*. American Society for Testing and Materials West Conshohocken, PA, 2008.

[84] H.-H. Tsang, "Seismic isolation by rubber-soil mixtures for developing countries," *Earthquake Engineering & Structural Dynamics*, vol. 37, no. 2, pp. 283–303, 2008.

[85] E. E. Walker, "The properties of powders. part vi. the compressibility of powders," *Trans. Faraday Soc.*, vol. 19, pp. 73–82, 1923.

[86] Y. Balshin, "Theory of compacting," *Vestn. Metalloprom*, vol. 18, no. 2, pp. 124–137, 1938.

[87] I. Shapiro and I. Kolthoff, "Studies on the Aging of Precipitates and Coprecipitation. XXXVIII. The Compressibility of Silver Bromide Powders," *Advances in Powder Metallurgy & Particulate Materials*, vol. 51, no. 2, pp. 493–493, 1947.

[88] K. Konopicky, "Parallelität der Gesetzmässigkeiten in Keramik und Pulvermetallurgie," *Radex-Rundschau*, vol. 7, no. 8, pp. 141–148, 1948.

[89] R. W. Heckel, "Density-Pressure Relations in Powder Compaction," *Trans Metal Soc Aime*, vol. 221, no. 4, pp. 671–675, 1961.

[90] M. M. Carroll and K. T. Kim, "Pressure-density equations for porous metals and metal powders," *Powder Metallurgy*, vol. 27, no. 3, pp. 153–159, 1984.

[91] K. Kawakita and K. H. Lüdde, "Some considerations on powder compression equations," *Powder Technology*, vol. 4, no. 2, pp. 61–68, 1971.

[92] I. Shapiro, "Compaction of powders X. Development of a general compaction equation," *Advances in Powder Metallurgy & Particulate Materials*, vol. 3, pp. 229–243, 1993.

[93] R. Panelli and F. Ambrozio Filho, "A study of a new phenomenological compacting equation," *Powder Technology*, vol. 114, no. 1-3, pp. 255–261, 2001.

[94] P. J. Denny, "Compaction equations: A comparison of the Heckel and Kawakita equations," *Powder Technology*, vol. 127, no. 2, pp. 162–172, 2002.

[95] J. M. Montes, F. G. Cuevas, J. Cintas, and Y. Torres, "Powder compaction law for cold die pressing," *Granular Matter*, vol. 12, no. 6, pp. 617–627, 2010.

[96] R. Ge, "A new equation for powder compaction," *Powder Metallurgy*, vol. 6, no. 3, pp. 20–24, 1995.

[97] J. van der Zwan and C. A. Siskens, "The compaction and mechanical properties of agglomerated materials," *Powder Technology*, vol. 33, no. 1, pp. 43–54, 1982.

[98] S. Gerdemann and P. Jablonski, "Compaction of Titanium Powders," *Metallurgical and Materials Transactions A*, vol. 42, p. 1325, 2011.

[99] S. Nezamabadi, X. Frank, J. Y. Delenne, J. Averseng, and F. Radjai, "Parallel implicit contact algorithm for soft particle systems," *Computer Physics Communications*, vol. 237, pp. 17–25, 2019.

[100] T. Çomoğlu, "An overview of compaction equations," *Ankara Universitesi Eczacilik Fakultesi Dergisi*, vol. 36, no. 2, pp. 123–133, 2007.

[101] D. Wang, X. An, P. Han, H. Fu, X. Yang, and Q. Zou, "Particulate scale numerical investigation on the compaction of tic-316l composite powders," *Mathematical Problems in Engineering*, vol. 2020, p. 5468076, Feb 2020.

[102] C. S. O'Hern, L. E. Silbert, A. J. Liu, and S. R. Nagel, "Jamming at zero temperature and zero applied stress: The epitome of disorder," *Phys. Rev. E*, vol. 68, p. 011306, Jul 2003.

[103] L. Pournin, M. Tsukahara, and T. M. Liebling, "Particle shape versus friction in granular jamming," *AIP Conference Proceedings*, vol. 1145, no. 1, pp. 499–502, 2009.

[104] A. T. Procopio and A. Zavaliangos, "Simulation of multi-axial compaction of granular media from loose to high relative densities," *Journal of the Mechanics and Physics of Solids*, vol. 53, no. 7, pp. 1523–1551, 2005.

[105] Y. Zou, X. An, and R. Zou, "Investigation of densification behavior of tungsten powders during hot isostatic pressing with a 3d multi-particle fem approach," *Powder Technology*, vol. 361, pp. 297–305, 2020.

[106] I. Agnolin and J. N. Roux, "On the elastic moduli of three-dimensional assemblies of spheres: Characterization and modeling of fluctuations in the particle displacement and rotation," *International Journal of Solids and Structures*, vol. 45, pp. 1101 – 1123, 2008.

[107] T. G. Mason, J. Bibette, and D. A. Weitz, "Elasticity of compressed emulsions," *Phys. Rev. Lett.*, vol. 75, pp. 2051–2054, Sep 1995.

[108] A. Boromand, A. Signoriello, J. Lowensohn, C. S. Orellana, E. R. Weeks, F. Ye, M. D. Shattuck, and C. S. O'Hern, "The role of deformability in determining the structural and mechanical properties of bubbles and emulsions," *Soft Matter*, 2019.

[109] P. A. Cundall and O. D. L. Strack, "A discrete numerical model for granular assemblies," *Géotechnique*, vol. 29, no. 1, pp. 47–65, 1979.

[110] F. Radjaï and D. F., *Discrete-element Modeling of Granular Materials*. ISTE Ltd and John Wiley & Sons Inc., 2011.

[111] D. J. Durian, "Foam mechanics at the bubble scale," *Physical Review Letters*, vol. 75, pp. 4780–4783, Dec 1995.

[112] R. T. Bonnecaze and M. Cloitre, "Micromechanics of soft particle glasses," *High Solid Dispersions*, pp. 117–161, 2010.

[113] J. Brujić, S. F. Edwards, D. V. Grinev, I. Hopkinson, D. Brujić, and H. A. Makse, "3d bulk measurements of the force distribution in a compressed emulsion system," *Faraday discussions*, vol. 123, pp. 207–220, 2003.

[114] S. Luding, "Cohesive, frictional powders: contact models for tension," *Granular Matter*, vol. 10, p. 235, Mar 2008.

[115] M. P. Allen and D. J. Tildesley, *Computer simulation of liquids*. Oxford university press, 2017.

[116] H. Choo, J. Larrahondo, and S. Burns, "Coating effects of nano-sized particles onto sand surfaces: Small strain stiffness and contact mode of iron oxide–coated sands," *Journal of Geotechnical and Geoenvironmental Engineering*, vol. 141, no. 1, p. 04014077, 2015.

[117] M. H. Khalili, J. N. Roux, J. M. Pereira, S. Brisard, and M. Bornert, "Numerical study of one-dimensional compression of granular materials. II. Elastic moduli, stresses, and microstructure," *Physical Review E*, vol. 95, no. 3, p. 032908, 2017.

[118] D. Baraff, "Fast contact force computation for nonpenetrating rigid bodies," in *Proceedings of the 21st annual conference on Computer graphics and interactive techniques*, pp. 23–34, 1994.

[119] V. Acary and B. Brogliato, *Numerical methods for nonsmooth dynamical systems: applications in mechanics and electronics*. Springer Science & Business Media, 2008.

[120] B. Harthong, J.-F. Jérier, P. Dorémus, D. Imbault, and F.-V. Donzé, "Modeling of high-density compaction of granular materials by the discrete element method," *International Journal of Solids and Structures*, vol. 46, no. 18, pp. 3357–3364, 2009.

[121] B. Storåkers, N. Fleck, and R. McMeeking, "The viscoplastic compaction of composite powders," *Journal of the Mechanics and Physics of Solids*, vol. 47, no. 4, pp. 785–815, 1999.

[122] D. Potyondy and P. Cundall, "A bonded-particle model for rock," *International Journal of Rock Mechanics and Mining Sciences*, vol. 41, no. 8, pp. 1329–1364, 2004. Rock Mechanics Results from the Underground Research Laboratory, Canada.

[123] S. Utili and R. Nova, "Dem analysis of bonded granular geomaterials," *International Journal for Numerical and Analytical Methods in Geomechanics*, vol. 32, no. 17, pp. 1997–2031, 2008.

[124] N. Cho, C. Martin, and D. Sego, "A clumped particle model for rock," *International Journal of Rock Mechanics and Mining Sciences*, vol. 44, no. 7, pp. 997–1010, 2007.

[125] G. Mollon, "Mixtures of hard and soft grains: micromechanical behavior at large strains," *Granular Matter*, vol. 20, no. 3, 2018.

[126] D. T. Gethin, R. W. Lewis, and R. S. Ransing, "A discrete deformable element approach for the compaction of powder systems," *Modelling and Simulation in Materials Science and Engineering*, vol. 11, pp. 101–114, dec 2002.

[127] X. Xin, P. Jayaraman, G. Daehn, and R. Wagoner, "Investigation of yield surface of monolithic and composite powders by explicit finite element simulation," *International Journal of Mechanical Sciences*, vol. 45, no. 4, pp. 707–723, 2003.

[128] G. Frenning, "Towards a mechanistic contact model for elastoplastic particles at high relative densities," *Finite Elements in Analysis and Design*, vol. 104, pp. 56–60, 2015.

[129] M. Jean, "The non-smooth contact dynamics method," *Computer Methods in Applied Mechanics and Engineering*, vol. 177, no. 3-4, pp. 235–257, 1999.

[130] S. D. Mesarovic and N. A. Fleck, "Frictionless indentation of dissimilar elastic-plastic spheres," *International Journal of Solids and Structures*, vol. 37, no. 46, pp. 7071–7091, 2000.

[131] Y. Chen, D. Imbault, and P. Dorémus, "Numerical simulation of cold compaction of 3d granular packings," in *Progress in Powder Metallurgy*, vol. 534 of *Materials Science Forum*, pp. 301–304, Trans Tech Publications Ltd, 1 2007.

[132] V. Acary and M. Jean, "Numerical simulation of monuments by the contact dynamics method," in *Monument-98, Workshop on seismic perfomance of monuments* (DGEMN-LNEC-JRC, ed.), (Lisbon, Portugal), pp. 69–78, Laboratório Nacional de engenharia Civil (LNEC), Lisboa, Portugal, Nov. 1998.

[133] H.-P. Cao, *Modélisation par éléments discrets rigides et/ou déformables des milieux granulaires et des troisiémes corps solides : Influence du comportement local sur le comportement global*. PhD thesis, Mécanique, Energétique, Génie Civil, Acoustique, INSA de Lyon, Lyon, 6 2011.

[134] K. Terzaghi, R. B. Peck, and G. Mesri, "Soil mechanics," *New York: John Wiley & Sons*, 1996.

[135] T. Schanz and P. Vermeer, "On the stiffness of sands," in *Pre-failure deformation behaviour of geomaterials*, pp. 383–387, Thomas Telford Publishing, 1998.

[136] GDR MiDi, "On dense granular flows," *The European Physical Journal E*, vol. 14, pp. 341–365, Aug. 2004.

[137] D. M. Walker and A. Tordesillas, "Topological evolution in dense granular materials: a complex networks perspective," *International Journal of Solids and Structures*, vol. 47, no. 5, pp. 624–639, 2010.

[138] D. Parker, "Positron emission particle tracking and its application to granular media," *Review of Scientific Instruments*, vol. 88, no. 5, p. 051803, 2017.

[139] A. Abed Zadeh, J. Barés, T. A. Brzinski, K. E. Daniels, J. Dijksman, N. Docquier, H. O. Everitt, J. E. Kollmer, O. Lantsoght, D. Wang, M. Workamp, Y. Zhao, and H. Zheng, "Enlightening force chains: a review of photoelasticimetry in granular matter," *Granular Matter*, vol. 21, p. 83, Aug 2019.

[140] Y. Zhou, B. Xu, A. Yu, and P. Zulli, "An experimental and numerical study of the angle of repose of coarse spheres," *Powder Technology*, vol. 125, no. 1, pp. 45–54, 2002.

[141] D. Bonamy, F. Daviaud, and L. Laurent, "Experimental study of granular surface flows via a fast camera: A continuous description," *Physics of Fluids*, vol. 14, no. 5, pp. 1666–1673, 2002.

[142] B. Miller, C. O'Hern, and R. P. Behringer, "Stress fluctuations for continuously sheared granular materials," *Phys. Rev. Lett.*, vol. 77, pp. 3110–3113, Oct 1996.

[143] P. Jop, Y. Forterre, and O. Pouliquen, "Crucial role of sidewalls in granular surface flows: consequences for the rheology," *Journal of Fluid Mechanics*, vol. 541, pp. 167–192, 2005.

[144] L. D. Landau, L. P. Pitaevskii, A. M. Kosevich, and E. Lifshitz, *Theory of Elasticity*. Butterworth-Heinemann, 1984.

[145] J. G. Puckett and K. E. Daniels, "Equilibrating temperaturelike variables in jammed granular subsystems," *Phys. Rev. Lett.*, vol. 110, p. 058001, Jan 2013.

[146] S. Stanier, J. Blaber, W. Take, and D. White, "Improved image-based deformation measurement for geotechnical applications," *Canadian Geotechnical Journal*, vol. 53, no. 5, pp. 727–739, 2016.

[147] Z. Tang, J. Liang, Z. Xiao, and C. Guo, "Large deformation measurement scheme for 3d digital image correlation method," *Optics and Lasers in Engineering*, vol. 50, no. 2, pp. 122–130, 2012.

[148] E. T. Owens and K. E. Daniels, "Sound propagation and force chains in granular materials," *EPL (Europhysics Letters)*, vol. 94, p. 54005, may 2011.

[149] E. Marteau and J. E. Andrade, "A novel experimental device for investigating the multiscale behavior of granular materials under shear," *Granular Matter*, vol. 19, no. 4, pp. 1–12, 2017.

[150] G. Cloud, *Optical Methods of Engineering Analysis*. Cambridge University Press, 1995.

[151] J. E. Andrade and C. F. Avila, "Granular element method (gem): linking inter-particle forces with macroscopic loading," *Granular Matter*, vol. 14, pp. 51–61, Feb 2012.

[152] M. Saadatfar, A. P. Sheppard, T. J. Senden, and A. J. Kabla, "Mapping forces in a 3d elastic assembly of grains," *Journal of the Mechanics and Physics of Solids*, vol. 60, no. 1, pp. 55–66, 2012.

[153] B. Pan, K. Qian, H. Xie, and A. Asundi, "Two-dimensional digital image correlation for in-plane displacement and strain measurement: a review," *Measurement Science and Technology*, vol. 20, p. 062001, apr 2009.

[154] F. M. Schaller, M. Neudecker, M. Saadatfar, G. W. Delaney, G. E. Schröder-Turk, and M. Schröter, "Local origin of global contact numbers in frictional ellipsoid packings," *Phys. Rev. Lett.*, vol. 114, p. 158001, Apr 2015.

[155] L. A. Taber, *Nonlinear theory of elasticity: applications in biomechanics*. World Scientific, 2004.

[156] M. Cárdenas-Barrantes, D. Cantor, J. Barés, M. Renouf, and E. Azéma, "Compaction of mixtures of rigid and highly deformable particles: A micromechanical model," *Physical Review E*, vol. 102, p. 032904, Sep 2020.

[157] D. Cantor, M. Cárdenas-Barrantes, I. Preechawuttipong, M. Renouf, and E. Azéma, "Compaction model for highly deformable particle assemblies," *Physical Review Letters*, vol. 124, p. 208003, May 2020.

[158] F. Dubois, V. Acary, and M. Jean, "La méthode de la dynamique des contacts, histoire d'une mécanique non régulière," *Comptes Rendus - Mecanique*, vol. 346, no. 3, pp. 247–262, 2018.

[159] Laboratoire de Mécanique et Génie Civil, Montpellier, France, "Lmgc90." git-xen.lmgc.univ-montp2.fr/lmgc90/lmgc90_user/wikis/home, 2021.

[160] W. M. Visscher and M. Bolsterli, "Random packing of equal and unequal spheres in two and three dimensions," *Nature*, vol. 239, no. 5374, pp. 504–507, 1972.

[161] R. S. Rivlin, "Large Elastic Deformations of Isotropic Materials. I. Fundamental Concepts," *Philosophical Transactions of the Royal Society A: Mathematical, Physical and Engineering Sciences*, vol. 240, no. 822, pp. 459–490, 1948.

[162] I. Agnolin and J. N. Roux, "Internal states of model isotropic granular packings. II. Compression and pressure cycles.," *Physical Review E*, vol. 76, p. 061303, 2007.

[163] I. Agnolin and J. N. Roux, "Internal states of model isotropic granular packings. III. Elastic properties," *Physical Review E*, vol. 76, p. 061304, 2007.

[164] T. S. Majmudar, M. Sperl, S. Luding, and R. P. Behringer, "Jamming transition in granular systems," *Physical Review Letters*, vol. 98, p. 058001, Jan 2007.

[165] L. E. Silbert, D. Ertaş, G. S. Grest, T. C. Halsey, and D. Levine, "Geometry of frictionless and frictional sphere packings," *Physical Review E*, vol. 65, p. 031304, Feb 2002.

[166] A. Donev, S. Torquato, and F. H. Stillinger, "Pair correlation function characteristics of nearly jammed disordered and ordered hard-sphere packings," *Physical Review E*, vol. 71, p. 011105, Jan 2005.

[167] M. H. Khalili, J. N. Roux, J. M. Pereira, S. Brisard, and M. Bornert, "Numerical study of one-dimensional compression of granular materials. I. Stress-strain behavior, microstructure, and irreversibility," *Physical Review E*, vol. 95, no. 3, p. 032907, 2017.

[168] I. Agnolin and J. N. Roux, "Internal states of model isotropic granular packings. I. Assemblies process, geometry and contact networks.," *Physical Review E*, vol. 76, p. 061302, 2007.

[169] S. J. Antony, "Evolution of force distribution in three-dimensional granular media," *Physical Review E*, vol. 63, Dec. 2000.

[170] A. Donev, R. Connelly, F. H. Stillinger, and S. Torquato, "Underconstrained jammed packings of nonspherical hard particles: Ellipses and ellipsoids," *Physical Review E*, vol. 75, p. 051304, May 2007.

[171] J. M. Valverde and A. Castellanos, "Random loose packing of cohesive granular materials," *Europhysics Letters (EPL)*, vol. 75, pp. 985–991, sep 2006.

[172] M. Cox, D. Wang, J. Barés, and R. P. Behringer, "Self-organized magnetic particles to tune the mechanical behavior of a granular system," *Europhysics Letters*, vol. 115, p. 64003, sep 2016.

[173] L. A. Pugnaloni, C. M. Carlevaro, M. Kramár, K. Mischaikow, and L. Kondic, "Structure of force networks in tapped particulate systems of disks and pentagons. i. clusters and loops," *Phys. Rev. E*, vol. 93, p. 062902, Jun 2016.

[174] R. J. Bathurst and L. Rothenburg, "Micromechanical aspects of isotropic granular assemblies with linear contact interactions," *Journal of Applied Mechanics, Transactions ASME*, vol. 55, no. 1, pp. 17–23, 1988.

[175] N. Brodu, J. A. Dijksman, and R. P. Behringer, "Spanning the scales of granular materials through microscopic force imaging," *Nat Commun*, vol. 6361, no. 6361, 2015.

[176] V. Richefeu, M. S. El Youssoufi, and F. Radjaï, "Shear strength properties of wet granular materials," *Physical Review E*, vol. 73, no. 5, pp. 1–11, 2006.

[177] L. La Ragione and V. Magnanimo, "Contact anisotropy and coordination number for a granular assembly: A comparison of distinct-element-method simulations and theory," *Physical Review E*, vol. 85, no. 3, p. 031304, 2012.

[178] A. Zaccone and E. Scossa-Romano, "Approximate analytical description of the non-affine response of amorphous solids," *Physical Review B*, vol. 83, p. 184205, May 2011.

[179] A. F. Bower, *Applied mechanics of solids*. CRC press, 2009.

[180] B. P. Tighe and T. J. H. Vlugt, "Stress fluctuations in granular force networks," *Journal of Statistical Mechanics: Theory and Experiment*, vol. 2011, p. P04002, apr 2011.

[181] M. Cárdenas-Barrantes, J. D. Muñoz, and W. F. Oquendo, "Contact forces distribution for a granular material from a Monte Carlo study on a single grain," *Granular Matter*, vol. 20, no. 1, 2018.

[182] M. Cárdenas-Barrantes, D. Cantor, J. Barés, M. Renouf, and E. Azéma, "Micromechanical description of the compaction of soft pentagon assemblies," *Phys. Rev. E*, vol. 103, p. 062902, Jun 2021.

[183] E. Azéma, F. Radjai, R. Peyroux, and G. Saussine, "Force transmission in a packing of pentagonal particles," *Phys. Rev. E*, vol. 76, p. 011301, 2007.

[184] M. Kramar, A. Goullet, L. Kondic, and K. Mischaikow, "Persistence of force networks in compressed granular media," *Phys. Rev. E*, vol. 87, p. 042207, Apr 2013.

[185] "Canon canoscan 9000f mark ii."

[186] "Moldstar 15 slow, castable silicone from smooth-on." `https://www.smooth-on.com/products/mold-star-15-slow/`.

[187] "Python codes to post-process experimental images (particle tracking, dic, fields computation, *etc.*)." `https://git-xen.lmgc.univ-montp2.fr/Image/granular_dic`.

[188] L. Rothenburg and Bathurst, "Analytical study of induced anisotropy in idealized granular materials," *Geotechnique*, vol. 39, no. 4, pp. 601–614, 1989.

[189] K. L. Johnson, *Contact Mechanics*. Cambridge [Cambridgeshire] ; New York: Cambridge University Press, 1985.

[190] V. L. Popov, *Contact Mechanics and Friction*. Berlin, Heidelberg: Springer Berlin Heidelberg, 2010.

[191] B. Harthong, D. Imbault, and P. Dorémus, "The study of relations between loading history and yield surfaces in powder materials using discrete finite element simulations," *Journal of the Mechanics and Physics of Solids*, vol. 60, no. 4, pp. 784–801, 2012.

[192] I. Schmidt, A. Trondl, T. Kraft, and A. Wonisch, "Simulation of the material behaviour of metal powder during compaction," *Proceedings of the Institution of Mechanical Engineers, Part E : Journal of Process Mechanical Engineering*, vol. 224, no. 3, pp. 187–194, 2010.

[193] J. Zhou, C. Zhu, W. Zhang, W. Ai, X. Zhang, and K. Liu, "Experimental and 3d mpfem simulation study on the green density of ti-6al-4v powder compact during uniaxial high velocity compaction," *Journal of Alloys and Compounds*, vol. 817, p. 153226, 2020.

[194] K. Peng, H. Pan, Z. Zheng, and J. Yu, "Compaction behavior and densification mechanisms of cuw composite powders," *Powder Technology*, vol. 382, pp. 478–490, 2021.

[195] K. C. Smith, M. Alam, and T. S. Fisher, "Athermal jamming of soft frictionless Platonic solids," *Phys. Rev. E*, vol. 82, no. 5, p. 051304, 2010.

[196] K. Kim and M. Carroll, "Compaction equations for strain hardening porous materials," *International Journal of Plasticity*, vol. 3, no. 1, pp. 63–73, 1987.